Dipl.-Ing. Markus Schätzer

Propagation of loaded cracks in two and three dimensions with XFEM

DISSERTATION

zur Erlangung des akademischen Grades

Doktor der technischen Wissenschaften

eingereicht an der

Technischen Universität Graz

Gutachter

Prof. Dr.-Ing. habil. Thomas-Peter Fries,
Institut für Baustatik,
Technische Universität Graz

Prof. Dr.-Ing. Stefan Löhnert,
Institut für Mechanik und Flächentragwerke,
Technische Universität Dresden

Graz, January 2020

EIDESSTATTLICHE ERKLÄRUNG

Ich erkläre an Eides statt, dass ich die vorliegende Arbeit selbstständig verfasst, andere als die angegebenen Quellen/Hilfsmittel nicht benutzt, und die den benutzten Quellen wörtlich und inhaltlich entnommenen Stellen als solche kenntlich gemacht habe. Das in TUGRAZonline hochgeladene Textdokument ist mit der vorliegenden Dissertation identisch.

Datum

Unterschrift

Abstract

This thesis introduces a general numerical framework in two and three dimensions for crack propagation induced by loaded crack surfaces. The distribution of the applied load may be arbitrary, wherefore the proposed method can be used for a variety of applications. The influence of different distributions is investigated in separate examples. Among the most important fields of applications of loaded cracks is hydraulic fracturing (HF). Therefore, this thesis relates to this topic frequently, although the context herein is more general and the numerical results are more academic than this concrete field of application. For loaded crack surfaces, a crack propagation model is developed based on the superposition principle of linear elastic fracture mechanics (LEFM), where the load factor of the crack surface loading is determined such that the criterion for crack propagation is met.

The approximation of loaded cracks with the Finite Element Method (FEM) leads to several issues due to the non-smooth solution properties of the problem. Therefore, other approaches were developed which simplify the handling of such problems. One of these approaches is the extended finite element method (XFEM) which is an extension of the classical FEM and offers a powerful numerical approach for solving partial differential equations (PDEs) with non-smooth solution properties. In this thesis, the proposed method is based on the XFEM with a hybrid explicit-implicit crack description. Herein, the load on the crack surface is given on an explicit surface mesh and transferred to the corresponding zero-level set of the implicit description. Therefore, integration points must be identified on the zero-level set which are also used to determine stress intensity factors by crack opening displacements.

A major advantage of the introduced procedure is the modularity which allows to improve individual aspects of the model and provides interfaces to other disciplines. Numerical results show the versatility and success of the approach.

Kurzfassung

In dieser Arbeit wird ein numerisches Verfahren für die Rissausbreitung von spannungsbehafteten Rissoberflächen in zwei und drei Dimensionen vorgestellt. Hierbei, ist die Verteilung der aufgebrachten Belastung beliebig, weshalb das vorgeschlagene Verfahren für eine Vielzahl von Anwendungen genutzt werden kann. Der Einfluss unterschiedlicher Belastungsverteilungen wird in separaten Beispielen untersucht. Zu den wichtigsten Anwendungen von druckbehafteten Rissen gehört das „hydraulic fracturing“. Daher bezieht sich diese Arbeit häufig auf dieses Thema, obwohl der Kontext hier allgemeiner ist und die numerischen Ergebnisse akademischer sind als dieses konkrete Anwendungsgebiet. Für spannungsbehaftete Risse wird nach dem Superpositionsprinzip der linear elastischen Bruchmechanik ein Rissausbreitungsmodell entwickelt, bei dem der Belastungsfaktor der Rissoberflächen so bestimmt wird, dass das Bruchkriterium erfüllt ist. Die Approximation spannungsbehafteter Rissoberflächen mit der Finite Elemente Methode (FEM) führt aufgrund der nicht glatten Lösungseigenschaften des Problems zu mehreren Erschwernissen. Daher wird die „Erweiterte Finite Elemente Methode“ (engl.: „eXtended Finite Element Method“, XFEM) eingesetzt, die auf die Approximation von nichtglatten Lösungen spezialisiert ist. In dieser Arbeit basiert die vorgeschlagene Methode auf der XFEM mit einer hybriden explizit-impliziten Rissbeschreibung. Dabei wird die Belastung auf einem expliziten Oberflächennetz vorgegeben und auf die zugehörige implizite Rissoberfläche übertragen. Dafür müssen Integrationspunkte auf der implizit definierten Oberfläche identifiziert werden, die dann auch zur Bestimmung von Spannungsintensitätsfaktoren durch Verschiebungen an der Rissfront verwendet werden. Ein wesentlicher Vorteil des vorgestellten Verfahrens ist die Modularität, die es ermöglicht, einzelne Aspekte des Modells zu verbessern und Schnittstellen zu anderen Disziplinen bereitzustellen. Numerische Ergebnisse belegen die Vielseitigkeit und den Erfolg des Ansatzes.

Acknowledgements

First of all, I want to express my sincerest gratitude to Prof. Thomas-Peter Fries for his supervision during the last years and for providing the opportunity to conduct this research. His enduring support has greatly influenced my studies and academic development and it would have been impossible to complete this work without his helpful supervision.

Besides my advisor, I would like extend my sincere appreciation to Prof. Stefan Löhnert for providing his time to examine this thesis.

Furthermore, I am especially grateful to Nikolai Weber, Endrina Rivas and Prof. Robert Gracie for their advices and our fruitful discussions.

My thanks also go to my colleagues at the Institute of Structural Analysis for the great time and cooperation. In particular, I would like to thank Christian Dünser and Bernhard Lindner for raising my interest in numerical simulations during my Master's program.

Last but not least, I want to thank my family and friends for their support and help at all times.

Contents

List of Tables

List of Figures

1 Introduction

1.1 Motivation and scope of work

In nature or industry, it is often observed that structures and materials fail below their expected tensile strength due to insufficient considerations of faults. Leonardo da Vinci already noticed that the maximum permissible load of iron wires vary with the wire length which implies that faults may control the strength. Until the beginning of the twentieth century attempts were made to capture such phenomena experimentally. Many research activities have been done in the field of fracture mechanics to prevent catastrophic failures.

In the analysis of fractures, one often assumes stress-free crack surfaces [106, 115, 187]. However, there are many applications where the crack surface is loaded, in fact, this load may be the dominant driving force for the potential propagation of the crack. Examples are corrosion and freezing processes in fractured structures. Another example is hydraulic fracturing (HF) for reservoir stimulation where a fracking fluid is pumped into some rock formation to induce fractures and increase the permeability and, thereby, the productivity [2, 113, 141]. Loaded crack surfaces similar to HF also occur, e.g., in dam break scenarios or in magma-driven dykes [155]. Hence, the investigation and numerical analysis of cracks under loading conditions which apply to the crack surface itself is important. For a general assessment, it is very useful to assume sharp crack surfaces where the crack surface is identified by a surface mesh or level-set function and, consequently, the locations where the stresses are acting are clearly identified. This is in contrast to smeared crack representations as in phase-field methods [116, 125, 130] where the consideration of general loading conditions within cracks is more difficult. Additionally, these methods are often mesh-dependent and require extremely fine meshes to resolve the sharp discontinuity across the crack surfaces [171].

The *extended* finite element method (XFEM) has developed to be a standard tool in fracture mechanics with a sharp crack representation [17, 53, 128, 181]. Many research activities have been done to improve the accuracy and efficiency of the XFEM in fracture mechanics. Adaptive local mesh refinements in XFEM ensure an accurate modeling of the crack front, see, e.g., [71, 86, 99, 191, 196]. In [43], an XFEM approach has been developed for modelling multiple branched cracks, voids and cracks emanating from holes. A junction enrichment was introduced in [168] to describe intersecting fractures in deformable

porous media. Intersections between hydraulic and natural fractures are investigated in the context of XFEM in [40]. An XFEM formulation with higher-order elements for curved cracks was introduced, e.g., in [33, 175], however, the higher-order accuracy may only hardly be extended to *propagating* and three-dimensional cracks. Kang [103–105] applied a consecutive interpolation procedure in XFEM which provides smoother stress distributions also in the vicinity of the crack tip leading to improved stress intensity factors (SIFs). The modeling of cohesive cracks with the XFEM was investigated, e.g., in [98, 111, 127, 197]. For further literature on the XFEM, interested readers are referred to the overviews given in [18, 70] and text books [110, 143]. It is also noted that meshfree methods may be used in the context of fracture mechanics with sharp crack representations, see [56, 144, 147, 198].

The motivation for this thesis stems from the ambition to provide a general numerical framework for crack propagation in two or three dimensions with arbitrarily curved and *loaded* crack surfaces. Therefore, the XFEM is preferred due to the ability to consider sharp crack surfaces without remeshing in an accurate, efficient and reliable manner. Herein, the XFEM with a hybrid explicit-implicit crack description from [16, 68] is adopted and significantly extended as described in [164]. This enables a very general setup for loaded crack surfaces: On the one hand, an explicit crack representation based on surface meshes is used which simplifies the definition of the crack update during propagation. It also enables a very general framework to consider for general loadings on the crack surfaces: The stress fields may be defined on the surface mesh or even result from solving additional model equations on the surface mesh. On the other hand, also an implicit crack representation based on zero level-sets is generated from the explicit one which is useful for addressing major XFEM-related issues, most importantly (i) the definition of enriched nodes, (ii) the enrichment functions based on customary coordinate systems, and (iii) the numerical integration.

The focus of this contribution is on interpolating and integrating the stress fields for which data are transferred from the explicit to the implicit crack description. Furthermore, a very general procedure for the extraction of SIFs is presented which is based on fitting the approximated crack opening displacements (CODs) to the expected displacement fields of the individual crack modes, see, e.g., [159, 161]. This is not trivial because the displacement fields are determined based on the implicit description, that is, for the fitting, it is required to explicitly locate points on the zero-level sets. Finally, a new approach is presented to extract a crack propagation criterion for which the overall loading is seperated into two states: one is the load on the crack surface, the other the remaining load including traction and displacement boundary conditions. It is then determined by which factor the crack loading may be increased until the crack propagates [162, 164].

Because the most important field of application of loaded cracks seems to be in HF, this thesis relates to this topic frequently, although the context herein is more general and the numerical results are more academic than this concrete field of application. For an overview of XFEM-based approaches in the context of HF, see, e.g., [86, 120, 131, 156], where the focus is often more on the modeling and application side than on the numerical treatment. It is noted that HF is typically modeled as a coupled multi-physics problem with (at least) three different fields: (i) a model which represents the deformation of the rock, typically considered as a linear-elastic body, (ii) a model for crack propagation, and (iii) a model for the fracking fluid inside the fracture, typically represented by the Reynolds equation [2, 15]. A coupled formulation of the problem generally leads to a non-linear and time-dependent system of equations, see, for example, in [112, 131, 148, 149] where the problem is discussed in the context of porous media. It is obvious that HF (i) involves a large number of physical processes (opening of existing fracture networks versus creation of new crack surfaces, fluid lag and leak-off, energy release by toughness and viscosity), (ii) takes place on various time and length scales which are not easily bridged/upscaled and (iii) the uncertainties are immense with existing experimental and field data being sparse. This makes the modeling and simulation an extremely challenging task [49]. A current trend is to resolving these processes and influencing factors individually to judge on the importance in practical applications of HF. For example, the influences of different asymptotic behaviours in the crack-tip region are investigated in [80, 120] with respect to different propagation regimes. However, in the light of the comments made above, in particular the lack of data for validation, one may also think of coarser models which summarize physical phenomena in a largely simplified manner. These models could provide rough relations between the structural analysis (deformations, crack openings and propagation) and the exerted loading on the crack surface so that no explicit fluid model is, in fact, needed. It is noted that even such models fall into the context of the proposed numerical framework and, in fact, it is suggested how such a largely simplified model may be set up [160, 163]. A major advantage of the proposed method is the modularity which allows to improve individual aspects of the model and provides interfaces to other disciplines. For example, the use of arbitrary tractions on the crack surfaces allows the use of advanced fluid models in HF.

However, it is emphasized that this work is not to be seen as a major contribution to the modeling of HF but to the numerical treatment of arbitrarily loaded crack surfaces in general. The original contributions are mostly (i) considerable improvements of the hybrid explicit-implicit XFEM concerning the definitions of level-set functions and resulting coordinate systems, (ii) the two-way data transfer between the explicit crack surface mesh and the implicit level set functions (iii), the extraction of SIFs in 2D and 3D based

on CODs in the XFEM, and (iv) the crack propagation criterion for loaded crack surfaces based on the load factor method and superposition of loading scenarios. Applications in HF are representative for situations where very general and complex pressure profiles are present and, therefore, this work is frequently related to this application. Many other applications with loaded crack surfaces feature simpler pressure distributions such as linear or constant functions.

1.2 Outline of the thesis

Historical milestones of fracture mechanics and their corresponding fundamental concepts are briefly repeated in Sec. 2. Basic ideas are shown and their developments or influences are discussed in today's fracture mechanic concepts. In Sec. 3, the solution of a linear elastic fracture mechanics (LEFM) problem with pressurized crack surfaces with the XFEM and a hybrid explicit-implicit crack description is described based on [16, 68]. The involved coordinate systems are discussed which simplify the detection of the enriched nodes and are basis for the definition of the enrichment functions. It is shown how the enrichment functions are defined based on these coordinate systems without any inconsistencies and discontinuities between the cut element edges. Another focus is placed on the domain and surface integration based on a decomposition procedure. Coordinate systems and distances in explicit crack surface meshes are discussed in Sec. 4 which are used in Sec. 5 to define stresses and loadings on these surfaces. Furthermore, a simplified fluid model is introduced in Sec. 5 in the context of HF. Another focus of this section is the data transfer between an implicit and explicit crack description which is required due to the fact that these crack geometries may not coincide exactly. In Sec. 6, the propagation of crack surfaces is discussed. Herein, the evaluation of a critical pressure magnitude and its corresponding time is investigated based on the superposition principle of LEFM. Another focus of this section is the computation of SIFs. Verifications and numerical results of the proposed method can be found in Sec. 7. Finally, Section 8 concludes this thesis with a brief summary and outlook.

2 Review of crack modeling

In the following, a brief overview of the historical milestones of fracture mechanics and their corresponding fundamental concepts is given. Herein, basic ideas are shown and their developments or influences are discussed in today's fracture mechanics concepts. In the analysis of fractures one often assumes stress-free crack surfaces [106, 115, 187]. However, there are many applications where the crack surface is loaded, in fact, this load may be the dominant driving force for the potential propagation of the crack. Examples are corrosion and freezing processes in fractured structures. Another example is hydraulic fracturing (HF) for reservoir stimulation where a fracking fluid is pumped into some rock formation to induce fractures and increase the permeability and, thereby, the productivity [2, 113, 141]. Due to the fact that HF seems to be one of the most important industrial applications in the field of loaded cracks, a brief discussion on modeling aspects of this topic is done in the end of this chapter.

2.1 Beginnings of fracture mechanics

The development of fracture mechanics began at the beginning of the 20th century by the works of Inglis [93] and Griffith [85]. In 1913, Inglis determined stress concentration around an elliptic hole in an infinite plate. First analytical expressions of the asymptotic mechanical fields in the vicinity of the crack-tip were given in [192, 193] for linear elastic materials. Later, [92, 150] proposed solutions for asymptotic fields within non-linear elasticity. Based on Inglis' analysis, Griffith proposed a first quantitative connection between crack size and fracture stress through a simple energy balance. Herein, it is assumed that an unstable crack growth occurs when the change of the strain energy which results from an increment of crack growth overcomes the surface energy γ which is required for building the newly formed crack surfaces. This original formulation is based on a pure energy dissipation process by the surface energy of the material which is only valid for ideally brittle solids. A change of the fracture energy due to plasticity was realised by Irwin [95] and Orowan [139] who proposed a modification of Griffiths' theory. They developed a formulation where the surface energy γ is composed of an elastic γ_s and plastic γ_p part. It is noted that γ_p is typically much larger than γ_s [187]. In the 1960s, researchers focused on yielding at the crack-tip. Based on a narrow strip of yielded

material, Dugdale [58] and Barenblatt [11] developed an energy approach which considers non-linear aspects within a linear elastic fracture mechanics (LEFM) framework.

In [106], it is mentioned that many scientists agree that fracture mechanics became an engineering discipline through the basic contributions of George Irwin in the years following the Second World War. The interest in fracture mechanics increased during this time as there were several catastrophic damages caused by cracks. For example, approximately 400 of the almost 2 700 Liberty ships which were build during the Second World War sustained fractures, of which 90 were considered serious [194]. Another example took place in Cleveland in 1944 where a rupture of a liquefied natural gas storage tank destroyed 79 houses, 2 factories, and 217 automobiles [7]. There are numerous further examples where fractures caused serious incidents often with significant damage and loss of human lives.

2.2 Fundamental concepts

In LEFM, the behaviour at the crack-tip/front may be described as a linear combination of three crack modes [106, 117, 187]. The first mode is called 'mode I' or 'opening mode' which corresponds to loading components normal to the crack face Γ. It leads to symmetrical openings of the crack faces and a straight crack propagation with respect to the crack surface. Mode II is known as the 'in-plane shear mode' which is characterised by anti-symmetric displacements tangential to the crack surface and normal to the crack-front, wherefore no crack opening occurs due to mode II, however, crack propagation may still take place. Generally, mode II loadings lead to a kinking of the crack with respect to the crack surface. Mode III or 'out-of-plane shear mode' also describes an anti-symmetric displacement of the two crack faces with the difference compared to mode II that this mode considers displacements tangential to the crack surface and tangential to the crack-front which causes a twisting of the crack-front [153]. A graphical representation of the different crack modes is given in Fig. 2.1. It is noted that mode III plays a minor role in many practical applications with unclear consequences on the crack propagation and is therefore often neglected. Based on the orientation of external loads and the orientation or the shape of the crack geometry these basic modes typically occur together with possibly varying dominance of one mode over the others. Such a behaviour occurs, for example, in domains with kinked/branched cracks or under superimposed loadings of the structure.

The understanding and mechanical modeling of fractures in structures is in the core of fracture mechanics, wherefore some of the fundamental fracture mechanics concepts are briefly discussed next. Just as important is the issue of *solving* such models. Due to the complex character of the governing equations and their solutions, *computational* methods play a crucial role in fracture mechanics. Such numerical methods only approximate

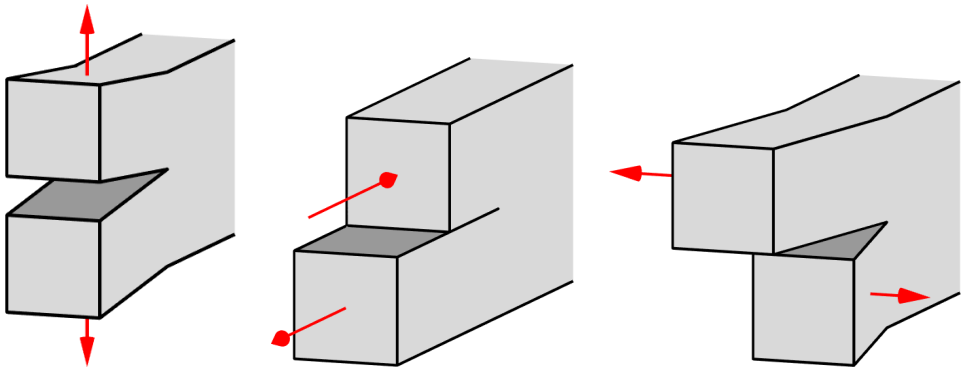

(a) Mode I (b) Mode II (c) Mode III

Figure 2.1: Definition of the three crack modes [117].

the governing equations, because analytical solutions are hardly found. The XFEM has become a popular approach for solving such problems which is discussed in more detail in Sec. 3.

2.2.1 Energy release rate

In 1920, Griffith formulated an energy balance for the formation of a crack based on the first law of thermodynamics [85]

$$\dot{W}_{\text{ext}} + \dot{Q} = \dot{E}_{\text{int}} + \dot{E}_{\text{kin}} + \dot{E}_{\Gamma}. \tag{2.1}$$

Herein, $\dot{W}_{\text{ext}}$ is the rate of energy change due to external loadings such as applied boundary tractions or body forces, $\dot{E}_{\text{int}}$ is the change of internal energy per unit time. $\dot{Q}$ describes the rate of energy transport into the body which is not covered by $\dot{W}_{\text{ext}}$, as e.g., heat flux. Changes of the kinetic energy are considered by $\dot{E}_{\text{kin}}$ and $\dot{E}_{\Gamma}$ describes the energy which is required for building new crack surfaces per unit time. If no dynamic effects are taken into account which is, for example, justified when the crack propagation occurs slowly due to time independent loads, then $\dot{E}_{\text{kin}} = 0$. In many fracture mechanics applications, it is also common practice to neglect $\dot{Q}$ as the investigated system is often assumed to be adiabatic and isolated. In LEFM, energy dissipations are neglected due to plastic deformations, wherefore the internal energy $\dot{E}_{\text{int}}$ corresponds to the elastic energy U^e [117]. Based on these assumptions and on the fact that all changes with respect to time are caused by changes of the crack size Γ, Eq. 2.1 may be written as

$$\frac{\partial}{\partial \Gamma}\left(W_{\text{ext}} - U^e\right) = \frac{\partial E_{\Gamma}}{\partial \Gamma}. \tag{2.2}$$

Herein, the left side describes the rate of energy which is available to grow an existing crack Γ to the size $\Gamma + \partial\Gamma$. This rate is known as the 'crack driving force' or the 'energy release rate G' [21, 22] where

$$G := -\frac{\partial \Pi}{\partial \Gamma} = -\frac{\partial}{\partial \Gamma}\left(U^e - W_{\text{ext}}\right). \tag{2.3}$$

The right side of Eq. 2.2 describes the energy which is required to form a new crack surface $\partial\Gamma$. This resistance of the material can be expressed through the specific surface energy γ of the material. In order to take into account that two new crack faces must be formed during a crack growth, the resistance of the material to a crack propagation can be defined as

$$\frac{\partial E_\Gamma}{\partial \Gamma} = 2\gamma = G_c, \tag{2.4}$$

where G_c is known as 'critical energy release rate'. It is noted that for brittle materials this resistance is independent of the crack length and stress state.

2.2.2 Stability of crack propagation

As previously mentioned, a crack propagates when the energy release rate G meets G_c. That is, if the crack driving force is less than the resistance of the material the crack is static and a continuous increase of the load further opens the crack until the critical state is reached. The stability of the propagation can be determined with the crack resistance curve R [187]. Herein, the energy release rate and the material resistance are plotted over the corresponding crack length, see Fig. 2.2. The resistances are obtained

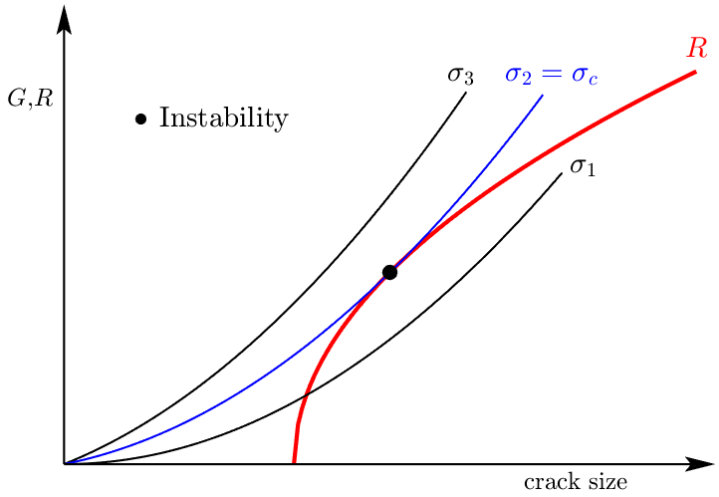

Figure 2.2: Schematic G-R curve diagram [187].

from experiments with stable crack growth. The resulting line is called 'crack resistance

curve R' which is generally curved. An exception exists for brittle materials where the resistance remains constant with crack growth, see Eq. 2.4. G depends on the crack size and the loading σ which is illustrated in Fig. 2.2 for some selected load magnitudes σ_i. R may be interpreted as a material parameter which is a function rather of $\Delta\Gamma$ than of Γ, wherefore it is possible to move this curve horizontally in the diagram. A crack grows stable when the rate of increase of the crack driving force G with crack length does not exceed the rate of increase of the resistance R to crack growth. That is, the stability of a crack growth may be expressed as follows

$$\frac{\partial G}{\partial \Gamma} \begin{cases} < \frac{\partial R}{\partial \Gamma} & \text{stable,} \\ = \frac{\partial R}{\partial \Gamma} & \text{indifferent,} \\ > \frac{\partial R}{\partial \Gamma} & \text{unstable.} \end{cases} \tag{2.5}$$

It is noted that in LEFM the resistance is constant $\frac{\partial R}{\partial \Gamma} = 0$, wherefore no stable propagation is possible. An exception is a fatigue propagation which occurs below the critical state R. Herein, threshold formulations ΔK_{th} are often used for the decision whether a propagation occurs [154]. Based on the G-R-diagram it is possible to determine the critical load magnitude σ_c of an existing crack Γ or the critical crack length Γ_c for a given loading. The critical load σ_c is determined by its associated G-curve and is defined as the curve which meets R tangentially. The critical crack length Γ_c for a given loading and its corresponding G may be determined by moving R horizontally until it meets G tangentially. The magnitude of the horizontal shift describes the length of the stable crack growth.

2.2.3 Stress intensity factors

The stress field in any two-dimensional linear elastic cracked body may be described based on a polar coordinate system with the origin at the crack-tip as [187]

$$\sigma_{ij} = \left(\frac{k}{\sqrt{r}}\right) f_{ij}(\theta) + \sum_{n=0}^{\infty} A_n r^{\frac{n}{2}} g_{ij}^{(n)}(\theta). \tag{2.6}$$

Such a solution was first published in the works of Westergard [192], Irwin [96], Sneddon [172] and Williams [193] where A_n is the n-th amplitude of the dimensionless function $g_{ij}^{(n)}$. These terms are known as the higher-order parts of the solution which depend on the geometry and remain finite within the domain. On the other hand, the first term has a singular behaviour at the crack-tip which dominates the stress state there. That is, the higher-order terms have a minor importance near the crack-tip, wherefore they are

often neglected. The scaled amplitude $K = k\sqrt{2\pi}$ of the singular term is called 'stress intensity factor (SIF)' which is one of the most important local crack-tip parameters in LEFM. Based on this parameter all stresses, strains and displacements may be defined as a function of r and θ. It is noted that the singularity dominated zone where the higher-order terms of Eq. 2.6 may be neglected is limited to a small region around the crack-tip, see Fig. 2.3. Outside this zone, the crack behaviour is governed by the remote boundary

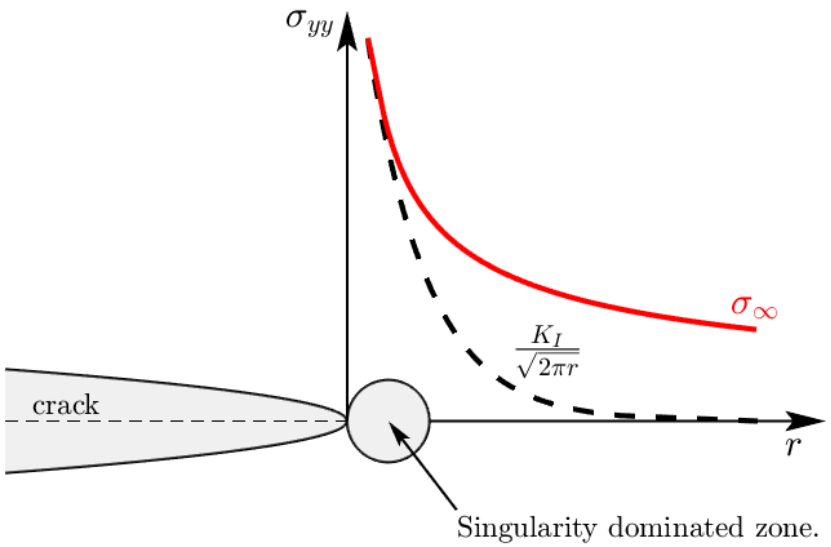

Figure 2.3: Stress normal to the crack plane in mode I for $\theta = 0$ [187].

conditions, for example, far field tractions.

As previously mentioned there are three crack modes in LEFM where each mode produces the $\sqrt{r}$-singularity at the crack-tip. However, the amplitude of the singular term of Eq. 2.6 and its corresponding dimensionless function $f_{ij}(\theta)$ depend on the current mode [187]. Based on the superposition principle it is convenient to consider the individual modes separately which is possible because the individual contributions to a total stress state may be superimposed,

$$\boldsymbol{\sigma}(r,\theta) = \sum_{m=I}^{\mathrm{III}} \frac{K_m}{\sqrt{2\pi r}} \cdot \mathbf{f}_m(\theta). \tag{2.7}$$

Herein, K_m is the stress intensity factor of mode m and $\mathbf{f}_m(\theta)$ the corresponding dimen-

sionless functions which are given for a mode I loading with [106]

$$\boldsymbol{f}_{\mathrm{I}}(\theta) = \begin{bmatrix} \cos(\frac{\theta}{2})\left[1-\sin(\frac{\theta}{2})\sin(\frac{3\theta}{2})\right] & \cos(\frac{\theta}{2})\sin(\frac{\theta}{2})\sin(\frac{3\theta}{2}) & 0 \\ & \cos(\frac{\theta}{2})\left[1+\sin(\frac{\theta}{2})\sin(\frac{3\theta}{2})\right] & 0 \\ \text{sym.} & & \sigma_{zz} \end{bmatrix}, \tag{2.8}$$

for a mode II loading with

$$\boldsymbol{f}_{\mathrm{II}}(\theta) = \begin{bmatrix} -\sin(\frac{\theta}{2})\left[2+\cos(\frac{\theta}{2})\cos(\frac{3\theta}{2})\right] & \cos(\frac{\theta}{2})\left[1-\sin(\frac{\theta}{2})\sin(\frac{3\theta}{2})\right] & 0 \\ & \sin(\frac{\theta}{2})\cos(\frac{\theta}{2})\cos(\frac{3\theta}{2}) & 0 \\ \text{sym.} & & \sigma_{zz} \end{bmatrix}, \tag{2.9}$$

and for a mode III loading with

$$\boldsymbol{f}_{\mathrm{III}}(\theta) = \begin{bmatrix} 0 & 0 & -\sin(\frac{\theta}{2}) \\ & 0 & \cos(\frac{\theta}{2}) \\ \text{sym.} & & 0 \end{bmatrix}. \tag{2.10}$$

Where

$$\sigma_{zz} = \begin{cases} 0 & \text{for plane stress conditions, and} \\ \nu\left(\sigma_{xx}+\sigma_{yy}\right) & \text{for plane strain conditions.} \end{cases} \tag{2.11}$$

Obviously, normal stresses σ_{zz} only occur in three dimensions or in two dimensional models with plane strain assumptions. As Eqs. 2.7- 2.10 show, it is possible to combine the SIFs of a crack mode due to different loads additively

$$K_m^{\mathrm{total}} = \sum_{i=1}^{N} K_m^i, \tag{2.12}$$

however, it is not possible to superimpose SIFs of different crack modes. A decision whether a crack propagation occurs may be based on the energy release rate, see Sec. 2.2.1. When the total SIFs are known it is possible to compute G directly by using the relationship between K and G which is given by [117]

$$G(K_m) = \frac{(1-\nu^2)}{E}\left(K_{\mathrm{I}}^2 + K_{\mathrm{II}}^2\right) + \frac{1}{2\mu}K_{\mathrm{III}}^2, \tag{2.13}$$

where E is the Young's modulus, ν the Poisson's ratio, and K_m the stress intensity factor of mode m. μ is the shear modulus which can be expressed through the Young's modulus E and the Poisson's ratio ν

$$\mu = \frac{E}{2\,(1+\nu)}. \tag{2.14}$$

Although, all modes are considered in this representation of G it assumes a self-similar crack growth, for example, a planar crack is assumed to remain planar and maintain a constant shape as it grows [187]. That is, G is evaluated for a straight extension of the crack. In general, G depends on the propagation angle θ_c which describes the kink between a straight and the actual extension of the crack. Such a behaviour is investigated, for example, in the work of Kageyama [100] who analyzed the maximum energy release rate for an infinitesimally kinked crack extension under combined mode I and II loading.

2.2.4 Conversion of boundary tractions into equivalent crack face tractions

In LEFM, it is possible to replace boundary tractions or far field tractions with equivalent crack face tractions which lead to the same SIFs [117, 143, 187]. That is, the behaviour within the crack is for both loading types equivalent which has the advantage that all occurring loadings can be treated in the same manner. In general, a preliminary simulation is required to determine these crack face tractions. However, such a calculation can be omitted when the entire stress state due to the boundary tractions is known within the theoretically *un-cracked* domain. Such a condition exists, for example, in the ground where in-situ stresses are applied which is discussed in Sec. 5.1. In this section, the replacement of the boundary tractions with equivalent crack face tractions is discussed in a general context to get a better understanding of the basic idea. Pressures within the fracture are neglected here as the conversion is independent of additional loadings which can be considered separately, see Sec. 6.2. The conversion is based on the superposition

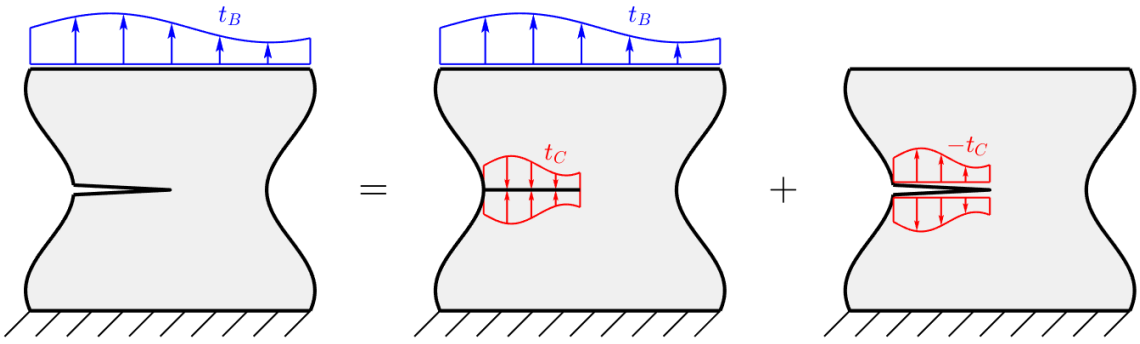

Figure 2.4: Superposition principle to replace a boundary traction with a crack face traction [117].

principle which is exemplarily shown in Fig. 2.4 for a pure mode I loading. Herein, a crack is loaded by a boundary traction $\boldsymbol{t}_N$ which leads to a crack opening and a corresponding SIF $K_{\mathrm{I}}^{(a)}$. When crack face tractions $\boldsymbol{t}_C$ are applied in addition to the boundary tractions so that the crack remains closed then the current stress intensity factor $K_{\mathrm{I}}^{(b)}$ is 0, see Fig. 2.4(b). That is, $\boldsymbol{t}_C$ are the tractions which result along the crack geometry due to a loaded domain without any cracks. Based on Eq. 2.12 the resulting SIF of Fig. 2.4(c) where $\boldsymbol{t}_C$ are applied with the opposite sign at the crack surface must be equal to $K_{\mathrm{I}}^{(a)}$. It is noted that this procedure applies equally for modes II and III, wherefore there are no restrictions on the direction or behaviour of the boundary tractions. This has the advantage that all possible in-situ stresses, e.g., normal and shear stresses, may be considered directly with the corresponding crack face tractions.

2.2.5 J-integral

The J-integral was developed in the 1960s by the works of Cherepanov [34] and Rice [152] and became a well known parameter in fracture mechanics. A main advantage of this parameter is that it can be used in LEFM as well as in elastic plastic fracture mechanics (EPFM). That is, there are no limitations on the extent of the plastic zone. The two-dimensional J-integral was originally defined for a straight crack with stress-free crack faces which is aligned with the x-axis as [152]

$$J = \int_{\Gamma} \left(W n_x - \boldsymbol{t} \cdot \frac{\partial \boldsymbol{u}}{\partial x} \right) ds. \tag{2.15}$$

Herein, Γ is a arbitrarily path around the crack-tip which starts at the lower crack face Γ_- and ends at the upper crack face Γ_+. W is the strain-energy density, $\boldsymbol{t}$ is the traction vector along the contour Γ and $\boldsymbol{u}$ is the displacement vector along Γ. The solution of the integral is a finite value which depends on the behaviour of the singularity at the crack-tip and is used for the assessment of the fracture. It is noted that Eq. 2.15 becomes zero if the contour Γ encloses a region of the domain where the solution fields are smooth. This behaviour is often used to prove the path independency of the J-integral, see Fig. 2.5. This proof is based on the subdivision of a closed contour Γ which encloses a region without a singularity into four sub-contours $\Gamma = \Gamma_1 \cup \Gamma_+ \cup \Gamma_2 \cup \Gamma_-$. It can be shown that

$$J_{\Gamma} = 0, \tag{2.16}$$

$$J_{\Gamma_+} = 0, \tag{2.17}$$

$$J_{\Gamma_-} = 0, \tag{2.18}$$

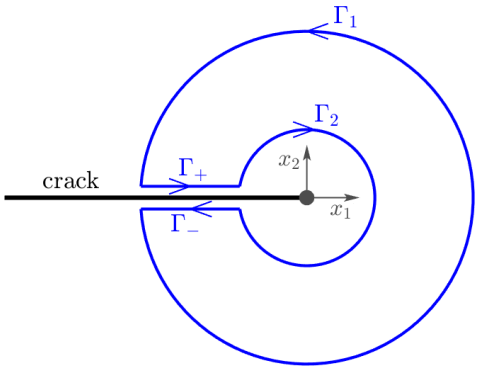

Figure 2.5: Setup for defining the J-integral.

wherefore J_{Γ_1} must be J_{Γ_2}. The first condition was previously discussed which is also valid for the configuration shown in Fig. 2.5 because there is no singularity within the region bounded by Γ. The other conditions are derived from the facts that n_x and $\boldsymbol{t}$ are zero along Γ_+ or Γ_- under the assumptions of stress-free crack faces.

A modification of the *original* formulation was developed by Karlsson and Bäcklund [107] which deals with pressurized crack faces in two dimensions. A three dimensional domain formulation of the J-integral was employed by Sukumar [182] based on the FEM coupled with the element-free Galerkin method. Viscoelastic materials are considered in a generalized J-integral which was introduced in [158]. More recently an extended J-integral formulation was developed in [174] for three-dimensional hydraulic fracturing problems in porous media.

2.2.6 Interaction integral

The interaction integral or also known as M-integral is based on the J-integral and provides a popular technique to evaluate mixed-mode SIFs [176, 195]. Herein, auxiliary fields are introduced and superposed with the actual fields which are obtained from the solution of the boundary value problem. This procedure takes advantage of the fact that the J-integral of two superimposed states, designated as *actual* and *auxiliary* here, can be expressed as

$$J^{(\mathrm{act+aux})} = J^{(\mathrm{act})} + J^{(\mathrm{aux})} + I^{(\mathrm{act,aux})}, \tag{2.19}$$

where $J^{(\mathrm{act})}$ and $J^{(\mathrm{aux})}$ are the obtained J-values of the corresponding fields and $I^{(\mathrm{act,aux})}$ is the energy interaction of the combined states which is known as the interaction integral. In many numerical frameworks, it is more convenient to evaluate the J-integral in terms of a domain integral rather than a contour integral [132, 133]. Applying the divergence

theorem, the interaction integral can be expressed in the domain form as [128, 169]

$$I^{(\mathrm{act,aux})} = \int_A \left[\sigma_{ij}^{(\mathrm{act})} \frac{\partial u_i^{(\mathrm{aux})}}{\partial x_1} + \sigma_{ij}^{(\mathrm{aux})} \frac{\partial u_i^{(\mathrm{act})}}{\partial x_1} - W^{(\mathrm{act,aux})} \delta_{1j} \right) \frac{\partial q}{\partial x_j} dA. \tag{2.20}$$

Herein, $W^{(\mathrm{act,aux})}$ is the interacted strain energy of the actual and auxiliary field which is given by

$$W^{(\mathrm{act,aux})} = {}^1\!/_2 \left(\sigma_{ij}^{(\mathrm{act})} \epsilon_{ij}^{(\mathrm{aux})} + \sigma_{ij}^{(\mathrm{aux})} \epsilon_{ij}^{(\mathrm{act})} \right), \tag{2.21}$$

and q is an arbitrary but continuous weighting function with unit value at the crack-tip and vanishes on an outer prescribed contour of the observed domain. A proper definition of q is quite simple in the context of the FEM because an interpolated function based on the standard shape functions already fulfills these requirements which can be achieved if the nodal values are prescribed with 1 within a pre-defined region around the crack-tip and with 0 otherwise [78, 128]. The energy interaction $\mathrm{I}^{(\mathrm{act,aux})}$ of the two states may also be computed based on the relationship between SIFs and G with

$$\mathrm{I}^{(\mathrm{act,aux})} = \frac{2(1-\nu^2)}{E} \left(K_{\mathrm{I}}^{(\mathrm{act})} K_{\mathrm{I}}^{(\mathrm{aux})} + K_{\mathrm{II}}^{(\mathrm{act})} K_{\mathrm{II}}^{(\mathrm{aux})} \right). \tag{2.22}$$

This behaviour can be based on Eq. 2.19 by using the fact that SIFs of a crack mode due to different loadings or states can be combined additively and the relationship between SIFs and G which was shown in Eq. 2.13. By equating Eqs. 2.20 and 2.22, mixed-mode SIFs can be extracted through an appropriate definition of the auxiliary fields. For example, the auxiliary field which results with the assumptions $K_{\mathrm{I}}^{(\mathrm{aux})} = 1$ and $K_{\mathrm{II}}^{(\mathrm{aux})} = 0$ may be used to compute $K_{\mathrm{I}}^{(\mathrm{act})}$ [128].

Based on the fundamental concept of the interaction integral which was discussed here in the context of a two-dimensional straight crack with stress-free crack surfaces within a homogeneous material, there were many developments to a wider range of applications. A formulation for computing mixed-mode SIFs for three-dimensional curved cracks in homogeneous materials under remote mechanical loadings and applied crack-face tractions were given in [190]. Two-dimensional cracks under thermo-mechanical loadings in orthotropic materials were investigated in [78]. Curvature effects were included, for example, for axissymmetric interface cracks [134], three-dimensional curved interface cracks [81] and non-planar crack fronts in three dimensions [82]. The interaction integral method was used to determine SIFs along three-dimensional bimaterial interface fronts in [140]. It is noted that the interaction integral procedure is typically evaluated in a post-processing step, wherefore the accuracy of these procedures depend strongly on the quality of the numerically determined near-field solutions of the problem in the vicinity of the crack-tip

or front.

2.3 Hydraulic fracture modeling as a practical application

Hydraulic fracturing (HF) is known as a reservoir stimulation technique which may be used in a wide range of industrial applications. Most importantly for the extraction of oil and gas. Herein, a mixture of hydraulic fluids and proppant, called *fracking fluid* is pumped into hydrocarbon layers of the host rock until a fracture initiates and propagates. The resulting fracture network increases the permeability of the material and improves the flow rate of oil and gas. Another industrial application based on this fluid driven fracture technique is, for example, in the stimulation of geothermal energy reservoirs in hot dry masses [136].

According to the large number of practical applications and the wide range of specification parameters, many different models in HF have been developed in the last century. One of the first are two-dimensional plane strain models and are known as 'Perkins-Kern-Nordgren' (PKN) [137, 141] and 'Kristianovich-Geertsma-de Klerk' (KGD) [75, 113] models which are applicable only to fully confined fractures [62]. The PKN model assumes that the crack length is much greater than the height, wherefore plane strain conditions are assumed in the vertical direction. That is, each vertical cross section acts independently and the pressure is dominated by the current height of fracture. The focus of this model is on the fluid flow and its corresponding pressure gradients within the fracture. Aspects of fracture mechanics such as crack-tip singularities are not considered there. In contrast, the KGD model assumes plane strain conditions in the horizontal direction and is therefore used for fractures where the heights are much larger than their lengths. For this model, the crack-tip behaviour is much more important than the fluid pressure gradients. Fig. 2.6 shows the geometries of both models where L is the crack length, w is the crack width and h_f is the crack height which is assumed to be constant within both models. For many practical applications these two-dimensional models are of limited applicability because they assume a planar fracture of certain height within a continuous, homogeneous, isotropic linear elastic material. That is, a previous specification of the fracture height is required which may be cumbersome since the fracture height usually varies from the well to the tip.

Three-dimensional models have been developed which are not limited to these restrictions. According to the computational effort and complexity of general three-dimensional models, the first investigations were carried out on simplified models. Three-dimensional models which attempt to capture the significant behaviour of planar models with low computational effort are known as pseudo 3D (P3D) models [62]. Two commonly used

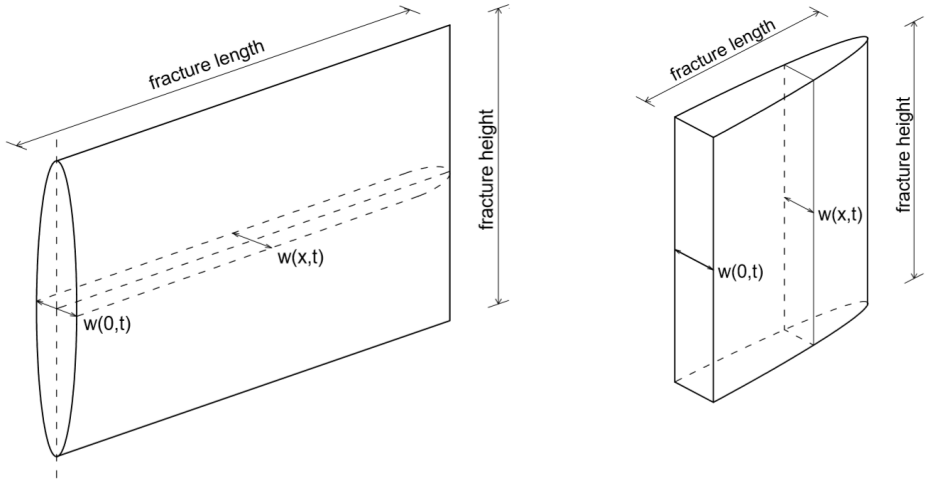

(a) (b)

Figure 2.6: Geometry of the (a) PKN and (b) KGD model [62].

types of P3D models are known as *lumped* and *cell-based* [2, 123, 145, 167]. A main difference of these two types is that lumped models are based on a predefined vertical profile (two half-ellipses) of the fracture which is matched to the horizontal length and vertical extension at the borehole at each time step. In contrast, cell-based models do not prescribe a fracture shape because they divide the fracture in a series of connected cells where each cell acts independently under the assumption of plain strain conditions. One similarity of these models is that they restrict the fluid flow to one-dimensional streamlines. A conceptual representation of the P3D fractures is given in Fig. 2.7. An enhanced formulation of the classical P3D models was introduced, for example, in [55] to capture viscous height growth and to include lateral fracture toughness. Planar fractures which are aligned and propagate perpendicular to the far-field minimum in-situ stresses (under pure mode I) may be analyzed with so called '*planar* three-dimensional' models. Although these are among the simplified 3D models, they are computationally demanding and are therefore seldomly used for routine designs [62]. In contrast to the P3D models, an entirely two-dimensional fluid flow within the fracture is taken into account here. Therefore, a two-dimensional mesh is used to discretize the fracture and to solve the fluid problem [4, 13, 39, 188]. That is, this model already leads to a coupled formulation of the problem where the crack widths of an arbitrarily shaped but planar crack interact with the fluid flow.

More recent research activities were placed in the definition of propagation regimes which capture different energy dissipating processes, see [46, 50, 121]. A classification of propagation regimes is given in [51]. There, four different hydraulic fracturing regimes are distinguished: storage/viscosity, storage/toughness, leak-off/viscosity and

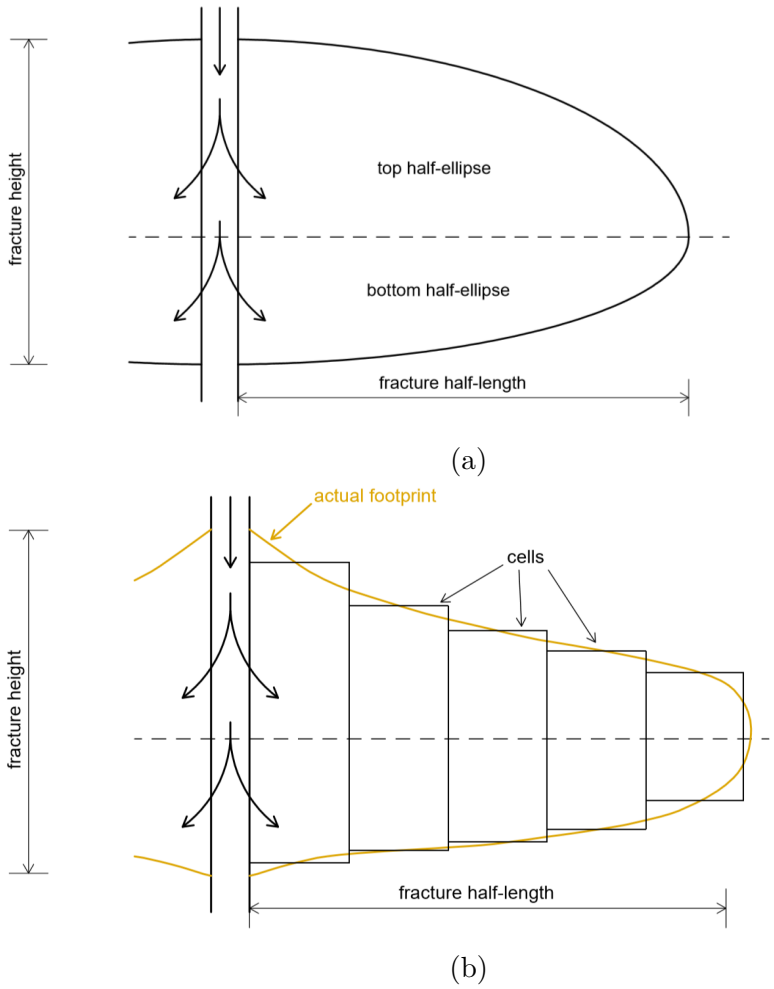

Figure 2.7: Schematic fracture geometry of the (a) lumped and (b) cell-based model [2].

leak-off/toughness. A propagation is called toughness-dominated when most of the energy is used to split the rock masses. In contrast, in a viscosity-dominated propagation regime the energy dissipation due to the fluid viscosity dominates the fracture. The transitions of the different regimes may be shown in a parametric space based on two time scales, see Fig. 2.8 where the parametric space is shown for a radial fracture [51]. Herein, t_{mk} identifies the transition from a viscosity-dominated (M) to a toughness-dominated (K) regime and $t_{m\tilde{m}}$ from a storage-dominated (M, K) to a leak-off-dominated ($\tilde{M}$, $\tilde{K}$) regime. Such a wide range of impact factors leads to complex, coupled problems which offer some efforts for numerical simulations. For example, models and simulations are performed in three different fields [156]: (i) the pressure exerted by the fracking fluid onto the surrounding rock, (ii) the deformation of the rock or fracture aperture with the corresponding fracture volume, and (iii) the propagation of the crack surfaces. These three fields lead to a fluid-structure interaction problem in general. Herein, the lubrication equation characterises

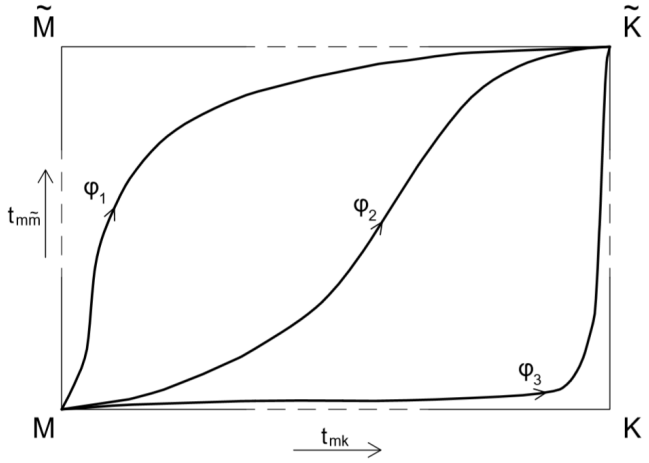

Figure 2.8: Parametric space of the different propagation regimes for a radial fracture based on two time scales [51].

the flow of the viscous fluid within the fracture and the elasticity equations characterise the elastic response of the fracture. This interaction is often described based on the Reynold's equation which poses a challenging task for numerical methods. Particularly, when the fluid and crack-front coalesce or the fluid lag vanishes due to the singularity of the fluid pressure at the crack-front [47]. Another complexity poses the fundamentally different crack-front asymptotics due to the dominant regimes [79, 120]. For example, in the viscosity-dominated regime, the well known LEFM $\sqrt{r}$-asymptote of the aperture is confined to a vanishingly small region at the fracture-front and the dominant asymptotic behaves as $r^{2/3}$ [120].

3 The extended finite element method (XFEM)

The approximation of models with non-smooth solutions is a challenging task for classical numerical methods such as the Finite Element Method (FEM) because they rely on the approximation properties of polynomials. When using the classical FEM for the approximation of discontinuous or singular fields, the mesh design requires special attention. Discontinuities must align with element edges and refinements are needed at singularities. This can already be cumbersome for quadrilateral elements. There exists a rich body of literature concerning meshing and adaptivity [65, 186]. Procedures based on hanging nodes were introduced, for example, in [6, 10, 71, 173] to simplify the generation of locally refined meshes. The mesh requirements may be implemented with reasonable effort for two-dimensional problems or for models with fixed interfaces in three dimensions, however, the effort becomes enormous for three-dimensional problems with *moving* interfaces where a remeshing is required in each time step.

Therefore, other approaches were developed which simplify the handling of such problems. One of these approaches is the XFEM which is an extension of the classical FEM and offers a powerful numerical approach for solving PDEs with non-smooth solution properties. A differentiation between an *intrinsic* and *extrinsic* XFEM approach is based on the number of introduced degrees of freedom. The intrinsic XFEM [69] enriches the classical shape functions such that they are able to reproduce the non-smooth features, wherefore no additional degrees of freedom are required. In the extrinsic XFEM, additional enrichment terms are added through the partition of unity concept [9] which lead to additional degrees of freedom. Due to the fact that the extrinsic XFEM is used more often than the intrinsic one, the extrinsic XFEM is simply the standard XFEM. All further discussion focus on this XFEM (without even using the term 'extrinsic') which itself falls into several variants. The *original* XFEM [17, 128] has been further developed to the *shifted* XFEM [19], *corrected* XFEM [66] and *stable* XFEM [8]. These variants, for example, recover Kronecker-delta property, achieve optimal convergence rates for general enrichments, and/or maintain well-conditioned systems of equations with similar dependencies on the mesh size than classical FEM [67].

In the (extrinsic) XFEM, the polynomial approximation space is enriched with additional enrichment functions such that the non-smooth solutions can be modeled independently of the mesh. That is, meshes do not have to conform to these special solution

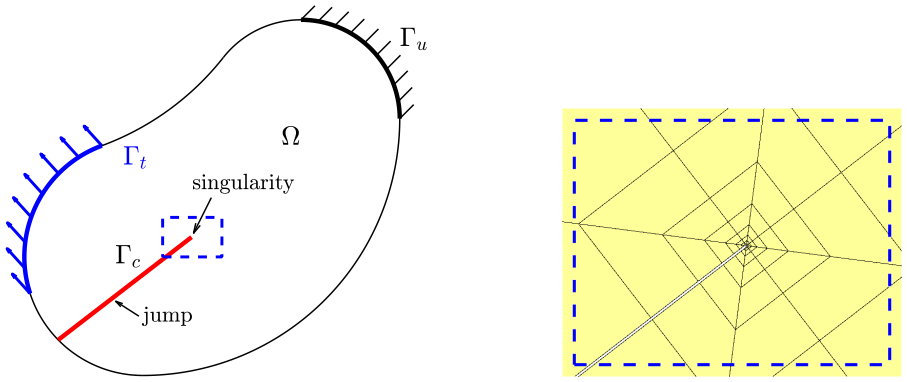

Figure 3.1: (a) Non-smooth solution properties of a LEFM problem and corresponding (b) a suitable standard FE-mesh in the vicinity of the crack-tip.

properties, wherefore no suitable mesh refinements or remeshings are required. The extended approximation $f^h(\boldsymbol{x})$ of an arbitrary scalar function $f(\boldsymbol{x})$ is typically expressed as

$$f^h(\boldsymbol{x}) = f^h_{\text{FEM}}(\boldsymbol{x}) + f^h_{\text{enr}}(\boldsymbol{x}), \tag{3.1}$$

where $f^h_{\text{FEM}}(\boldsymbol{x})$ is the approximation of the function $f(\boldsymbol{x})$ based on the standard finite element shape functions and $f^h_{\text{enr}}(\boldsymbol{x})$ is the enriched approximation which accounts for the non-smooth behaviour. The computation of the enriched approximation or the definition of the ansatz space is discussed in the context of a LEFM problem in Sec. 3.2. It is noted that a *priori* knowledge about the non-smooth solution characteristics is essential for the definition of the enrichment functions because they determine the characteristics of the enriched approximation $f^h_{\text{enr}}(\boldsymbol{x})$. They should be able to reproduce the special solution characteristics analytically to achieve optimal accuracy. Non-smooth solution properties are known for a wide range of practical applications. For example, discontinuities (jumps, kinks, etc.) and high gradients may appear across material interfaces which occur in solids as well as in two-phase flows. Models of shear bands often lead to high gradients in the displacement field or discontinuities along the interface depending on whether the shear band width is explicitly considered or not. In LEFM, displacements are discontinuous along the crack path which describe the opening of the fracture and the stresses are singular at the crack-tip, see Fig. 3.1(a). Because this leads to high requirements of suitable meshes in the classical FEM, the use of the XFEM (together with standard meshes that do not consider the cracks) is particularly promising in LEFM.

In this section, the solution of a LEFM problem with pressurized crack 'surfaces' with the XFEM and a hybrid explicit-implicit crack description is described based on [16, 68]. The involved coordinate systems are discussed which simplify the detection of the enriched

nodes and are basis for the definition of the enrichment functions. It is shown how the enrichment functions are defined based on these coordinate systems without any inconsistencies and discontinuities between the cut element edges. Another focus is placed on the domain and surface integration based on a decomposition procedure.

3.1 Crack description

Interfaces such as cracks or material transitions are often responsible for non-smooth solution properties in engineering models, wherefore a suitable definition of their location is required. They are usually defined as a manifold with one order lower dimension than the embedding physical space. This section shows different possibilities how interfaces can be defined and discusses their corresponding advantages or disadvantages in the context of crack propagation simulations with XFEM. In particular, the basic ideas of a purely explicit and implicit description are discussed and then a combined formulation is shown which combines the advantages of both descriptions.

3.1.1 Explicit crack description

A simple explicit crack description could be achieved, for example, in two dimensions by joining line-segments to an open polygon. Herein, the lines discretize the crack path and the end-nodes of the polygon discretize the crack-tips, see Fig. 3.2(a). In three dimensions, the crack represents an arbitrarily curved surface which could be described, for example, by connected two-dimensional elements embedded in 3D. Then, the element faces represent the crack surface and the obtained polygon of the boundary edges the crack-front, see Fig. 3.2(b). It is noted that such a representation of the crack geometry is generally used in the context of the classical FEM where crack geometries are obtained by decoupling element nodes along the crack surface. In this thesis, the basic idea of an explicit crack description is exemplarily discussed based on geometries which are composed of simplex elements. That is, straight line segments are used for two-dimensional problems and flat triangles are used in 3D. Crack geometries are not restricted to these special elements, however, this assumption simplifies the definition of a local coordinate system at the crack-tip/front which is needed, for example, to determine the direction of the propagation, see Sec. 6.3.

This coordinate system is defined by three linearly independent basis vectors $\boldsymbol{n}$, $\boldsymbol{t}$ and $\boldsymbol{q}$, see Fig. 3.2. These vectors represent the normal vector $\boldsymbol{n}$ of the crack surface, the tangential vector $\boldsymbol{q}$ of the crack-front and the co-normal vector $\boldsymbol{t}$ which is normal to these two vectors and can be interpreted as a planar extension of the crack. In the two-dimensional case, the definitions of $\boldsymbol{n}$ and $\boldsymbol{t}$ are quite simple because they are the normal

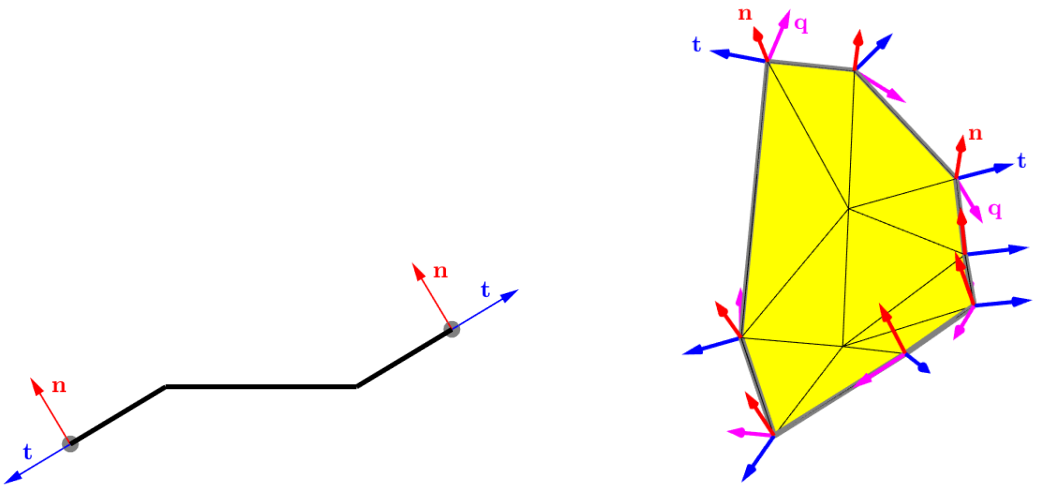

(a) (b)

Figure 3.2: Explicit crack descriptions and their corresponding local coordinate systems in (a) two and (b) three dimensions.

vectors or the straight extension vectors of line-segments associated to the crack-tip. In three dimensions, the coordinate vectors are averaged at the nodes living on the crack-front and linearly interpolated inbetween. This procedure is, for example, used in [68] where the normal vector $\boldsymbol{n}$ at the crack-front node is averaged through the neighboring element areas A_i and their corresponding element normal vectors $\boldsymbol{n}_i$ as follows

$$\boldsymbol{n} = \frac{\boldsymbol{n}^\star}{||\boldsymbol{n}^\star||} \quad \text{with :} \quad \boldsymbol{n}^\star = \frac{\sum_i A_i \cdot \boldsymbol{n}_i}{\sum_i A_i}. \tag{3.2}$$

The tangential vector $\boldsymbol{q}$ at the crack-front node is averaged with the element edge lengths l_i of the neighboring element edges and their corresponding tangential vectors $\boldsymbol{q}_i$ as

$$\boldsymbol{q} = \frac{\boldsymbol{q}^\star}{||\boldsymbol{q}^\star||} \quad \text{with :} \tag{3.3}$$

Due to the fact that the co-normal vector $\boldsymbol{t}$ is normal to the $\boldsymbol{n}$-$\boldsymbol{q}$-plane it can be determined by the associated cross product. One could easily extend the proposed procedure for simplex elements to higher-order quadrilateral and triangular elements by replacing the summations in Eqs. 3.2 and 3.3 with integral expressions.

A main advantage of the explicit crack description is that the update of the crack geometry during the propagation is simple as new segments can be added explicitly after a propagation step, see Sec. 6.3. This description also enables a very general framework to consider general loadings on the crack surfaces: The stress fields may be defined on the surface mesh or even result from solving additional model equations on the surface

mesh. However, in the context of the XFEM, a purely explicit description complicates the definition of the enrichment functions and the detection of the enriched nodes, wherefore an implicit crack description is often preferred in XFEM [129, 177, 180, 181].

3.1.2 Implicit crack description

Implicit crack descriptions by means of level-set functions are a quasi-standard in the XFEM [20, 35, 36, 179]. They have the advantage that enrichment functions can be defined based on the level-set functions and that the detection of enriched nodes is quite simple. In [177, 178], two level-set functions $\Phi(\boldsymbol{x})$ and $\Psi(\boldsymbol{x})$ are introduced to describe a two-dimensional crack geometry. The second level-set function $\Psi(\boldsymbol{x})$ is required to locate the crack-tips (in 2D) or front (in 3D) because one level-set function is only able to define closed interfaces. It is common to construct $\Phi(\boldsymbol{x})$ as a signed-distance function being zero on the crack surface and its tangential extension. The second level-set function $\Psi(\boldsymbol{x})$ can be used to define the scope of the corresponding zero-level set $\Phi(\boldsymbol{x}) = 0$ so that both level-set functions represent the crack geometry. It is noted that the construction of $\Psi(\boldsymbol{x})$ is not unique, however, it is suggested that it is orthogonal to $\Phi(\boldsymbol{x})$ at the crack-tips which ensures that the two level-set functions do not have the same tangent plane on the crack-front. Summarizing, based on these two functions the crack path or surface is defined with

$$\Phi(\boldsymbol{x}) = 0 \ \text{ and } \ \Psi(\boldsymbol{x}) < 0, \tag{3.4}$$

and the crack-tip or front with

$$\Phi(\boldsymbol{x}) = 0 \ \text{ and } \ \Psi(\boldsymbol{x}) = 0. \tag{3.5}$$

This definition is illustrated in Fig. 3.3 where the zero-level set of $\Phi(\boldsymbol{x})$ is shown in yellow, the zero-level of $\Psi(\boldsymbol{x})$ in blue and the crack-tips or front in grey. In addition, for the two-dimensional problem the level-set function $\Phi(\boldsymbol{x})$ is represented in color in Fig. 3.3(a). A three-dimensional extension of this approach is given, for example, in [84, 129]. A disadvantage of a purely implicit description is that it requires an effort for updating the crack geometry during the propagation as, for example, a Hamilton-Jacobi equation has to be solved [84] which may require a sophisticated FEM approach, e.g., due to a necessary stabilization of the governing weak form. A fast marching method was used in [38, 180] for updating level-set functions during propagation. The work of Duflot [57] provides an overview of different level-set approaches for the description and update of crack geometries.

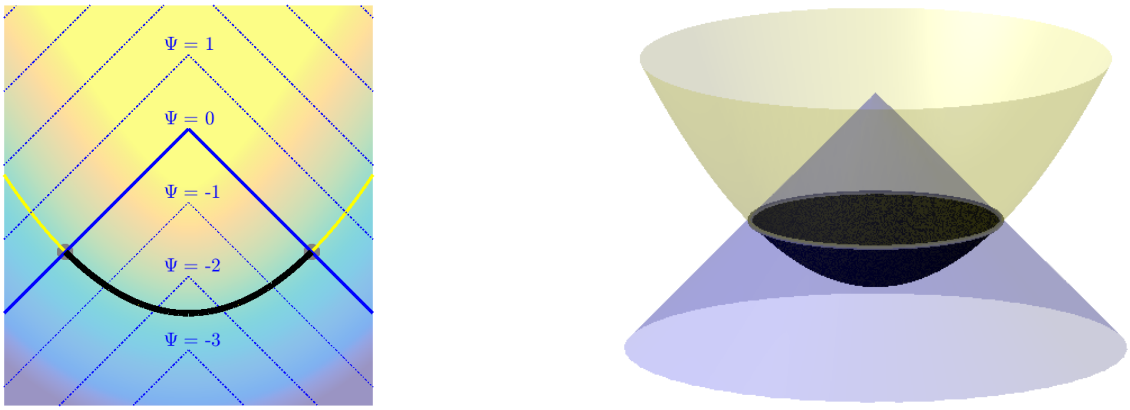

(a) (b)

Figure 3.3: Implicitly defined crack geometry based on two level-set functions in (a) two and (b) three dimensions. Related colors to the two level-set functions.

3.1.3 Hybrid explicit-implicit crack description

A hybrid explicit-implicit crack description was introduced by Fries [68] where the advantages of both descriptions were combined. Herein, the crack geometry is firstly determined explicitly by means of straight line-segments in two dimensions or flat triangles in three dimensions, see Sec. 3.1.1. This representation of the crack geometry is denoted by Γ_h in the further work.

Then, level-set functions are derived from this master configuration based on distance computations. This combined description simplifies the update of the crack geometry during propagation in comparison to a purely implicit description since this can be done explicitly by adding new segments, see Sec. 6.3. On the other hand, all benefits of an implicit description, discussed in Sec. 3.1.2, are also maintained, in particular related to enrichment schemes and numerical integration. In contrast to the two level-set functions which were used in Sec. 3.1.2 to describe the crack geometry, three level-set functions [68] are used here. These are defined as follows:

- $\phi_1(\boldsymbol{x})$ is the (unsigned) distance function to the crack path/surface.
- $\phi_2(\boldsymbol{x})$ is the (unsigned) distance function to the crack-tip/front.
- $\phi_3(\boldsymbol{x})$ is a signed distance function to the extended crack path/surface.

A graphical representation of these functions is given by some example level-sets in Fig. 3.4). To minimize the computational effort and required memory space, level-set functions are just computed in the element *nodes* and are interpolated within the ele-

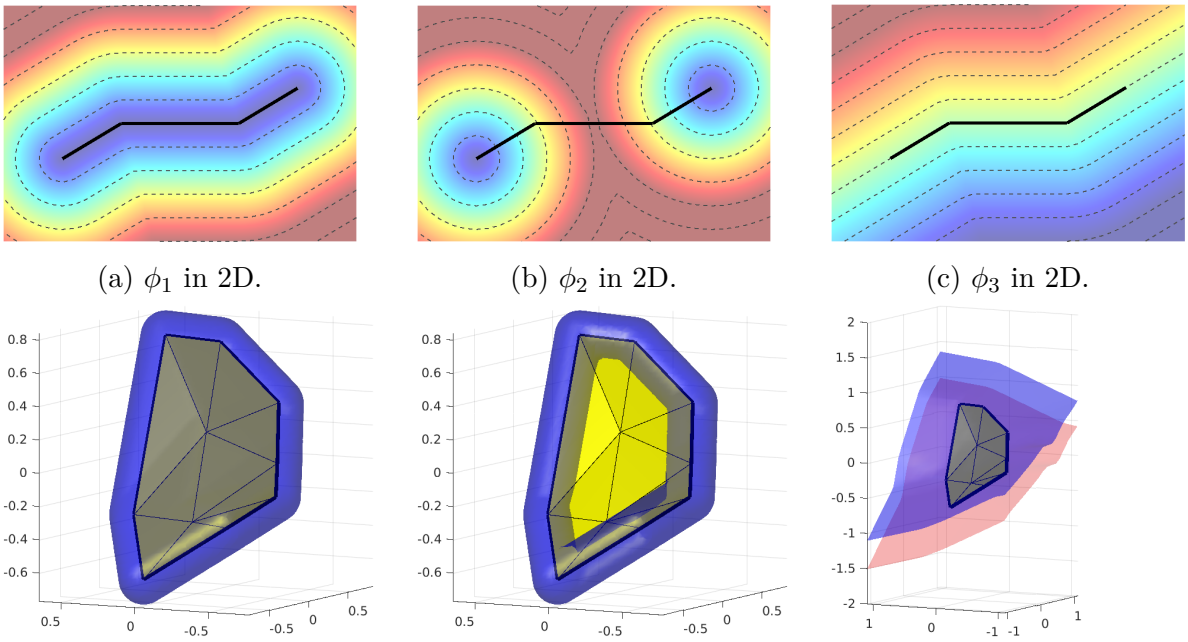

(a) ϕ_1 in 2D. (b) ϕ_2 in 2D. (c) ϕ_3 in 2D.

(d) $\phi_1 = 1$ in 3D. (e) $\phi_2 = 1$ in 3D. (f) $\phi_3 = \{-1; 1\}$ in 3D.

Figure 3.4: Level-set functions ϕ_1-ϕ_3 in (a-c) two dimensions and (d-f) some selected iso-surfaces in three dimensions [68].

ments by the corresponding shape functions

$$\phi_j^h(\boldsymbol{x}) = \sum_i N_i \phi_j(\boldsymbol{x}_i). \tag{3.6}$$

In general, the implicitly defined crack geometry based on the interpolation leads to curved zero-level sets within the reference element of the physical element and does not exactly coincide with the explicit description, see Sec. 3.3. However, the difference is vanishing upon mesh refinement and does not dominate the overall approximation error.

3.1.3.1 Coordinate system implied by three level-set functions

Based on the level-set functions ϕ_1, ϕ_2, and ϕ_3 a local coordinate system (a, b) is implied which simplifies the detection of the enriched nodes and may be used for the definition of the enrichment functions. Herein, the local coordinates are defined by two scalar functions

$$a(\boldsymbol{x}) = \pm\sqrt{\phi_2(\boldsymbol{x})^2 - \phi_3(\boldsymbol{x})^2} \tag{3.7}$$

and

$$b(\boldsymbol{x}) = \phi_3(\boldsymbol{x}). \tag{3.8}$$

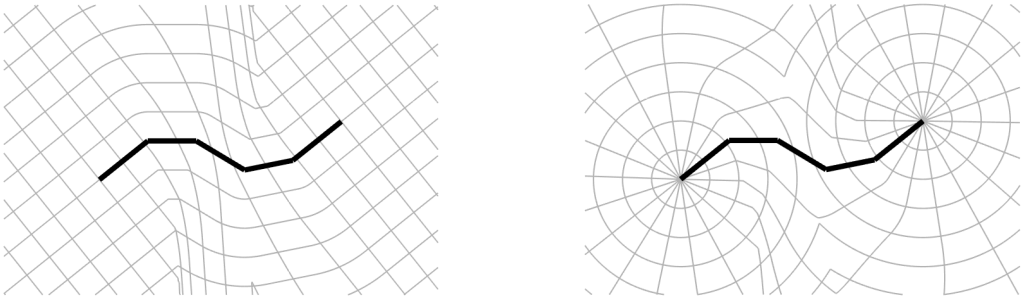

(a) (b)

Figure 3.5: (a) Local and (b) polar coordinate system implied by ϕ_1, ϕ_2, and ϕ_3 [68].

The sign of $a(\boldsymbol{x})$ depends on the position of point $\boldsymbol{x}$. It is negative for points on the crack surface or behind the crack-front and positive for points in front of the crack-front, see [68] for further information. This coordinate system is also related to the polar coordinate system (r, θ) which is used for the definition of the crack-tip/front enrichment functions of Eq. 3.21. The relation is given as

$$r(\boldsymbol{x}) = \sqrt{a(\boldsymbol{x})^2 + b(\boldsymbol{x})^2} \tag{3.9}$$

and

$$\theta(\boldsymbol{x}) = \begin{cases} \tan^{-1}\left(\frac{b(\boldsymbol{x})}{a(\boldsymbol{x})}\right) & \text{for: } a > 0; \quad b \neq 0, \\ \tan^{-1}\left(\frac{b(\boldsymbol{x})}{a(\boldsymbol{x})}\right) + \pi & \text{for: } a < 0; \quad b \neq 0, \\ \frac{\pi}{2} & \text{for: } a = 0; \quad b > 0, \\ \frac{3\pi}{2} & \text{for: } a = 0; \quad b < 0, \\ 0 & \text{for: } a > 0; \quad b = 0. \end{cases} \tag{3.10}$$

Fig. 3.5 shows the local and polar coordinate system in two dimensions, respectively. It is noted that $\nabla a(\boldsymbol{x})$ and $\nabla b(\boldsymbol{x})$ are only orthonormal for straight or planar cracks.

Similar to the interpolation of the level-set functions within the elements, also the local coordinates (a, b) and polar coordinates (r, θ) can be interpolated based on the element shape functions. However, in crack-tip enriched elements it is recommended to interpolate the polar coordinates based on the local coordinates (a, b) rather than by the level-set functions as, otherwise, the unsigned distance functions (ϕ_1, ϕ_2) lead to some issues [164]: For example, in the element containing the crack-tip, the coordinate $r(\boldsymbol{x})$ should be zero at the crack-tip. However, as the level-set values at the element nodes are all farther away from the crack-tip they are all significantly larger than 0. An interpolation will only yield values inbetween the nodal values, i.e. the desired 0 at the crack-tip is not achievable. In

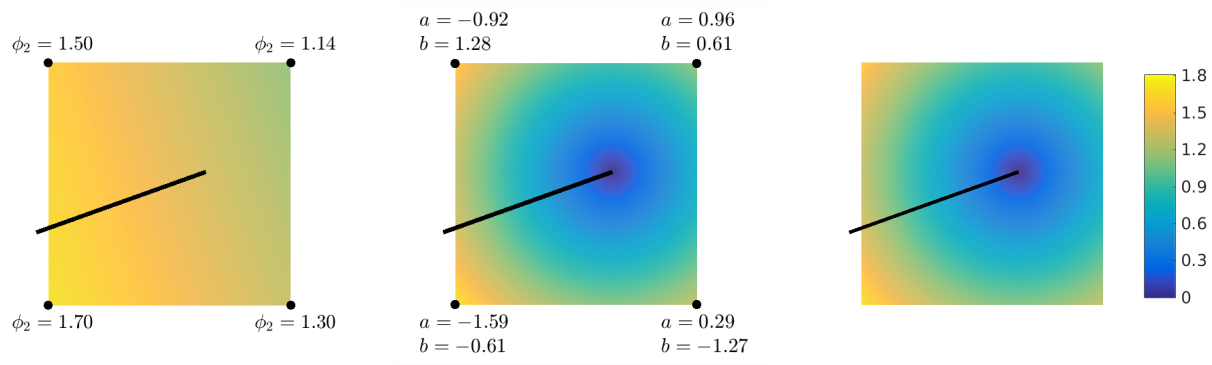

(a) (b) (c)

Figure 3.6: The coordinate $r(\boldsymbol{x})$ in the crack-tip element, (a) using $r = \phi_2$ interpolated from the nodes which is not adequate, (b) evaluating (a, b) at the nodes based on ϕ_i, interpolating within the element and computing r based on Eq. 3.9 gives a better result when compared to the exact solution shown in (c).

contrast, when the local coordinates (a, b) are evaluated at the nodes based on Eqs. 3.7 and 3.8 and then interpolated within the elements, it is possible to determine the polar coordinates (r, θ) based on these interpolated coordinates (a, b) through Eqs. 3.9 and 3.10 which will yield the desired $r = 0$ at the tip. See Fig. 3.6 for a comparison. The global derivatives of the polar coordinates are required to determine the global derivatives of the crack-tip enrichment functions which are used in Sec. 3.4 to solve the boundary value problem. They can be easily computed with the global derivatives of the shape functions which is a standard procedure in the FEM.

$$f^h_{,i}(\boldsymbol{x}) = \sum_j N_{j,i} f(\boldsymbol{x}_j). \tag{3.11}$$

However, this leads to discontinuous derivatives between the element edges due to the C_0-continuous behaviour of the shape functions. Therefore, it is proposed to determine the *exact* derivatives in the element nodes and interpolate them within the element by the corresponding shape functions [164]

$$f^h_{,i}(\boldsymbol{x}) = \sum_j N_j f_{,i}(\boldsymbol{x}_j). \tag{3.12}$$

A related setting is used in [129] where an average nodal gradient avoids the discontinuities between the elements. According to the chain rule this interpolation scheme leads to the

following formulation of the global derivatives of the polar coordinate $r(\boldsymbol{x})$ and $\theta(\boldsymbol{x})$ [164]:

$$\frac{\partial r}{\partial x_i} = \frac{\partial r}{\partial a} \cdot \frac{\partial a}{\partial x_i} + \frac{\partial r}{\partial b} \cdot \frac{\partial b}{\partial x_i} \tag{3.13}$$

$$\frac{\partial r}{\partial x_i} = \frac{\sum_j N_j a_j}{r(\sum_j N_j a_j, \sum N_j b_j)} \cdot \sum_j N_j a_{j,x_i} + \frac{\sum_j N_j b_j}{r(\sum_j N_j a_j, \sum_j N_j b_j)} \cdot \sum_j N_j b_{j,x_i} \tag{3.14}$$

$$\frac{\partial \theta}{\partial x_i} = \frac{\partial \theta}{\partial a} \cdot \frac{\partial a}{\partial x_i} + \frac{\partial \theta}{\partial b} \cdot \frac{\partial b}{\partial x_i} \tag{3.15}$$

$$\frac{\partial \theta}{\partial x_i} = \frac{-\sum_j N_j b_j}{r^2(\sum_j N_j a_j, \sum_j N_j b_j)} \cdot \sum_j N_j a_{j,x_i} + \frac{\sum_j N_j a_j}{r^2(\sum_j N_j a_j, \sum N_j b_j)} \cdot \sum_j N_j b_{j,x_i}. \tag{3.16}$$

Fig. 3.7(a-b) shows the interpolated derivatives of the polar coordinate $r(\boldsymbol{x})$ due to the standard interpolation (Eq. 3.11) and the proposed interpolation (Eq. 3.14). The *'correct'* derivatives according to continuous level-set functions ϕ_i (contrary to ϕ_i^h) are illustrated in Fig. 3.7(c). The interpolation error is quantified by means of the relative L_2-norm over the complete domain Ω as follows:

$$\varepsilon = \sqrt{\frac{\int \left(f^{\text{ref}} - f^h\right)^2 d\Omega}{\int \left(f^{\text{ref}}\right)^2 d\Omega}} \,. \tag{3.17}$$

Herein, f^{ref} represents the reference results which are achieved when the *exact* level-set values by means of no interpolation within the elements are used in all points. f^h represents the approximated results of the two interpolation schemes which are based on Eq. 3.11 or Eq. 3.14 and Eq. 3.16. The convergence rates for both interpolation schemes are shown in Fig. 3.7(d), where the dashed line represents the optimal convergence rate. These results show that the proposed interpolation scheme provides a very good accuracy. This, together with the generation of the polar coordinate system as mentioned above, may be seen as an improvement over the standard XFEM with hybrid explicit-implicit crack description from [68].

3.2 XFEM approximation of a LEFM problem

The classical FEM offers a powerful numerical approach for solving PDEs, however, it requires smooth solution features for an optimal convergence rate. Singular stresses as they appear at the crack front in LEFM, however, hinder optimal convergence. The FEM also requires a suitable mesh that accounts for the openings of the crack *faces* and the $\sqrt{r}$-behaviour of the displacement field in the vicinity of the crack-front, see Fig. 3.1(b).

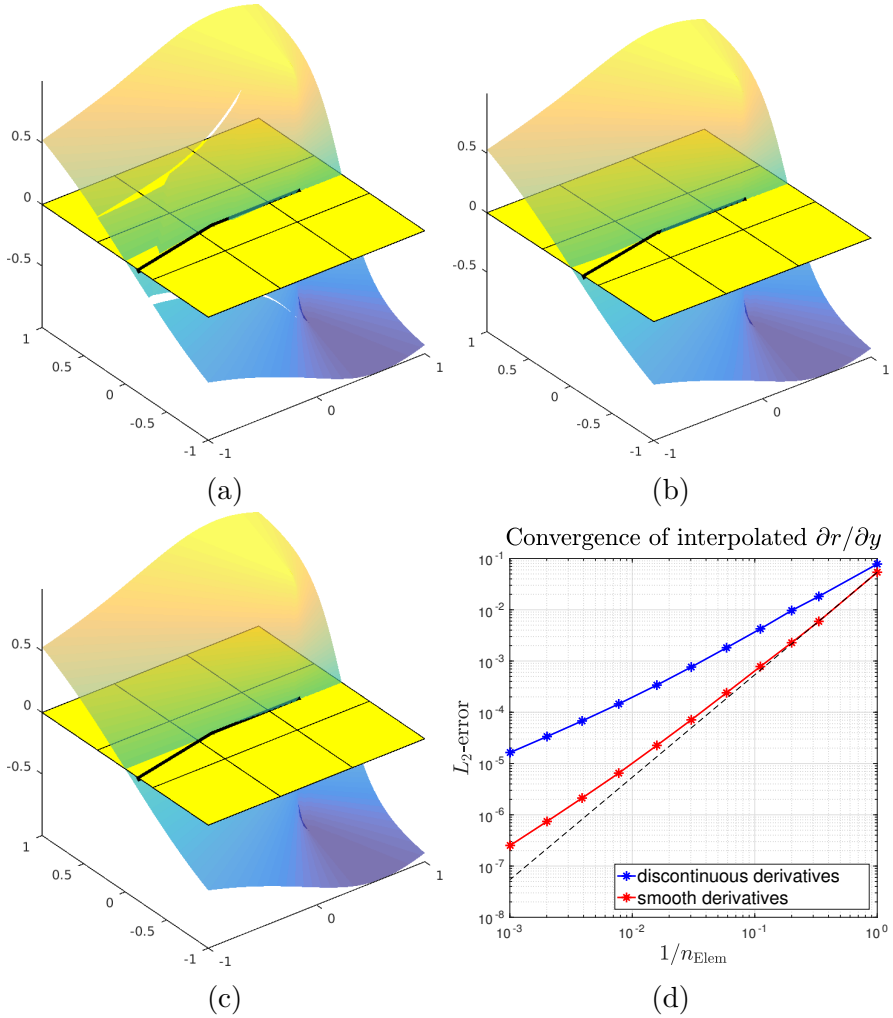

Figure 3.7: Interpolated $\partial r/\partial y$ based on (a) discontinuous derivatives obtained from Eq. 3.11, and (b) smooth derivatives obtained from Eq. 3.14 and Eq. 3.16. (c) Correct derivatives, and (d) convergence [].

That is, local mesh-refinements are required at the crack-front which, in the context of crack propagation, usually demands frequent remeshings. Other approaches such as phase-field methods [116, 125, 130] use smeared crack representations which complicate the consideration of general loading conditions within cracks. Due to the large number of practical applications which involve pressurized cracks, see Sec. 1, the investigation and numerical analysis of cracks with general loading conditions on the crack surfaces is an important topic. For such problems, the XFEM has become a popular approach since additional enrichment functions enable the approximation of inner-element discontinuities and singularities with optimal accuracy only based on uniform, regular background meshes [17, 70, 128]. That is, no remeshings and local refinements in the vicinity of the crack-front are required during propagation. Another advantage of this method is that the

crack surface is identified by a surface mesh or level-set functions, see Sec. 3.1, wherefore the locations where stresses are acting within the cracks are clearly identified. It is noted that the focus of this section is placed on the evaluation of displacements within a cracked linear-elastic body under given loading conditions based on the XFEM using the hybrid explicit-implicit crack description introduced in Sec. 3.1. In particular, more detailed discussions are based on the definition of the enriched ansatz space and on the required domain and surface integration. It is assumed here that pressure magnitudes and pressure distributions which are applied within the pre-defined fracture geometry are constant. More general physical pressure distributions are discussed in Sec. 5 and crack propagation models are discussed in Sec. 6.

In the context of LEFM with XFEM, the following enriched approximation has proven useful [128]

$$u^h(\boldsymbol{x}) = \sum_I N_i(\boldsymbol{x}) u_i + \sum_{i \in I^\star} N_i(\boldsymbol{x}) \psi_{\text{step}}(\boldsymbol{x}) a_i + \sum_{j=1}^{4} \sum_{i \in J^\star} N_i(\boldsymbol{x}) \psi_{\text{tip}}^j(r,\theta) b_i^j. \tag{3.18}$$

The first term of the right hand side represents the standard finite element part u^h_{FEM} while the other terms represent the enrichment u^h_{enr} enabling the accurate approximation of the non-smooth solution properties, compare with Eq. 3.1. N_i are the standard finite element shape functions, $\psi_{\text{step}}(\boldsymbol{x})$ and $\psi^j_{\text{tip}}(r,\theta)$ are globally defined enrichments functions, a_i and b_i^j are additional degrees of freedom at the corresponding enriched nodes $I^\star$ and $J^\star$ to be further discussed below.

It is noted that all approximations within this work are based on the shifted XFEM [19] and a hybrid explicit-implicit crack description [66], however, other versions of the XFEM may also be useful, e.g., the corrected XFEM [66] or the stable XFEM [8]. Furthermore, in this work meshes are used which are composed by linear tensor-product elements but most conclusions also apply to simplex elements.

3.2.1 Enriched nodes $I^\star$ and $J^\star$

In the context of a standard XFEM approximation of a LEFM problem, nodes with more degrees of freedom than just the classical displacements are called 'enriched nodes'. These nodes are introduced to reproduce the locally non-smooth solution properties. In Eq. 3.18, $J^\star$ are nodes in the vicinity of the crack-tip/front which reproduce the singular stresses there and $I^\star$ are nodes that are located along the crack path/surface to consider the independent moving of the two crack faces, see Fig. 3.8. There are two different techniques how the set of nodes $J^\star$ can be defined. Either enriched nodes $J^\star$ are identified as element nodes whose elements contain the crack-tip/front or as set of element nodes

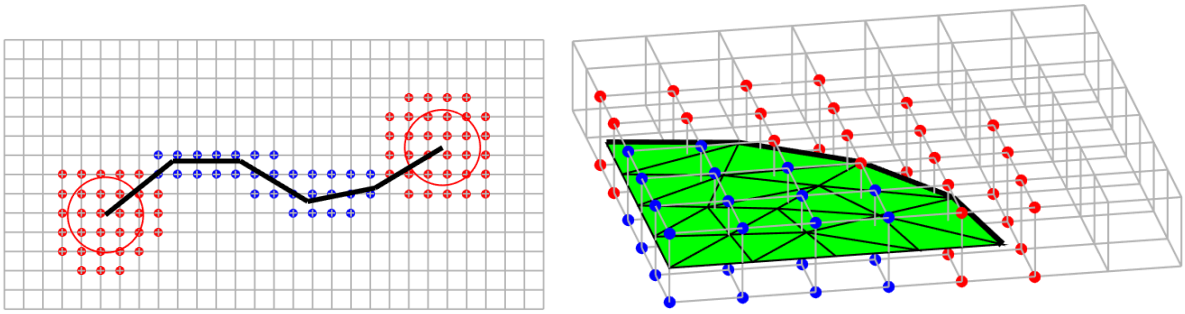

(a) (b)

Figure 3.8: Enriched nodes $I^\star$ (blue) and $J^\star$ (red) in (a) two and (b) three dimensions where the area of the crack-tip enrichment is defined by a constant radius r_{tip}.

within a fixed enrichment area near the tip/front. These two enrichment schemes differ in terms of achievable convergence rates and the condition numbers of the corresponding system of equations [33, 118]. Better convergence properties are achieved with a fixed enrichment area which is independently defined of the element sizes. However, such a procedure negatively influences the resulting condition number. In this work, $J^\star$ is defined as the set of element nodes of elements where the minimum distance of at least one element node to the crack-tip/front is smaller than a pre-defined distance r_{tip}. These two procedures are illustrated in Fig. 3.8 where crack-tip enriched nodes are shown in red and step enriched nodes in blue. Herein, the two-dimensional case shows the definition based on fixed enrichment area (defined with the distance r_{tip}) and the three-dimensional case the definition based on the crack-front associated elements. For the sake of clarity, only one layer of elements is shown in Fig. 3.8(b).

Based on Eq. 3.18 it can be seen that if all nodes of an element belong to $I^\star$ or $J^\star$ then the corresponding enrichment function ψ_{step} or ψ_{tip} can be reproduced exactly within that element, wherefore such elements are called *reproducing* elements. In contrast, elements that are only partly enriched or consist of different enriched nodes, for example, ψ_{step} and ψ_{tip} are called *blending* elements. These elements do not satisfy the partition of unity properties, wherefore the enrichment function can not be reproduced exactly there which negatively influences the performance of the approximation [118, 184]. Strategies to overcome these issues were discussed, for example, in [37, 66, 83]. It is noted that no problems occur from blending elements which arise from enrichments based on the Heaviside or sign function [70].

3.2.2 Enrichment functions

Enrichment functions are typically defined based on level-set functions which is discussed here in the context of a LEFM problem with XFEM. Discontinuous displacements along crack surfaces are realized through the global enrichment function $\psi_{\text{step}}(\boldsymbol{x})$, see Eq. 3.18, which is defined as

$$\psi_{\text{step}}(\boldsymbol{x}) := \text{sign}(\phi_3(\boldsymbol{x})) = \begin{cases} -1 & \text{for: } \phi_3(\boldsymbol{x}) < 0, \\ 0 & \text{for: } \phi_3(\boldsymbol{x}) = 0, \\ 1 & \text{for: } \phi_3(\boldsymbol{x}) > 0. \end{cases} \tag{3.19}$$

That is, $\psi_{\text{step}}(\boldsymbol{x})$ is the sign function applied to the third level-set function $\phi_3(\boldsymbol{x})$ which is positive above the crack, negative below the crack and zero at the crack, see Sec. 3.1.3. The definitions of the crack-tip enrichment functions ψ^j_{tip} are often based on the polar coordinate system $(r,\ \theta)$ which aligns with the crack surface and has its origin at the crack-front. It is noted that this coordinate system can also be expressed by the level-set functions, see Sec. 3.1.3.1, which simplifies the definition of suitable enrichment functions. It has proven useful to approximate the asymptotic behaviour in the vicinity of the crack-front with four enrichment functions

$$\psi^j_{\text{tip}}(r,\theta) := \begin{pmatrix} \psi^1_{\text{tip}}(r,\theta) \\ \psi^2_{\text{tip}}(r,\theta) \\ \psi^3_{\text{tip}}(r,\theta) \\ \psi^4_{\text{tip}}(r,\theta) \end{pmatrix} = \begin{pmatrix} r^\lambda \cos(\lambda\theta) \\ r^\lambda \sin(\lambda\theta) \\ r^\lambda \sin(\theta)\sin(\lambda\theta) \\ r^\lambda \sin(\theta)\cos(\lambda\theta) \end{pmatrix}. \tag{3.20}$$

Herein, λ characterises the asymptotic behaviour at the crack-front. In a classical LEFM sense, the crack-tip has a $\sqrt{r}$-behaviour, wherefore $\lambda = 1/2$, see Sec. 2.2.3. Fig. 3.9 shows the four crack-tip enrichments, respectively, for a straight two-dimensional crack within a classical LEFM asymptotic behaviour. However, there are applications where the tip behaviour is dominated by other influences. For example, depending on the corresponding propagation regime, the fluid-structure interaction of a HF problem leads to fundamentally different crack tip asymptotics [80, 120] which vary between the two extremes of a toughness-dominated regime ($\lambda = 1/2$) and a viscosity dominated regime ($\lambda = 2/3$). It is noted that the viscosity-dominated regime also has a $\sqrt{r}$-behaviour at the crack-tip, however, it is confined to a vanishingly small region. In the further contribution, discussions are based on the classical assumption $\lambda = 1/2$ of LEFM.

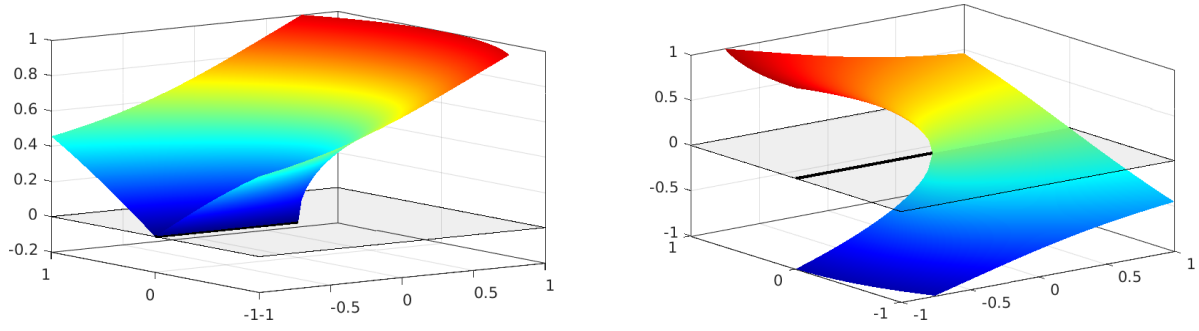

(a) $\psi^1_{\text{tip}}(r,\theta)$.

(b) $\psi^2_{\text{tip}}(r,\theta)$.

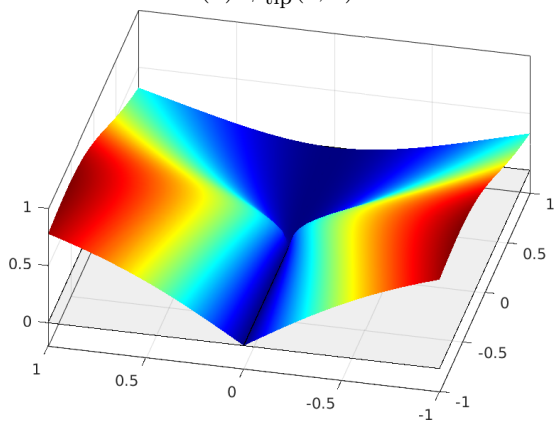

(c) $\psi^3_{\text{tip}}(r,\theta)$.

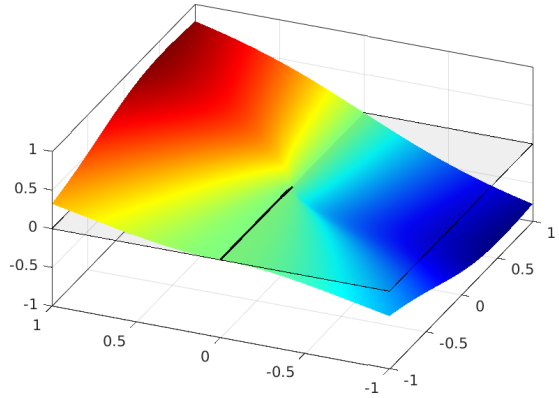

(d) $\psi^4_{\text{tip}}(r,\theta)$.

Figure 3.9: The crack-tip enrichment functions $\psi^1_{\text{tip}}(r,\theta)$-$\psi^4_{\text{tip}}(r,\theta)$ at the crack-front within a classical LEFM asymptotic behaviour.

3.2.2.1 Shifted enrichment functions

As the resulting shape functions of the enriched approximation according to Eq. 3.18 do not have Kronecker-δ property it follows for non-zero values of a_i or b^j_i that $u^h(\boldsymbol{x}_i) \neq u_i$ which complicates the imposition of Dirichlet boundary conditions and the interpretation of the solution. A shifted version of the standard XFEM approach was introduced in [19] which restores Kronecker-δ property with a minimum effort. This shifted version modifies Eq. 3.18 in order to maintain the desired properties as follows

$$u^h(\boldsymbol{x}) = \sum_I N_i(\boldsymbol{x})u_i + \sum_{i\in I^\star} N_i(\boldsymbol{x})\psi^{\text{shift,i}}_{\text{step}}(\boldsymbol{x})a_i + \sum_{j=1}^{4}\sum_{i\in J^\star} N_i(\boldsymbol{x})\psi^{j,\text{shift},i}_{\text{tip}}(r,\theta)b^j_i, \tag{3.21}$$

with

$$\psi^{\text{shift,i}}_{\text{step}} = \psi_{\text{step}}(\boldsymbol{x}) - \psi_{\text{step}}(\boldsymbol{x}_i), \qquad \text{and} \qquad \psi^{j,\text{shift},i}_{\text{tip}} = \psi^j_{\text{tip}}(r,\theta) - \psi^j_{\text{tip}}(r_i,\theta_i). \tag{3.22}$$

Herein, the index i after 'shift' indicates the associated node i of the shifting. The Kronecker-δ property of Eq. 3.21 or Eq. 3.22 can be easily proven with the following equation

$$N_i(\boldsymbol{x}_j) \cdot [\psi(\boldsymbol{x}_j) - \psi(\boldsymbol{x}_i)] \cdot a_i, \qquad \text{with} \;\; \forall i \in I^\star; \;\; \forall j \in I \tag{3.23}$$

which shows that the enrichment terms of the approximation vanish at the element nodes independently of the unknows a_i due to the fact that

$$0 = \begin{cases} N_i(\boldsymbol{x}_j) & \text{for: } i \neq j, \\ \psi(\boldsymbol{x}_j) - \psi(\boldsymbol{x}_i) & \text{for: } i = j. \end{cases} \tag{3.24}$$

The first statement is proven through the Kronecker-δ property of the standard finite element shape functions and the proof of the second case is trivial. Fig. 3.10 shows on the left side the global crack-tip enrichment functions $\psi^j_{\text{tip}}(r, \theta)$ multiplied with the FE shape function $N_1(\boldsymbol{x})$ within a reference bi-linear quadrilateral element which describes one part of the enriched approximation space of Eq. 3.18. The shifted versions of these configurations are shown in Fig. 3.10 on the right side where also the Kronecker-δ property can be seen because all nodal values of the enriched functions are zero.

3.3 Integration

In the XFEM, discontinuous shape functions require a special treatment of the numerical integration within enriched elements which is discussed here in the context of LEFM where the discontinuity follows the crack faces. The treatment of the numerical surface integration which is required for arbitrarily loaded crack faces is also part of this section. For the detection of enriched nodes and the definition of enrichment functions it is convenient to use an implicit description of the crack geometry by means of level-set functions. One issue of this description compared to an explicit description is that the zero-level sets have to be determined explicitly. It is common to compute level-set values just in element nodes and use interpolated values within the element which are based on the standard finite element shape functions N_i. A general handling of the integration may be provided if all computations are done in the reference element rather than in all physical elements of the domain separately. Therefore, all further discussions with regard to the integration are done for the reference element of the discretized domain. It is noted that simplex elements are neglected here as their handling is quite simple and may be seen as a simplified subset of the situation discussed herein for tensor-product elements.

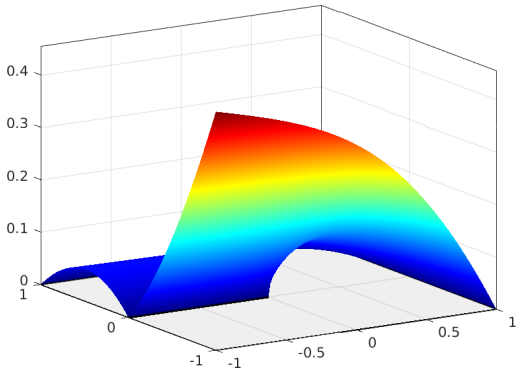

(a) $N_1 \cdot \psi^1_{\text{tip}}(r,\theta)$.

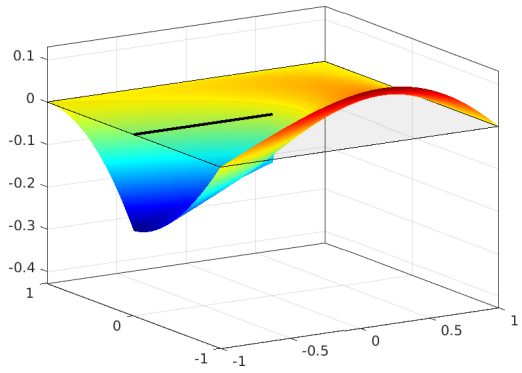

(b) $N_1 \cdot \left[\psi^1_{\text{tip}}(r,\theta) - \psi^1_{\text{tip}}(r_1,\theta_1)\right]$.

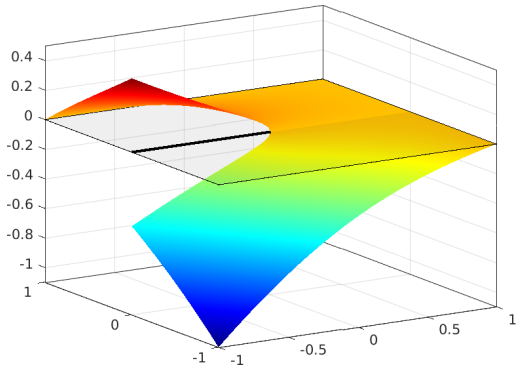

(c) $N_1 \cdot \psi^2_{\text{tip}}(r,\theta)$.

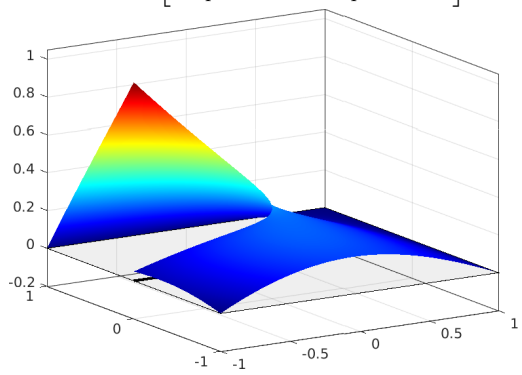

(d) $N_1 \cdot \left[\psi^2_{\text{tip}}(r,\theta) - \psi^2_{\text{tip}}(r_1,\theta_1)\right]$.

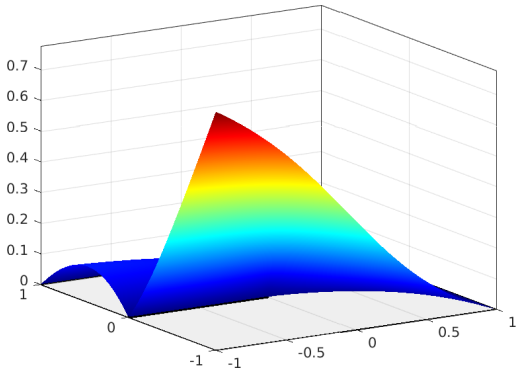

(e) $N_1 \cdot \psi^3_{\text{tip}}(r,\theta)$.

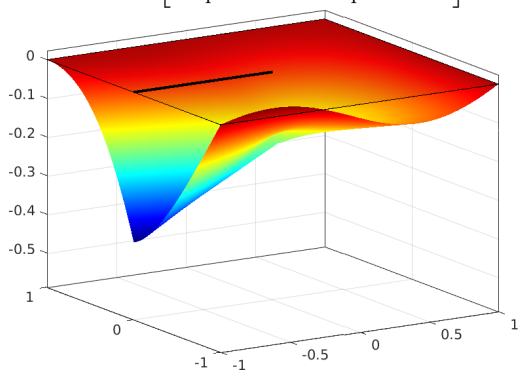

(f) $N_1 \cdot \left[\psi^3_{\text{tip}}(r,\theta) - \psi^3_{\text{tip}}(r_1,\theta_1)\right]$.

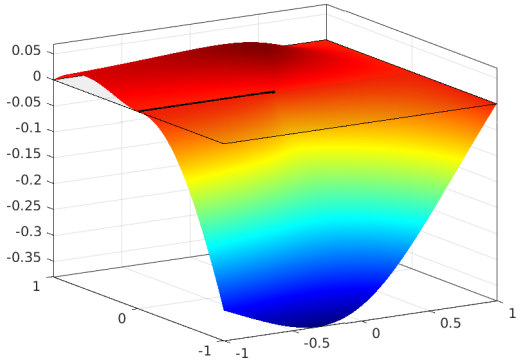

(g) $N_1 \cdot \psi^4_{\text{tip}}(r,\theta)$.

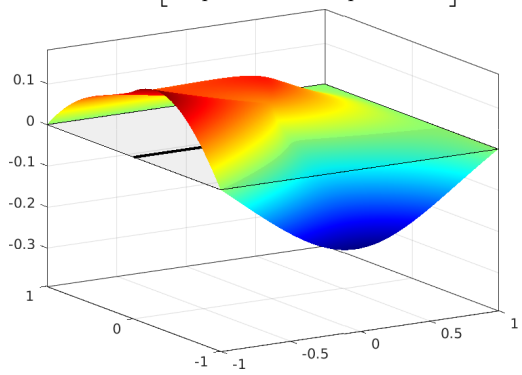

(h) $N_1 \cdot \left[\psi^4_{\text{tip}}(r,\theta) - \psi^4_{\text{tip}}(r_1,\theta_1)\right]$.

Figure 3.10: Local crack tip enrichment function within an element based on the classical XFEM approximation and the shifted version.

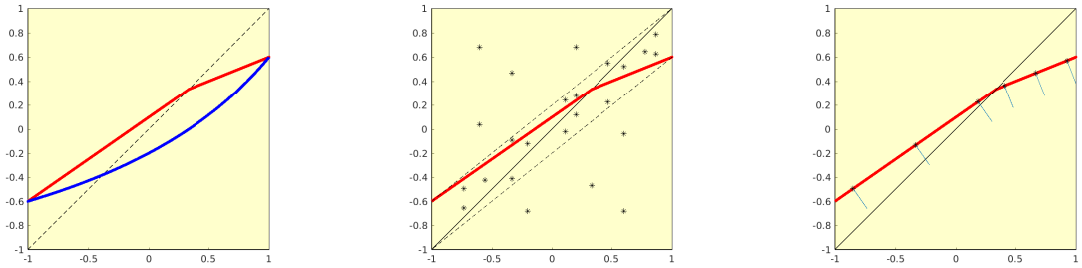

(a) (b) (c)

Figure 3.11: (a) Zero-level set in a bilinear quadrilateral element due to interpolation and decomposition. Integration points within a decomposed element for the (b) domain and (b) surface integration.

3.3.1 Detection of zero-level set

In the XFEM-approach, an issue is the detection of zero-level sets within cut elements which is discussed next. Usually, only few elements of the domain are potentially cut by zero-level sets which may be identified by the condition

$$\max[\phi_3(\boldsymbol{x}_i)] \cdot \min[\phi_3(\boldsymbol{x}_i)] < 0, \tag{3.25}$$

where $\phi_3(\boldsymbol{x}_i)$ represents the nodal values of the third level-set function which was defined in Sec. 3.1.3. In general, the interpolation of level-set functions within elements by the corresponding shape functions leads to curved zero level-sets which complicates their detection. This behaviour is shown by the blue line or surface in Fig. 3.11(a) for a bi-linear quadrilateral element or in Fig. 3.12(a) for a tri-linear hexahedral elements. Therefore, a decomposition of the corresponding *reference* elements into simplex elements is employed which simplifies the detection of the zero level-sets as they are piecewise straight or planar within these sub-elements which is shown in Figs. 3.11 and 3.12 by the red lines or surfaces. The decomposition of cut elements into polygonal sub-cells has become a standard in the XFEM and is often used for the numerical integration of the weak form, e.g., in [70, 128, 181]. A similar setting was introduced for higher-order elements in [33, 72, 73]. There is no unique way how to decompose elements and each procedure leads to a different representation of the crack geometry in general. In this paper, a quadrilateral element is subdivided into two triangles and a hexahedral element is subdivided into six tetrahedrons, see Figs. 3.11 and 3.12.

Within these simplex elements roots of the level-set functions can be easily determined

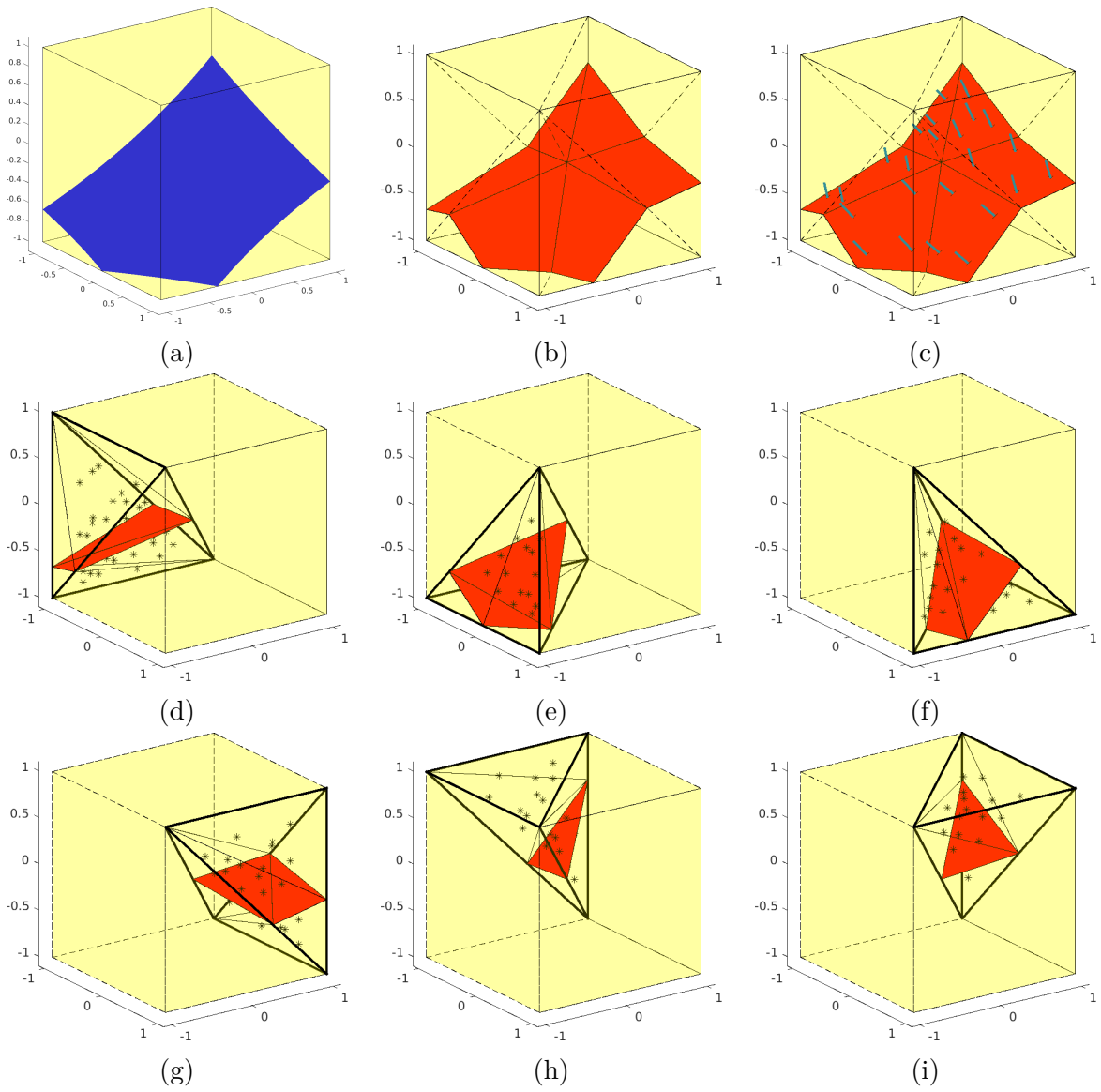

Figure 3.12: Zero-level set in a trilinear hexahedral element due to (a) interpolation and (b) decomposition. Integration points for the (c) surface integration and (d)-(i) the domain integration within the sub-elements.

along the element edges with

$$\boldsymbol{x}_j^\star = \boldsymbol{x}_1 + (\boldsymbol{x}_2 - \boldsymbol{x}_1)\,\frac{\phi_3(\boldsymbol{x}_1)}{\phi_3(\boldsymbol{x}_1) - \phi_3(\boldsymbol{x}_2)}. \tag{3.26}$$

Herein, $\boldsymbol{x}_j^\star$ are the coordinates of the level-set root along the edge j of the element, $\boldsymbol{x}_i$ are the coordinates of the element nodes which define edge j, and $\phi_3(\boldsymbol{x}_i)$ is the level-set value at node i. That is, two edges intersect with the zero-level set of a cut two-dimensional triangular element and three to four edges are intersected with the zero-level set of a cut three-dimensional tetrahedral element, see Fig. 3.15. It is noted that due to the definition of simplex elements also the case where four edges are cut by the zero-level set leads to a planar representation of the zero-level set, see Fig. 3.15(c). Based on the used decomposition there are three possible shapes of the zero-level sets within each simplex element: a straight line in two dimensions and a flat triangle or quadrilateral in three dimensions. The dimension of the zero-level sets is one order lower than the problem itself and can be described with $(d-1)$-dimensional standard finite elements which live in $\mathbb{R}^d$. Because these elements describe the crack geometry they are called 'crack elements' and build the basis for the surface integration which is discussed in Sec. 3.3.3.

3.3.2 Domain integration within cut elements

Assuming that no level-set function is exactly zero at a node, then each cut triangle is split into a triangular and a quadrilateral element, see Fig. 3.11 where the solid black line shows the decomposition of the reference quadrilateral element. A similar behaviour exists in three dimensions, however, there are two possibilities how the zero-level set cuts the tetrahedral element. Each cut tetrahedron is split into (i) a tetrahedron and a prism when one nodal value of the level-set function has a different sign or (ii) into two prisms when two nodes have a different sign compared to the other two. Case (i) is shown, for example, in Fig. 3.12(h) and case (ii) in Fig. 3.12(e) where the zero-level set is illustrated in the corresponding sub-element. A consistent integration is provided by subdividing each resulting sub-element which can not be reproduced by simplex elements is further subdivided into simplex elements. That is, a quadrilateral sub-element is subdivided into two triangles, see Fig. 3.11(b) where the decomposition is shown by the dashed lines or a prism is split into two tetrahedrons as shown in Figs. 3.12(d)-(i) where the decomposition is shown by the thin solid black line. These subdivisions avoid a mixture of different integration rules, for example, such as those for quadrilaterals and triangles. The domain integration is based on these simplex elements and requires 3 steps which are explained next.

(i) Define the integration points in the reference simplex elements, see Fig. 3.13(a) or

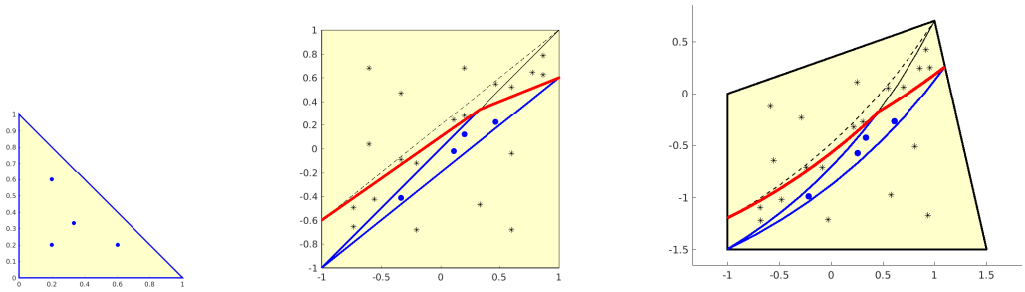

(a) (b) (c)

Figure 3.13: Mapping of the Gauss points for the two-dimensional domain integration. Position of the integration points within the (a) reference triangular element, (b) reference quadrilateral element, and (c) physical element.

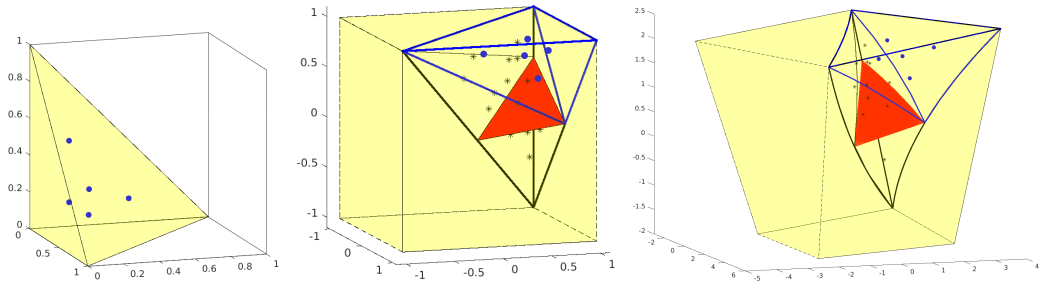

(a) (b) (c)

Figure 3.14: Mapping of the Gauss points for the three-dimensional domain integration. Position of the integration points within the (a) reference tetrahedral element, (b) reference hexahedral element, and (c) physical element.

Fig. 3.14(a).

(ii) Map these points to the corresponding sub-elements of the reference quadrilateral or hexahedral element, see Fig. 3.13(b) or Fig. 3.14(b).

(iii) Map the reference quadrilateral or hexahedral element to the physical element of the mesh, see Fig. 3.13(c) or Fig. 3.14(c).

In Figs. 3.13 and 3.14, the mapping procedure is shown from a simplex element via the subdivided sub-element to the physical element. Herein, the blue points and lines show the mapping for one element, respectively. The modification of the corresponding integration weights from the reference simplex element $\omega_i^{\boldsymbol{a}}$ to the physical element of the domain $\omega_i^{\boldsymbol{x}}$ is given by

$$\omega_i^{\boldsymbol{x}} = \omega_i^{\boldsymbol{a}} \cdot \det(\mathbf{J}_{\boldsymbol{r}}) \cdot \det(\mathbf{J}_{\boldsymbol{x}}). \tag{3.27}$$

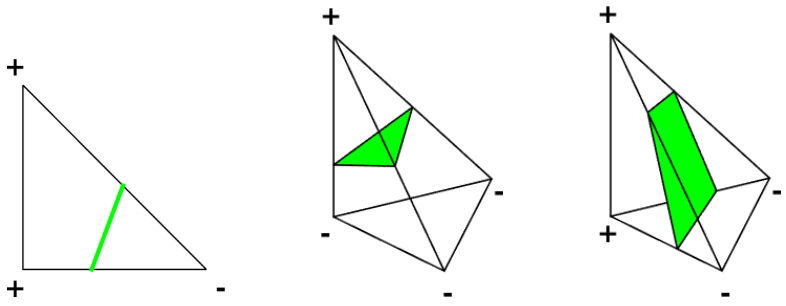

Figure 3.15: Possible shapes of the zero level-sets within one sub-element in (a) two dimensions, and in three dimensions when (b) one node has a different sign or (c) two nodes have the same sign.

Herein, $\mathbf{J}_{\boldsymbol{r}}$ is the Jacobi-matrix with respect to the mapping of the reference simplex element to the corresponding element within the sub-element and $\mathbf{J}_{\boldsymbol{x}}$ is the Jacobi-matrix with respect to the mapping of the reference background element to the physical element of the domain. It is noted that the mapping of the reference quadrilateral or hexahedral element to the physical element of the mesh in step (iii) with the bi- or tri-linear shape functions leads to *curved* representations of the mapped simplex elements in the physical space in general. Therefore, it is not possible to map the integration points directly from the reference simplex element to the physical element. The proposed method is numerically consistent and works for structured and unstructured background meshes in the same way. In the following, a similar procedure is presented for the required surface integration of loaded crack surfaces.

3.3.3 Integration of loaded crack surfaces

In the analysis of fractures, there are many applications where the crack surface is loaded, in fact, this load may be the dominant driving force of the potential propagation of the crack. Examples are corrosion and freezing processes in fractured structures. Another example is hydraulic fracturing where the pressure exerted by the fracking fluid is often the only crack opening load. Therefore, the handling of loaded crack surfaces became an important part in fracture mechanics. In this section, the focus is placed on the surface integration of the applied loading within the fracture on a purely implicitly described crack geometry which is often used in the context of the XFEM.

The basis of the surface integration are the reference elements of the 'crack elements' which are obtained by the detection of the zero-level set within the reference sub-elements, see Sec. 3.3.1. All possible shapes of the zero level-sets or the 'crack elements' are shown in Fig. 3.15 for the two and three-dimensional case. Based on these elements four steps

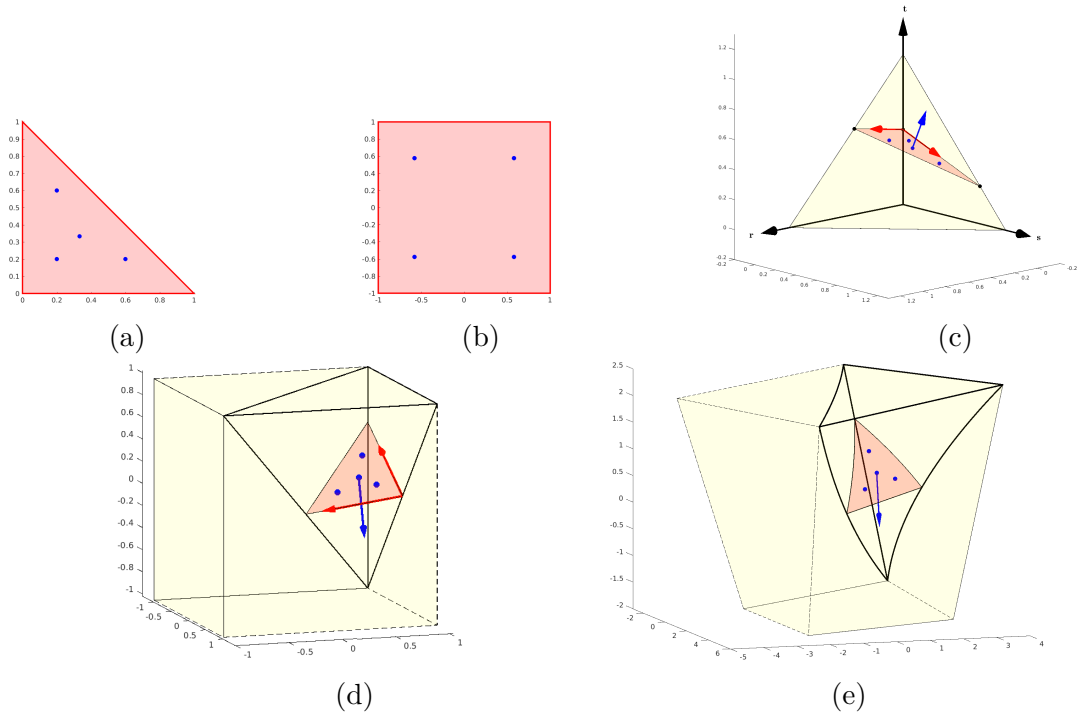

Figure 3.16: Mapping of the Gauss points for the integration of the loading on the crack surface in three dimensions.

are required to get integration points on the implicit crack surface which are explained for a tri-linear hexahedral element, representatively.

(i) Define the integration points $\boldsymbol{r}_i^\star$ in the two-dimensional reference crack element.

(ii) Map these points to the reference tetrahedral element.

(iii) Map the reference tetrahedral element to the corresponding sub-tetrahedron in the reference hexahedral element.

(iv) Map the reference hexahedral element to the physical element of the mesh.

The general procedure for generating integration points on the implicit crack surface is illustrated in Fig. 3.16 for an arbitrary three-dimensional hexahedral element. As the shape functions are discontinuous along the crack surface, the integration points have to be *'split'* into two opposite but infinitesimally close points being on either side of the crack surface. This is done between step (iii) and (iv) of the surface integration based on the unit normal vector $\boldsymbol{n}^{\boldsymbol{\xi}}$ and the shifting magnitude ε

$$\boldsymbol{r}_i^{\star\pm}(\boldsymbol{\xi}_i) = \boldsymbol{r}_i^{\star}(\boldsymbol{\xi}_i) \pm \varepsilon \boldsymbol{n}_i^{\boldsymbol{\xi}}. \tag{3.28}$$

This normal vector is given by the cross product of the two tangential vectors $\boldsymbol{t}_1^{\boldsymbol{\xi}}$ and $\boldsymbol{t}_2^{\boldsymbol{\xi}}$ which are extracted from the roots of the zero level-sets at the element edges. Based on these tangent vectors $\boldsymbol{t}$ and the Jacobi-matrices $\mathbf{J}$, the modification of the integration weights ω_i is given by

$$\omega_i^{\boldsymbol{x}} = \omega_i^{\boldsymbol{a}} \cdot \sqrt{\det(\mathbf{J}_{\boldsymbol{r}}^T \mathbf{J}_{\boldsymbol{r}})} \cdot \frac{||\mathbf{J}_{\boldsymbol{\xi}} \boldsymbol{t}_1^r \times \mathbf{J}_{\boldsymbol{\xi}} \boldsymbol{t}_2^r||}{||\boldsymbol{t}_1^r \times \boldsymbol{t}_2^r||} \cdot \frac{||\mathbf{J}_{\boldsymbol{x}} \boldsymbol{t}_1^{\boldsymbol{\xi}} \times \mathbf{J}_{\boldsymbol{x}} \boldsymbol{t}_2^{\boldsymbol{\xi}}||}{||\boldsymbol{t}_1^{\boldsymbol{\xi}} \times \boldsymbol{t}_2^{\boldsymbol{\xi}}||} \tag{3.29}$$

It is noted that the first mapping requires the Gram's determinant as a $(d-1)$-dimensional element is mapped to $\mathbb{R}^d$. The other mappings take into account that an area is projected instead of a volume. Quadrilateral zero-level sets within the reference tetrahedral element are handled in the same way because they remain planar within the reference hexahedral element. This procedure applies analogously to background meshes discretized by tetrahedral elements where the situation is simplified because the zero level-sets stay naturally flat even in the physical element. The obtained integration points shall later also be used for the computation of stress intensity factors (SIFs) which is discussed in Sec. 6.1. Different stresses and loadings of crack surfaces are discussed in Sec. 5.

3.4 Computation of displacements

In the previous sections, the approximation of a LEFM problem was discussed in the context of the XFEM. In particular, the definition of enriched nodes, the enrichment functions based on customary coordinate system, numerical integration of the domain and surface loadings were investigated based on a hybrid explicit-implicit crack description. This section deals with the determination of the displacement field of a fractured isotropic material with the XFEM based on the governing equations of linear elasticity. Following the same procedure as the classical FEM, the weak form of the governing equations can be used to obtain a system of equations for the nodal degrees of freedom,

$$\mathbf{K} \cdot \boldsymbol{u} = \boldsymbol{f}, \tag{3.30}$$

In an XFEM-context, the number of degrees of freedom per node varies due to the structure of enriched approximation, see Eq. 3.40. equivalent to a standard FEM approximation. Herein, $\mathbf{K}$ is known as stiffness matrix, $\boldsymbol{u}$ represents the (displacement) unknows and $\boldsymbol{f}$ is the load vector. Differences between the classical FEM and the XFEM only exist in the employed approximation spaces resulting in consequences for the element matrices as discussed below.

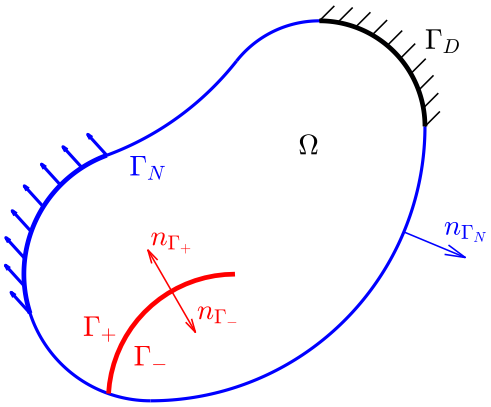

Figure 3.17: Definitions of the boundaries Γ_D, Γ_N, Γ_+ and Γ_- their corresponding normal vectors.

3.4.1 Governing equations

A cracked domain Ω is considered with its boundary being decomposed into the sets Γ_D, Γ_N, Γ_+ and Γ_-, such that $\Gamma = \Gamma_D \cup \Gamma_N \cup \Gamma_+ \cup \Gamma_-$ as shown in Fig. 3.17. Γ_+ and Γ_- describe the two crack faces of a given crack path/surface Γ_C such that $\Gamma_C = \Gamma_+ \cup \Gamma_-$. Prescribed displacements are imposed on Γ_D, while tractions are imposed on Γ_N and Γ_C. Based on these definitions the equilibrium equations and boundary conditions are defined as

$$\nabla \cdot \boldsymbol{\sigma} + \boldsymbol{f} = \boldsymbol{0} \quad \text{in } \Omega, \tag{3.31}$$

$$\boldsymbol{u} = \boldsymbol{u}_D \quad \text{on } \Gamma_D, \tag{3.32}$$

$$\boldsymbol{\sigma} \cdot \boldsymbol{n}_{\Gamma_N} = \boldsymbol{t}_N \quad \text{on } \Gamma_N, \tag{3.33}$$

$$\boldsymbol{\sigma} \cdot \boldsymbol{n}_{\Gamma_C} = \boldsymbol{t}_C \quad \text{on } \Gamma_C. \tag{3.34}$$

In many practical applications, it is assumed that either the crack faces are stress-free or that the exerted loading has a hydro-static behaviour within the fracture, wherefore the applied tractions $\boldsymbol{t}_C$ may be expressed at the crack surfaces $\Gamma_\pm$ by

$$\boldsymbol{t}_C = \begin{cases} \boldsymbol{0} & \text{for stress-free crack surfaces,} \\ p \cdot \boldsymbol{n}_{\Gamma_\pm} & \text{under a hydro-static loading, i.e., pressure.} \end{cases} \tag{3.35}$$

The general formulation of Eq. 3.34 is required for the conversion of boundary tractions into equivalent face tractions, see Sec. 2.2.4. The Cauchy stress tensor $\boldsymbol{\sigma}$ for an isotropic material is defined as

$$\boldsymbol{\sigma} = \lambda \mathrm{tr}(\boldsymbol{\varepsilon})\mathbf{I} + 2\mu\boldsymbol{\varepsilon}, \tag{3.36}$$

where the linear strain tensor $\boldsymbol{\varepsilon}$ can be expressed with the strain-displacement relation

$$\boldsymbol{\varepsilon} = \frac{1}{2}\left(\nabla \boldsymbol{u} + (\nabla \boldsymbol{u})^T\right), \tag{3.37}$$

which is valid for small strain and small displacements. The relation between the strains $\boldsymbol{\varepsilon}$ and the stresses $\boldsymbol{\sigma}$ is based on the second Lamé-Constant μ (Eq. 2.14) and the first Lamé-Constant λ with

$$\lambda = \begin{cases} \dfrac{E\nu}{(1+\nu)(1-2\nu)} & \text{for plane strain,} \\ \dfrac{E\nu}{1-\nu^2} & \text{for plane stress.} \end{cases} \tag{3.38}$$

It is noted that only the plane strain expression of Eq. 3.38 is useful in three dimensions.

3.4.2 Resulting system of equations

The usual steps in any finite element procedure are to start from a boundary value problem in strong form as given in Eqs. 3.32 to 3.34. These equations (i) are multiplied with test functions $\boldsymbol{w}$, (ii) integrated over the domain, and (iii) the divergence theorem is applied in order to shift derivatives onto the test functions. The result is a weak formulation of the boundary value problem [110],

$$\int_\Omega \nabla \boldsymbol{w} : \boldsymbol{\sigma} d\Omega - \int_\Gamma \boldsymbol{w} \cdot \boldsymbol{t} d\Gamma - \int_\Omega \boldsymbol{w} \cdot \boldsymbol{f} d\Omega = 0. \tag{3.39}$$

$\boldsymbol{w}$ represent the test functions and Γ is the boundary which consists of Γ_N and Γ_C. The applied tractions on Γ_N and Γ_C are treated in the same manner, wherefore no additional terms are required in Eq. 3.39 for the discontinuity Γ_C. In this sense, Γ_C corresponds to Γ_N.

The next step is to *discretize* the weak form (Eq. 3.39). Then, the task is to find the one approximation $\boldsymbol{u}^h$ according to Eq. 3.40 such that this discrete weak form is fulfilled for all test functions $\boldsymbol{w}^h$:

$$\int_\Omega \nabla \boldsymbol{w}^h : \boldsymbol{\sigma}(\varepsilon^h(\boldsymbol{u}^h)) d\Omega - \int_\Gamma \boldsymbol{w}^h \cdot \boldsymbol{t} d\Gamma - \int_\Omega \boldsymbol{w}^h \cdot \boldsymbol{f} d\Omega = 0, \tag{3.40}$$

with $\boldsymbol{u}^h$ being the extended approximation of Eq. 3.21. The test functions $\boldsymbol{w}^h$ are chosen identically in a Bubnov-Galerkin scheme. This results in a system of equations (Eq. 3.30) for the nodal degrees of freedom. In the FEM and XFEM, this system of equations is assembled by element contributions which are discussed in detail next.

The element stiffness matrix $\mathbf{K}^{\text{elem}}$ and the corresponding load vector $\boldsymbol{f}^{\text{elem}}$ can be defined in a formally equivalent way for the XFEM and the FEM. That is, $\mathbf{K}^{\text{elem}}$ is given in two dimensions as

$$\mathbf{K}_{\text{2D}}^{\text{elem}} = \int \begin{bmatrix} (\lambda+2\mu)\boldsymbol{N}_{,x}\boldsymbol{N}_{,x}^T + \mu\boldsymbol{N}_{,y}\boldsymbol{N}_{,y}^T & \lambda\boldsymbol{N}_{,x}\boldsymbol{N}_{,y}^T + \mu\boldsymbol{N}_{,y}\boldsymbol{N}_{,x}^T \\ \lambda\boldsymbol{N}_{,y}\boldsymbol{N}_{,x}^T + \mu\boldsymbol{N}_{,x}\boldsymbol{N}_{,y}^T & (\lambda+2\mu)\boldsymbol{N}_{,y}\boldsymbol{N}_{,y}^T + \mu\boldsymbol{N}_{,x}\boldsymbol{N}_{,x}^T \end{bmatrix} d\Omega \tag{3.41}$$

and the corresponding load vector as

$$\boldsymbol{f}_{\text{2D}}^{\text{elem}} = \begin{pmatrix} \int \boldsymbol{N} t_x d\Gamma + \int \boldsymbol{N} f_x d\Omega \\ \int \boldsymbol{N} t_y d\Gamma + \int \boldsymbol{N} f_y d\Omega \end{pmatrix}. \tag{3.42}$$

In three dimensions, the element stiffness matrix K^{elem} is defined as follows

$$\mathbf{K}_{\text{3D}}^{\text{elem}} = \int \begin{bmatrix} K_{xx} & K_{xy} & K_{xz} \\ & K_{yy} & K_{yz} \\ \text{sym.} & & K_{zz} \end{bmatrix} d\Omega \tag{3.43}$$

with

$$\begin{aligned} K_{xx} &= (\lambda+2\mu)\boldsymbol{N}_{,x}\boldsymbol{N}_{,x}^T + \mu\boldsymbol{N}_{,y}\boldsymbol{N}_{,y}^T + \mu\boldsymbol{N}_{,z}\boldsymbol{N}_{,z}^T, && (3.44)\\ K_{xy} &= \lambda\boldsymbol{N}_{,x}\boldsymbol{N}_{,y}^T + \mu\boldsymbol{N}_{,y}\boldsymbol{N}_{,x}^T, && (3.45)\\ K_{xz} &= \lambda\boldsymbol{N}_{,x}\boldsymbol{N}_{,z}^T + \mu\boldsymbol{N}_{,z}\boldsymbol{N}_{,x}^T, && (3.46)\\ K_{yy} &= (\lambda+2\mu)\boldsymbol{N}_{,y}\boldsymbol{N}_{,y}^T + \mu\boldsymbol{N}_{,x}\boldsymbol{N}_{,x}^T + \mu\boldsymbol{N}_{,z}\boldsymbol{N}_{,z}^T, && (3.47)\\ K_{yz} &= \lambda\boldsymbol{N}_{,y}\boldsymbol{N}_{,z}^T + \mu\boldsymbol{N}_{,z}\boldsymbol{N}_{,y}^T, && (3.48)\\ K_{yy} &= (\lambda+2\mu)\boldsymbol{N}_{,z}\boldsymbol{N}_{,z}^T + \mu\boldsymbol{N}_{,x}\boldsymbol{N}_{,x}^T + \mu\boldsymbol{N}_{,y}\boldsymbol{N}_{,y}^T, && (3.49) \end{aligned}$$

and the corresponding load vector with

$$\boldsymbol{f}_{\text{3D}}^{\text{elem}} = \begin{pmatrix} \int \boldsymbol{N} t_x d\Gamma + \int \boldsymbol{N} f_x d\Omega \\ \int \boldsymbol{N} t_y d\Gamma + \int \boldsymbol{N} f_y d\Omega \\ \int \boldsymbol{N} t_z d\Gamma + \int \boldsymbol{N} f_z d\Omega \end{pmatrix}. \tag{3.50}$$

Although the expressions of Eqs. 3.41-3.50 are for the XFEM and standard FEM equivalent, the definition of the shape functions in $\boldsymbol{N}$ is different in the two methods. In the standard FEM, $\boldsymbol{N}$ is a $k \times 1$- vector which is composed of the shape functions N_i and k being the number of nodes per element. In the XFEM, depending on the number of enriched nodes and their associated enrichment functions, the size of $\boldsymbol{N}$ varies between the different types of element. For example, the length of $\boldsymbol{N}$ is for two- and three-dimensional reproducing elements as follows

$$\text{length}(\boldsymbol{N}) = \begin{cases} 2 \cdot k & \text{for step-enriched elements,} \\ 5 \cdot k & \text{for tip-enriched elements.} \end{cases} \tag{3.51}$$

That is, the number of global degrees of freedom varies from element to element which complicates the implementation. In a LEFM problem with XFEM, $\boldsymbol{N}$ consists not only of the standard FE shape functions N_i but also of the enriched shape functions $N_i\psi(\boldsymbol{x})$ which leads to following structure

$$\boldsymbol{N} = \begin{pmatrix} \begin{bmatrix} N_1(\boldsymbol{x}), ..., N_k(\boldsymbol{x}) \end{bmatrix}^T \\ \begin{bmatrix} N_1(\boldsymbol{x})\psi_{\text{step}}^{\text{shift,1}}(\boldsymbol{x}), ..., N_k(\boldsymbol{x})\psi_{\text{step}}^{\text{shift,k}}(\boldsymbol{x}) \end{bmatrix}^T \\ \begin{bmatrix} N_1(\boldsymbol{x})\psi_{\text{tip}}^{1,\text{shift,1}}(r,\theta), ..., N_k(\boldsymbol{x})\psi_{\text{tip}}^{1,\text{shift,k}}(r,\theta) \end{bmatrix}^T \\ \begin{bmatrix} N_1(\boldsymbol{x})\psi_{\text{tip}}^{2,\text{shift,1}}(r,\theta), ..., N_k(\boldsymbol{x})\psi_{\text{tip}}^{2,\text{shift,k}}(r,\theta) \end{bmatrix}^T \\ \begin{bmatrix} N_1(\boldsymbol{x})\psi_{\text{tip}}^{3,\text{shift,1}}(r,\theta), ..., N_k(\boldsymbol{x})\psi_{\text{tip}}^{3,\text{shift,k}}(r,\theta) \end{bmatrix}^T \\ \begin{bmatrix} N_1(\boldsymbol{x})\psi_{\text{tip}}^{4,\text{shift,1}}(r,\theta), ..., N_k(\boldsymbol{x})\psi_{\text{tip}}^{4,\text{shift,k}}(r,\theta) \end{bmatrix}^T \end{pmatrix}. \tag{3.52}$$

It is noted that Eq. 3.52 represents the structure of an element where all enriched shape functions are present. Depending on the individual situation in an element, some of these (nodal) shape functions are absent. This general representation is used to demonstrate the order of the stored shape functions. Based on this structure the corresponding (three-

dimensional) degrees of freedom are

$$\boldsymbol{u} = \begin{pmatrix} \left[u_{1x},...,u_{kx},\quad a_{1x},...,a_{kx},\quad b^1_{1x},...,b^1_{kx},\quad b^2_{1x},...,b^2_{kx},\quad b^3_{1x},...,b^3_{kx},\quad b^4_{1x},...,b^4_{kx}\right]^T \\ \left[u_{1y},...,u_{ky},\quad a_{1y},...,a_{ky},\quad b^1_{1y},...,b^1_{ky},\quad b^2_{1y},...,b^2_{ky},\quad b^3_{1y},...,b^3_{ky},\quad b^4_{1y},...,b^4_{ky}\right]^T \\ \left[u_{1z},...,u_{kz},\quad a_{1z},...,a_{kz},\quad b^1_{1z},...,b^1_{kz},\quad b^2_{1z},...,b^2_{kz},\quad b^3_{1z},...,b^3_{kz},\quad b^4_{1z},...,b^4_{kz}\right]^T \end{pmatrix}. \tag{3.53}$$

The global system of equation is often assembled in such a way that the different types of degrees of freedom ($\boldsymbol{u}$, $\boldsymbol{a}$ and $\boldsymbol{b}^j$) are grouped together which simplifies the localization of the individual degrees of freedom and ensures banded stiffness matrices $\mathbf{K}$.

3.4.3 Global derivatives of enriched shape functions

In the weak form, derivatives with respect to the global coordinates $\boldsymbol{x}$ occur naturally. In a finite element context, where shape functions are defined over reference elements with coordinates $\boldsymbol{\xi} = (\xi, \eta, \zeta)$, one has to establish a relation between these coordinate systems. As a result of the chain rule, this relation is given by the (transposed) inverse of the Jacobi-matrix,

$$N_{,\boldsymbol{x}} \;=\; \mathbf{J}^{-T} \cdot N_{,\boldsymbol{\xi}} \tag{3.54}$$

$$\begin{pmatrix} \frac{\partial N}{\partial x} \\ \frac{\partial N}{\partial y} \\ \frac{\partial N}{\partial z} \end{pmatrix} \;=\; \begin{bmatrix} \frac{\partial x}{\partial \xi} & \frac{\partial y}{\partial \xi} & \frac{\partial z}{\partial \xi} \\ \frac{\partial x}{\partial \eta} & \frac{\partial y}{\partial \eta} & \frac{\partial z}{\partial \eta} \\ \frac{\partial x}{\partial \zeta} & \frac{\partial y}{\partial \zeta} & \frac{\partial z}{\partial \zeta} \end{bmatrix}^{-1} \cdot \begin{pmatrix} \frac{\partial N}{\partial \xi} \\ \frac{\partial N}{\partial \eta} \\ \frac{\partial N}{\partial \zeta} \end{pmatrix}. \tag{3.55}$$

In the XFEM, the same applies also to the enrichment functions which is outlined here in x-direction,

$$\frac{\partial}{\partial x}\left[N_i(\boldsymbol{x})\psi^{\text{shift,i}}_{\text{step}}(\boldsymbol{x})\right] = \frac{\partial N_i(\boldsymbol{x})}{\partial x}\psi^{\text{shift,i}}_{\text{step}}(\boldsymbol{x}), \tag{3.56}$$

and

$$\frac{\partial}{\partial x}\left[N_i(\boldsymbol{x})\psi^{\text{j,shift,i}}_{\text{tip}}(r,\theta)\right] = \frac{\partial N_i(\boldsymbol{x})}{\partial x}\psi^{\text{j,shift,i}}_{\text{tip}}(r,\theta) + \frac{\partial \psi^{\text{j}}_{\text{tip}}(r,\theta)}{\partial x}N_i(\boldsymbol{x}) \tag{3.57}$$

with

$$\frac{\partial \psi^{\text{j}}_{\text{tip}}(r,\theta)}{\partial x} = \frac{\partial \psi^{\text{j}}_{\text{tip}}(r,\theta)}{\partial r}\frac{\partial r}{\partial x} + \frac{\partial \psi^{\text{j}}_{\text{tip}}(r,\theta)}{\partial \theta}\frac{\partial \theta}{\partial x}. \tag{3.58}$$

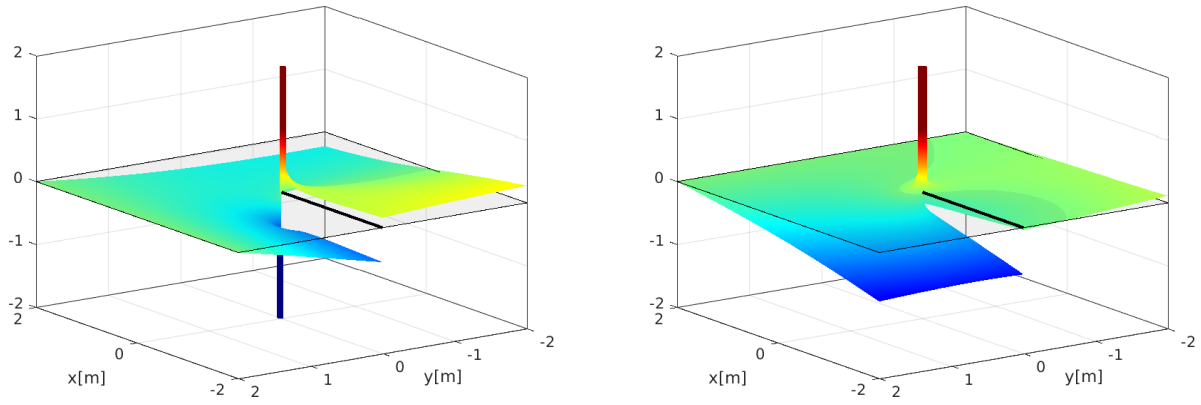

(a) $\frac{\partial}{\partial x}\left[N_1 \cdot \psi_{\text{tip}}^{2,\text{shift},1}(r,\theta)\right]$. (b) $\frac{\partial}{\partial y}\left[N_1 \cdot \psi_{\text{tip}}^{2,\text{shift},1}(r,\theta)\right]$.

Figure 3.18: Global derivatives of the local crack-tip enrichment function $N_1\psi_{\text{tip}}^{2,\text{shift},1}(r,\theta)$.

Furthermore, the global derivatives of the polar coordinates r and θ are obtained with Eqs. 3.13-3.16 and are needed for the derivatives of the tip enrichment functions. It is noted that the global derivatives of $\psi_{\text{step}}^{\text{shift,i}}(\boldsymbol{x})$ are 0 within the domain, wherefore there are no additional terms in Eq. 3.56. Fig. 3.18 shows the global derivatives of the enriched shape function $N_1 \cdot \psi_{\text{tip}}^{2,\text{shift},1}(r,\theta)$ within the crack-tip element. Herein, the crack is aligned with respect to the x-direction and has its crack-tip at the coordinates $[0,0]$. As can be seen, the global derivatives are singular at the crack-tip due to the $\sqrt{r}$-behaviour of $\psi_{\text{tip}}^{\text{j}}(r,\theta)$. As a consequence, advanced quadrature schemes are required within these elements containing the crack-tip/front [129, 181].

3.5 Comparison of XFEM and FEM in LEFM

In this section, the differences between XFEM and FEM simulations of LEFM problems are discussed and are illustrated based on simple test cases in two and three dimensions. Additionally, the concept of the XFEM approach in LEFM is proved by comparing the obtained results with those obtained from an equivalent standard finite element approach.

In the XFEM, the domain discretization can be performed independently of the crack geometry which is not possible with the classical FEM. Singular stresses at the crack-tip/front are considered within the XFEM by the corresponding crack-tip enrichments (Eq. 3.20) while the FEM requires locally refined meshes, see Fig. 3.20. Surface integrations are necessary to deal with pressurized crack surfaces within the XFEM, see Sec. 3.3.3. In contrast, such integrations are not required in the FEM because loaded crack surfaces are considered through Neumann boundary conditions. It is noted that only constant pressure distributions are considered here because a suitable description of an arbitrary pressure distribution on the implicitly defined crack geometry has not yet been discussed

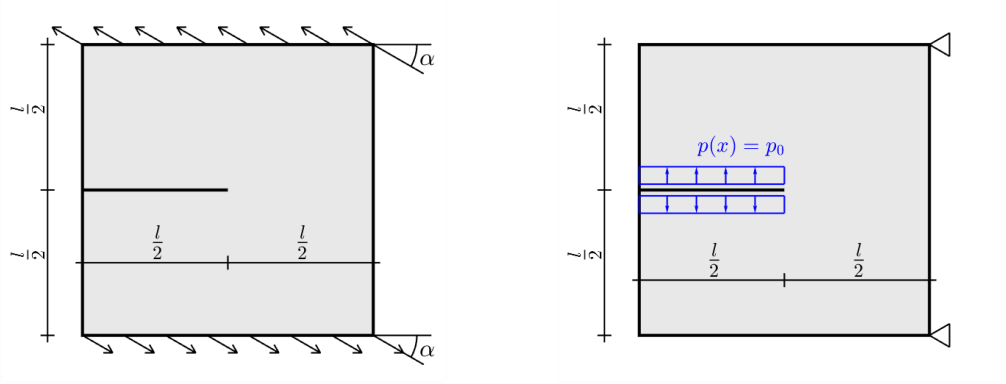

Figure 3.19: Edge crack in a squared plate which is opened through (a) prescribed displacements at the boundary (TC-1) or (b) through an applied pressure within the fracture (TC-2).

here. How more complex loadings can be applied in the context of the XFEM with a hybrid explicit-implicit crack description is discussed in Sec. 5 which is a focus of this thesis. For all test cases a brittle and isotropic material is used with a Poisson's ratio $\nu = 0.3$ and a Young's modulus $E = 30\,\text{GPa}$. Each mesh is based on bilinear 4-node quadrilateral or trilinear 8-node hexahedral elements. Comparable results of the two simulation methods are obtained by using meshes with almost the same element sizes.

3.5.1 Two-dimensional test cases

An edge cracked rectangular plate with the extent $l = 2\,\text{m}$ and an initial crack length $l_c = 1\,\text{m}$ is investigated due to different boundary conditions. In the first test case (TC-1), the displacements are prescribed on the upper and lower side of the domain with 5 mm in direction of the specified angle $\alpha = 60\,°$, as illustrated in Fig. 3.19(a). These boundary conditions produce an opening of the crack, wherefore no other loadings are needed. The second test case (TC-2) is used to verify implementation aspects of the surface integration. Herein, the right corner nodes of the domain are fixed and a uniform pressure $p_0 = 0.1\,\text{GPa}$ is applied within the fracture, see Fig. 3.19(b). The XFEM simulation is based on a structured background mesh which consists of 51×51-elements. One straight line-segment is used to explicitly define the crack geometry. 50×50-elements are used to discretize the domain within the FEM simulation. This mesh is locally refined in the vicinity of the crack-tip which leads to a total number of 2 524 elements. An illustration of the two mesh types is given in Fig. 3.20. The obtained results are shown for both test cases in Figs. 3.21 and 3.22. There, the global displacements u_x and u_y are shown in Figs. 3.21(a-d) and 3.22(a-d) and the resulting crack opening stresses σ_{yy} are

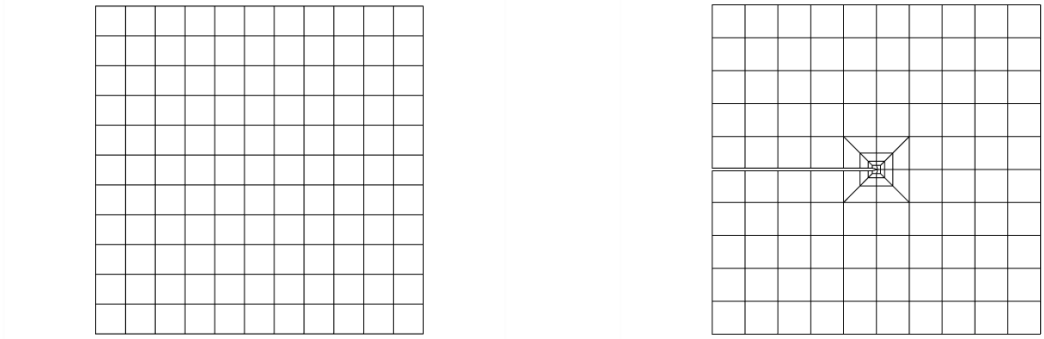

(a) (b)

Figure 3.20: Structure of the mesh within (a) XFEM and (b) FEM.

illustrated in Figs. 3.21(e-f) and 3.22(e-f) along a line which is aligned with the crack and is located infinitesimally close above the crack. It can be seen that both approaches lead to almost identical displacement and stress fields. Furthermore, the crack opening stresses σ_{yy} along the crack are in good agreement with the expected stresses which are almost 0 in TC-1 where stress-free crack surfaces are assumed and are almost $-0.1\,\mathrm{GPa}$ in TC-2 which agrees with the applied load p_0.

3.5.2 Three-dimensional test cases

The three-dimensional test cases represent extensions of the two-dimensional cases where the cracked configurations of TC-1 and TC-2 are extended in the third direction as described next. TC-3 and TC-4 investigate an edge cracked cube-shaped domain ($2\,\mathrm{m} \times 2\,\mathrm{m} \times 2\,\mathrm{m}$) under similar boundary conditions as in TC-1 and TC-2. In particular, TC-3 is loaded by prescribed displacements on the upper and lower side of the domain, see Fig. 3.23(a). The applied boundary conditions $\boldsymbol{u}_D$ are given with

$$\boldsymbol{u}_D^{\mathrm{up}} = \Delta u_{\mathrm{D}} \cdot \begin{pmatrix} -\cos(\alpha_D) \\ \sin(\alpha_D) \\ \sin(\alpha_D) \end{pmatrix}, \qquad \text{and } \boldsymbol{u}_D^{\mathrm{below}} = \Delta u_{\mathrm{D}} \cdot \begin{pmatrix} \cos(\alpha_D) \\ -\sin(\alpha_D) \\ -\sin(\alpha_D) \end{pmatrix}, \tag{3.59}$$

with $\Delta u_{\mathrm{D}} = 5\,\mathrm{mm}$ and $\alpha_D = 60\,^\circ$. These boundary conditions lead to a fully three-dimensional configuration, wherefore no equivalent two-dimensional formulation can be used. In TC-4, the crack and domain geometry of TC-3 is investigated due to a uniform pressure $p_0 = 0.1\,\mathrm{GPa}$ within the fracture. Zero displacement conditions are applied at the

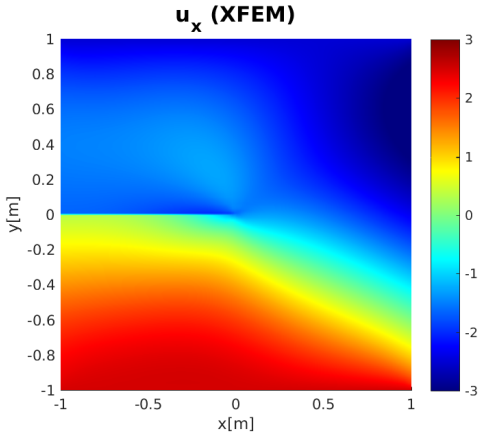

(a) TC-1: u_x [mm] with XFEM.

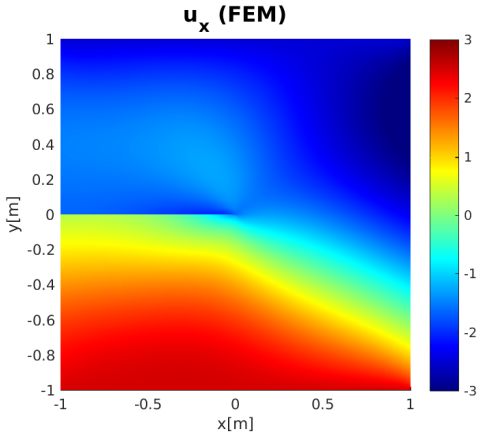

(b) TC-1: u_x [mm] with FEM.

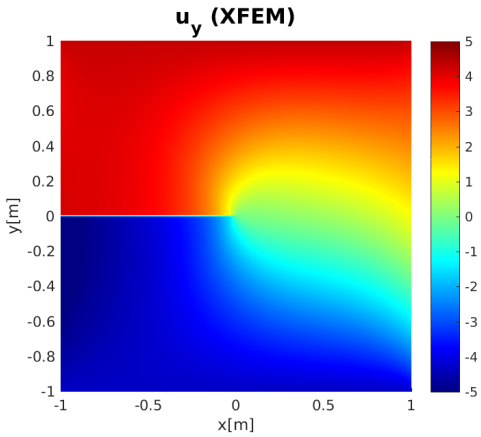

(c) TC-1: u_y [mm] with XFEM.

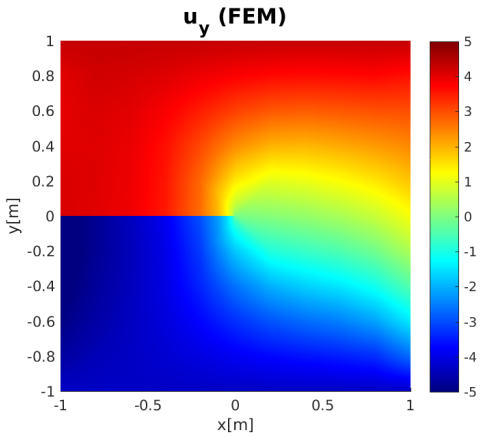

(d) TC-1: u_y [mm] with FEM.

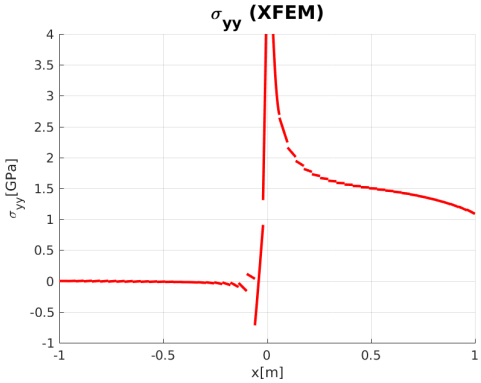

(e) TC-1: σ_{yy} [GPa] with XFEM.

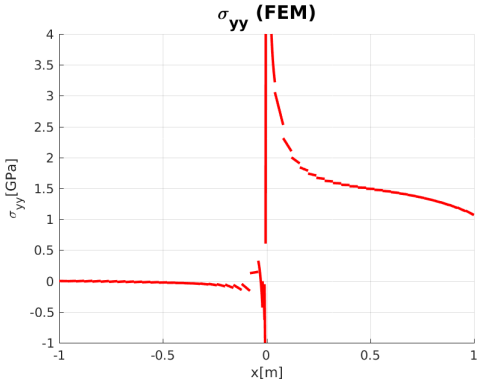

(f) TC-1: σ_{yy} [GPa] with FEM.

Figure 3.21: Comparison of the XFEM and FEM results due to prescribed displacements at the boundary in two dimensions.

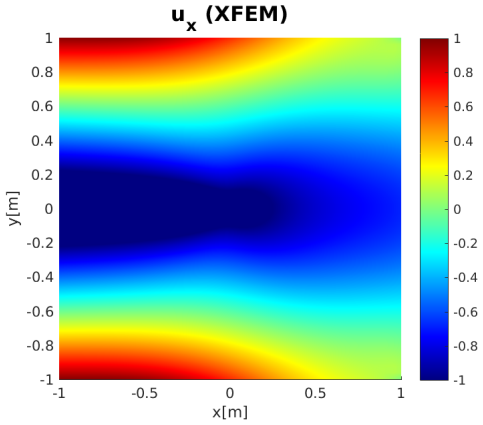

(a) TC-2: u_x [mm] with XFEM.

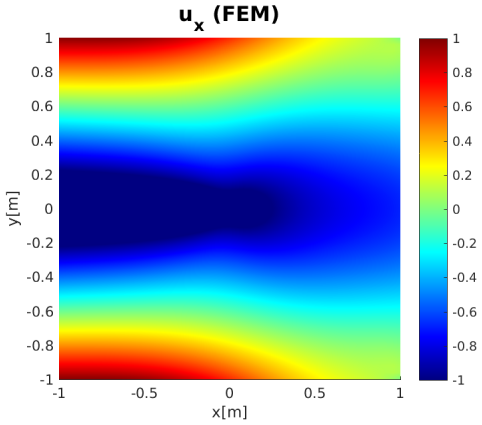

(b) TC-2: u_x [mm] with FEM.

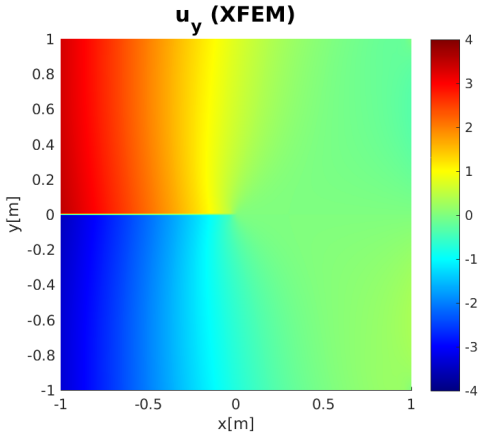

(c) TC-2: u_y [mm] with XFEM.

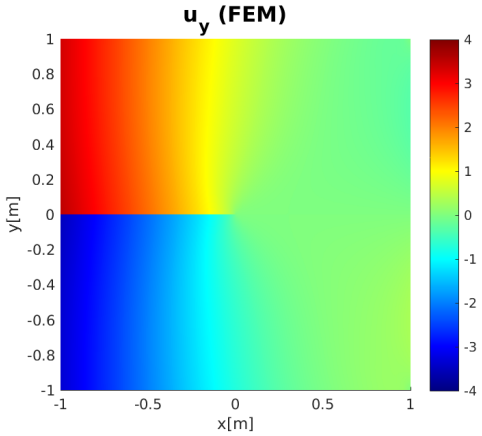

(d) TC-2: u_y [mm] with FEM.

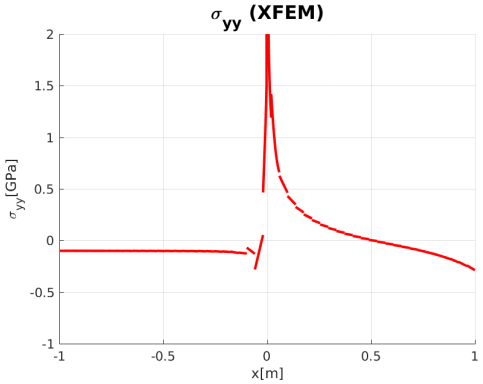

(e) TC-2: σ_{yy} [GPa] with XFEM.

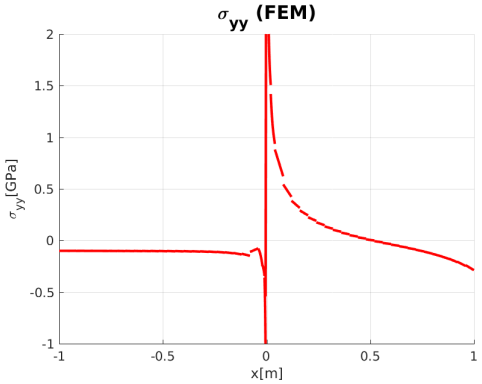

(f) TC-2: σ_{yy} [GPa] with FEM.

Figure 3.22: Comparison of the XFEM and FEM results due to a constant pressure within the fracture in two dimensions.

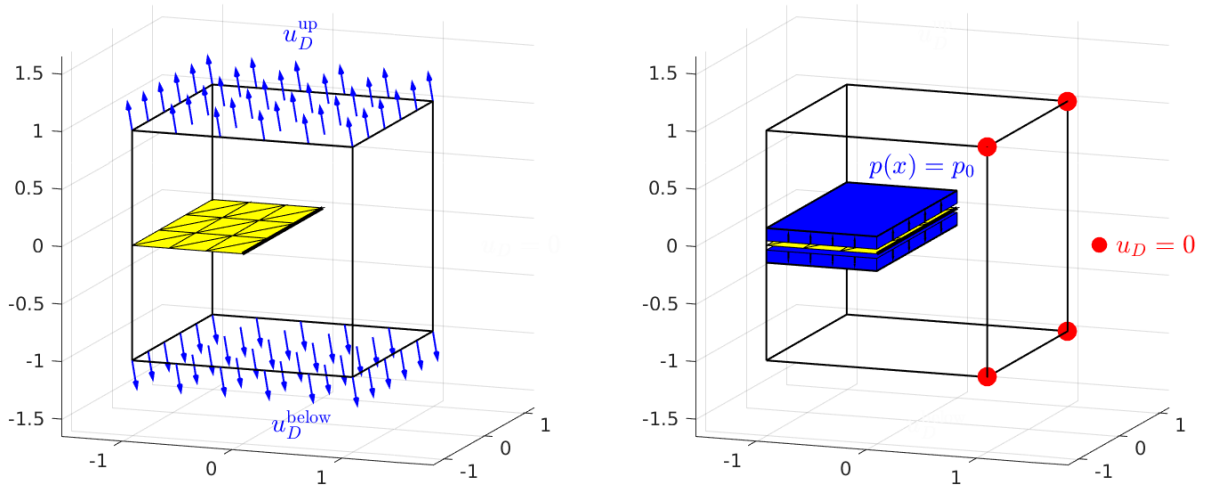

(a) (b)

Figure 3.23: Edge crack in a cube-shaped domain which is opened through (a) prescribed displacements at the boundary (TC-3) or (b) through an applied pressure within the fracture (TC-4).

right corner nodes of the discretized domain, see Fig. 3.23(b). It is noted that the required three-dimensional meshes of TC-3 and TC-4 are obtained from the extrusions of the two-dimensional meshes of the corresponding two-dimensional test cases, see Sec. 3.5.1. A domain discretization of 19×19×19 trilinear hexahedral elements is used within the XFEM approximation, wherein, 18 flat triangular elements explicitly describe the crack geometry (this number 18 is freely chosen as only 2 flat triangles would have been sufficient for this simple, flat crack geometry). The FEM simulations are based on a domain discretization which consists of 20 × 20 × 20-elements which is locally refined in the vicinity of the crack-front. Figs. 3.24(a-f) or Figs. 3.24(a-f) show the three displacement components of the solution of TC-3 or TC-4 along an xy-plane which is located infinitesimally close above the crack surface. The corresponding normal stresses σ_{zz} of this plane are shown in Figs. 3.24(g-h) or Figs. 3.24(g-h) for a chosen y-value ($y = 0$).

These test cases illustrate the major differences between the XFEM and the FEM in LEFM. It can be seen that the FEM requires suitable meshes which can be cumbersome, in particular, for more complex three-dimensional crack geometries and, in particular, when crack *propagation* is considered. For these simple test cases, the achieved results (displacements and stresses) with the XFEM are in good agreement with those obtained from the FEM. We conclude that the applied XFEM concept offers a powerful simulation tool for rather coarse meshes in LEFM.

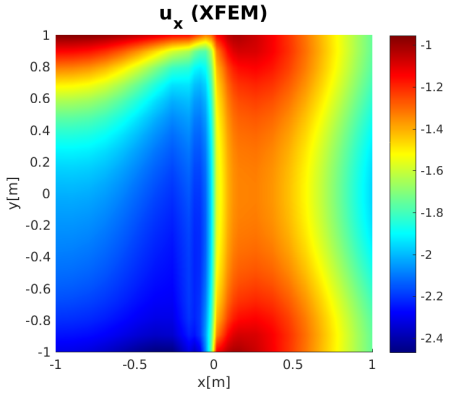

(a) TC-3: u_x [mm] with XFEM.

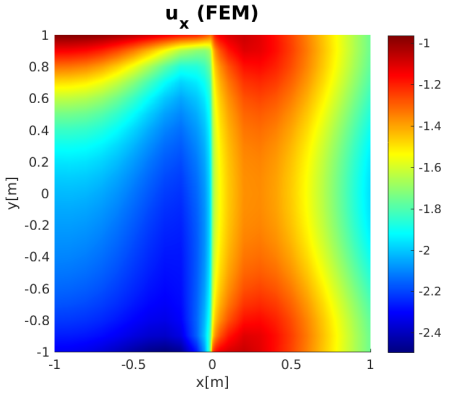

(b) TC-3: u_x [mm] with FEM.

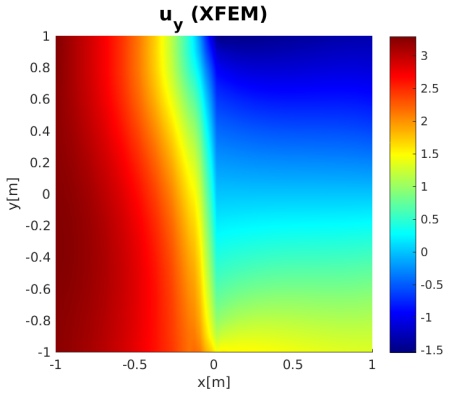

(c) TC-3: u_y [mm] with XFEM.

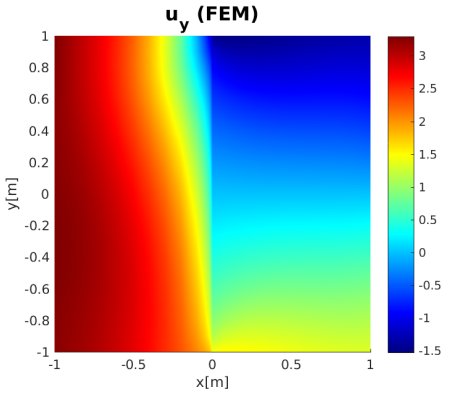

(d) TC-3: u_y [mm] with FEM.

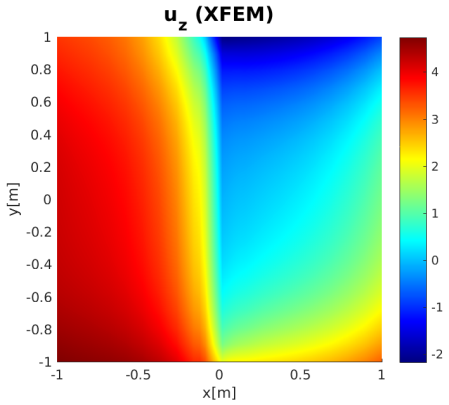

(e) TC-3: u_z [mm] with XFEM.

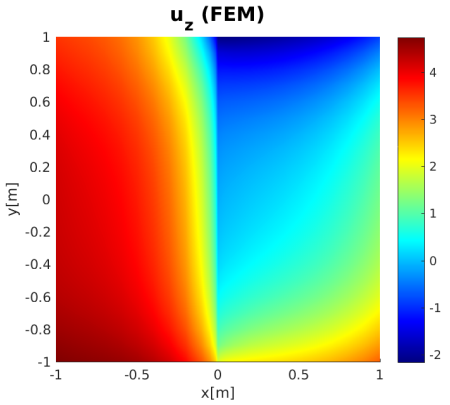

(f) TC-3: u_z [mm] with FEM.

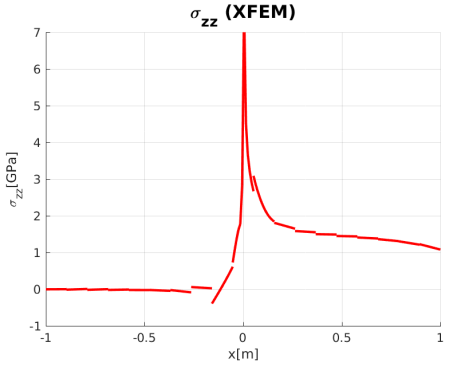

(g) TC-3: σ_{zz} [GPa] with XFEM.

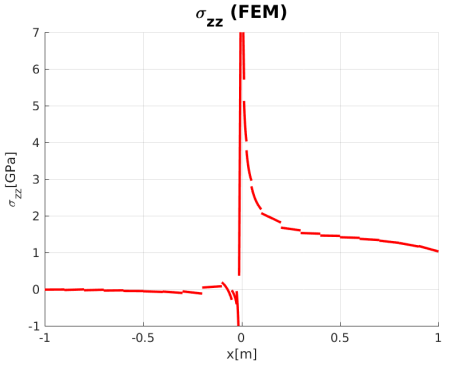

(h) TC-3: σ_{zz} [GPa] with FEM.

Figure 3.24: Comparison of the XFEM and FEM results due to prescribed displacements at the boundary in three dimensions.

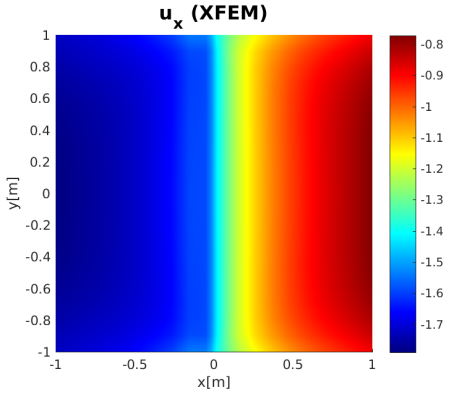

(a) TC-4: u_x [mm] with XFEM.

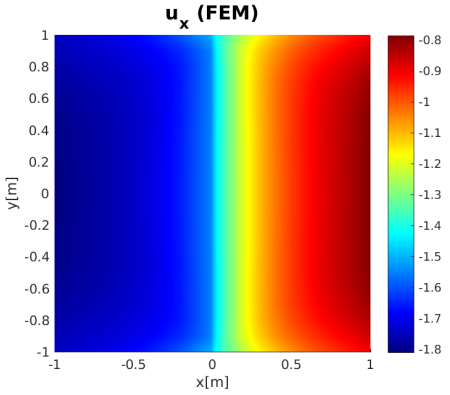

(b) TC-4: u_x [mm] with FEM.

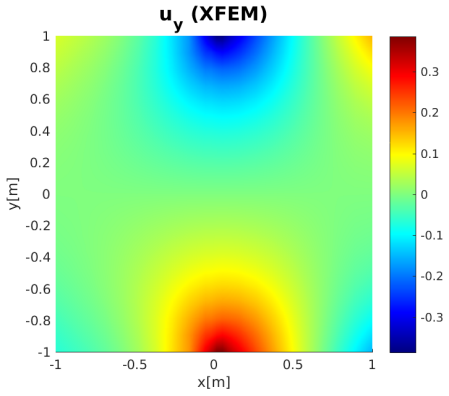

(c) TC-4: u_y [mm] with XFEM.

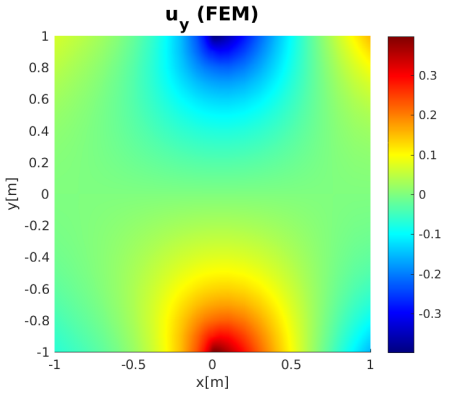

(d) TC-4: u_y [mm] with FEM.

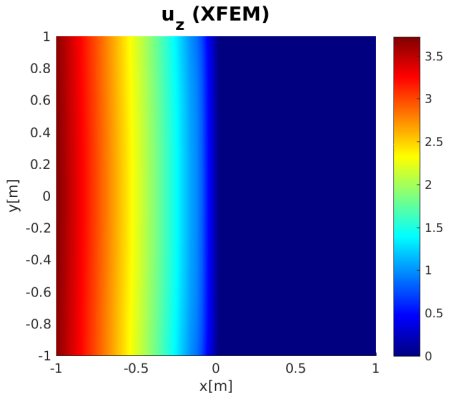

(e) TC-4: u_z [mm] with XFEM.

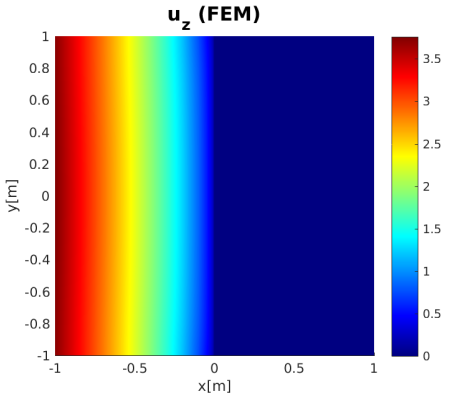

(f) TC-4: u_z [mm] with FEM.

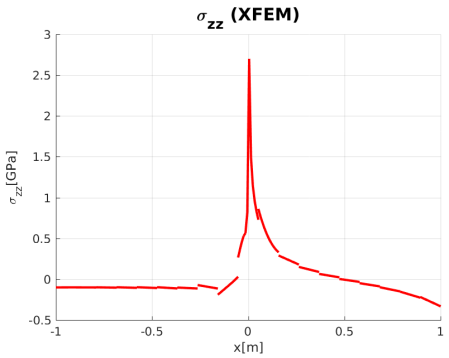

(g) TC-4: σ_{zz} [GPa] with XFEM.

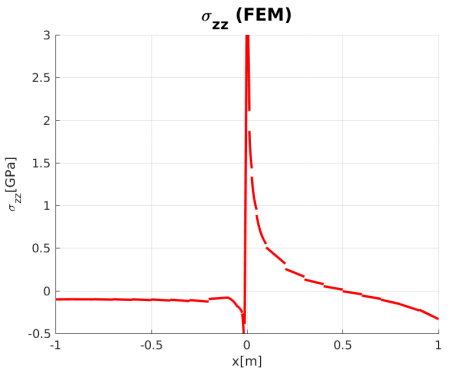

(h) TC-4: σ_{zz} [GPa] with FEM.

Figure 3.25: Comparison of the XFEM and FEM results due to a constant pressure within the fracture in three dimensions.

4 Coordinate systems and distances in crack surfaces

In this section, coordinate systems and distances in explicitly defined crack surface meshes Γ_h are discussed which are used in Sec. 5 to define stresses and loadings on surfaces. Coordinate systems $\boldsymbol{x}_e$ are defined in Γ_h which are extracted from coordinate systems $\boldsymbol{X}$ of the physical space, see Sec. 4.1. Distances are evaluated based on three different types of distances which are: (i) 'spatial' distances $d_{\boldsymbol{x}}$, (ii) 'geodesic' distances d_Γ, and (iii) 'virtual' distances d_v as discussed next.

Spatial distances describe the shortest distance between two points $\boldsymbol{x}_i$ and $\boldsymbol{x}_j$ on Γ_h which is easily computed based on their corresponding Cartesian coordinates with

$$d_{\boldsymbol{x}} = ||\boldsymbol{x}_i - \boldsymbol{x}_j||. \tag{4.1}$$

That is, these distances are independent of the surface curvature and geometry.

Geodesic distances are the shortest distance between two points $\boldsymbol{x}_i$ and $\boldsymbol{x}_j$ on the surface itself. That is, they strongly depend on, e.g., the crack geometry because they are evaluated along paths which are on the surface. In general, $d_{\boldsymbol{x}}(\boldsymbol{x}_i, \boldsymbol{x}_j)$ is already for planar surfaces smaller than $d_\Gamma(\boldsymbol{x}_i, \boldsymbol{x}_j)$ due to the surface dependency, see Fig. 4.1. These distances are discussed in more detail in Secs. 4.2 and 4.3. There, they are used to evaluate distances between a point $\boldsymbol{x}_i \in \Gamma_h$ and the crack-front $\partial\Gamma_h$.

Virtual distances d_v describe the distance between a point $\boldsymbol{x}_i$ to either a source point $\boldsymbol{x}_s$ or to the crack-front $\partial\Gamma_h$. They are introduced in Sec. 4.4 based on the Laplace-Beltrami operator [61, 138].

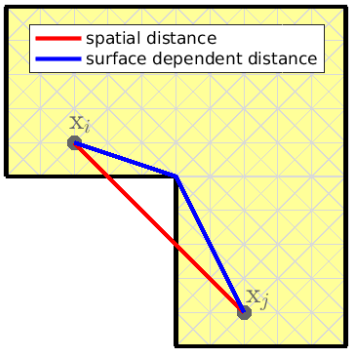

Figure 4.1: Spatial and geodesic distances on a planar crack surface.

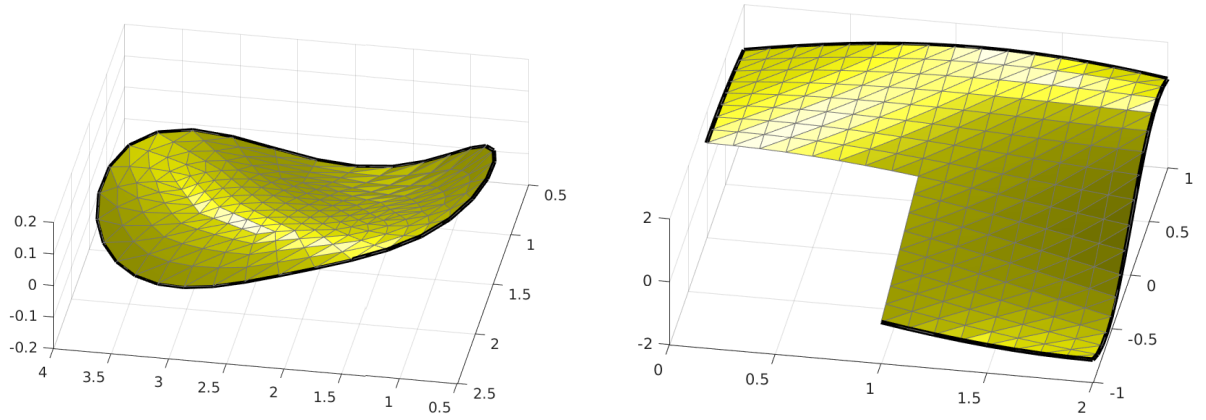

(a) (b)

Figure 4.2: Three-dimensional embedded crack geometries with a (a) closed crack-front and (b) an open crack-front.

The introduced coordinate systems and distances are illustrated exemplarily for two crack geometries, see Fig. 4.2, which not only differ geometrically but also in the fact that different parts of the crack-fronts are *active*. Fig. 4.2(a) shows a crack surface where the entire boundary is an *active* crack-front. Fig. 4.2(b) illustrates a crack geometry where only a part of the surface boundary is active because the other part coincides, e.g., with the boundary of the domain.

4.1 Euclidean coordinates

A very simple coordinate system $\boldsymbol{x}_e$ on the surface Γ_h can be extracted from coordinate systems $\boldsymbol{X}$ which are defined in the physical space of the domain, such as, Cartesian coordinates, polar coordinates, cylindrical or spherical coordinates with

$$\boldsymbol{x}_e = \boldsymbol{X}, \quad \forall \boldsymbol{X} \in \Gamma_h. \tag{4.2}$$

An example based on the Cartesian coordinate system is seen in Fig. 4.3 for the crack geometry shown in Fig. 4.2(a). There, the three coordinate components x_e, y_e and z_e of the coordinate system $\boldsymbol{x}_e$ are represented in color. It is noted that there is a wide range of other coordinate systems which can be defined on Γ_h, e.g., curvilinear coordinates which are popular in shell theory [14, 23, 29]. However, they are not in the focus of this contribution, wherefore they are not discussed in more detail and interested readers are referred to the text books [44, 189].

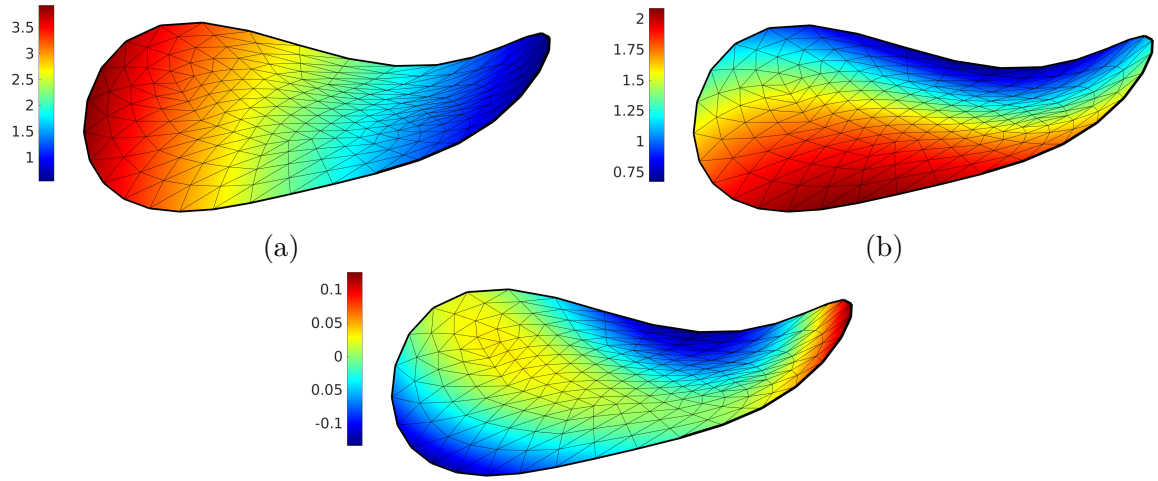

Figure 4.3: Euclidean coordinate components (a) x_e, (b) y_e, and (c) z_e extracted from the Cartesian coordinate system.

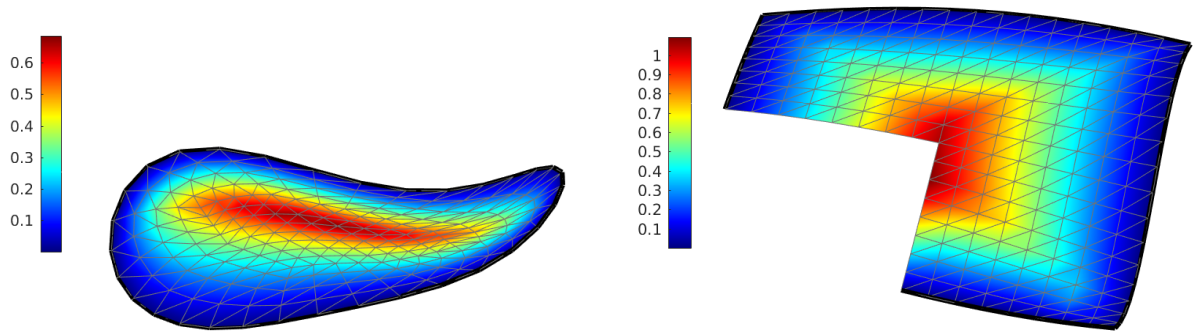

Figure 4.4: Spatial distances to (a) a closed crack-front and (b) an open crack-front.

4.2 Spatial distances to the crack-front

In this section, spatial distances are used to describe the shortest *spatial* distance between a point $\boldsymbol{x}_i \in \Gamma_h$ and the crack-front $\partial\Gamma_h$. That is, the nearest point $\boldsymbol{x}_j$ of the crack-front to $\boldsymbol{x}_i$ is sought which is either within a crack-front segment or a crack-front node. The computation of these distances was already discussed in Sec. 3 and is equivalent to computing the level-set function $\phi_2(\boldsymbol{x})$. The obtained distances are shown in Fig. 4.4 for the two crack geometries defined in Fig. 4.2.

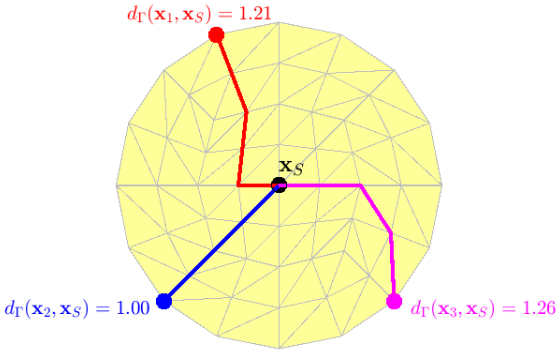

Figure 4.5: Issue of the computed geodesic distances due to the mesh dependency of the Dijkstra algorithm.

4.3 Geodesic distances to the crack-front

Next, we are interested in computing the shortest *geodesic* distance between a point $\boldsymbol{x}_i \in \Gamma_h$ and the crack-front. That is, the length of some path on the surface is of interest. The computation of these distances is more complex than the spatial distances because they are evaluated along paths which are on the surface mesh. A very fast and robust procedure is based on the 'Dijkstra algorithm' [52] which finds the shortest path between two points along element edges which renders the algorithm strictly mesh dependent. The influence of this dependency is illustrated in Fig. 4.5 where the computed geodesic distances between three points and a point $\boldsymbol{x}_S$ are shown with their corresponding paths. These points are arranged so that the exact distance of each point is given with $d(\boldsymbol{x}_i, \boldsymbol{x}_S) = 1.00$. It can be seen that the obtained distances $d(\boldsymbol{x}_i, \boldsymbol{x}_S)$ vary strongly between these points due to the mesh dependency of the procedure. Many research activities have been invested in improving the original Dijkstra algorithm, see, e.g., [32, 102, 114, 126, 183]. Geodesic distances and their corresponding paths are not the focus of this thesis, wherefore they are only mentioned here for the sake of completeness and interested readers are referred to [26] which gives a good overview of different algorithms. The geodesic distances which are obtained based on the Dijkstra algorithm are shown in Fig. 4.6 for the two crack geometries of Fig. 4.2.

4.4 Virtual distances based on Laplace-Beltrami operator and point sources

This section deals with distances between a point $\boldsymbol{x}_i \in \Gamma_h$ and the crack-front $\partial\Gamma_h$ or between the point $\boldsymbol{x}_i$ and a point source $\boldsymbol{x}_S$ along streamlines which are obtained from solving a Laplace-Beltrami problem. These selected paths are used due to the physical

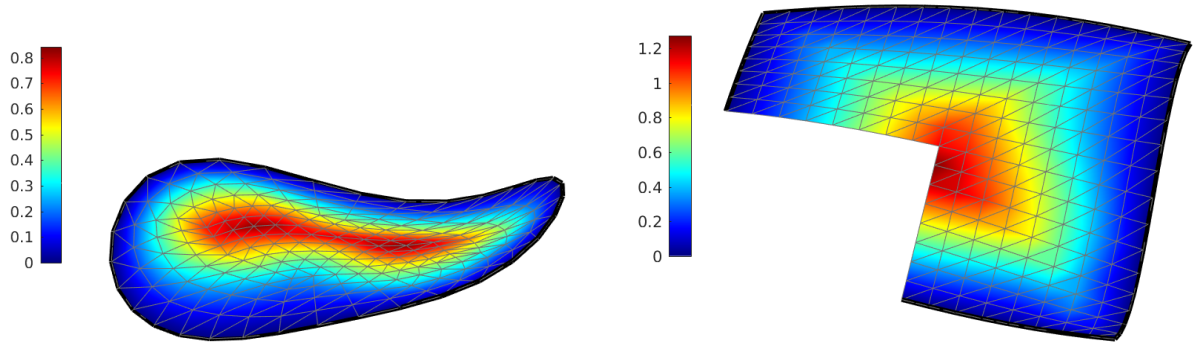

(a) (b)

Figure 4.6: Geodesic distances to (a) a closed crack-front and (b) an open crack-front.

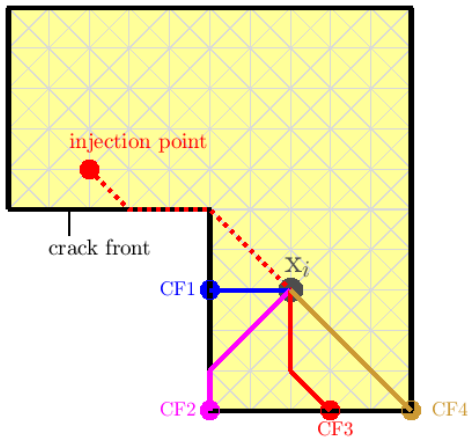

Figure 4.7: Issue of the Dijkstra algorithm in the context of HF.

meaning of the Poisson problem because the obtained distances are used later in the context of HF, see Sec. 5.3. There, the fluid pressure exerted by the fracking fluid is related to a fluid flow within a fracture which, in turn, is closely related to the flow described by the Poisson problem. Regarding to the intended use of these virtual distances, many assumptions and discussions of this section are related to HF. In this context, the point source $\boldsymbol{x}_S$ represents the well and is further called 'injection point'.

The evaluation of virtual distances based on other approaches, e.g., the Dijkstra algorithm has the disadvantage that the shortest distances are only computed between two points which have to be explicitly defined. That is, the distance between a point $\boldsymbol{x}_i$ and the crack-front $\partial\Gamma_h$ is not unique but depends on the selected node on the crack-front, see Fig. 4.7. Another issue is that paths are constructed without a physical meaning, wherefore they could partially coincide with the crack-front which is illustrated in Fig. 4.7 by the dashed line. In contrast, the proposed procedure works for any crack geometries in the same way and physically meaningful paths are provided automatically without any

further assumptions, see Fig. 4.10.

4.4.1 Laplace-Beltrami operator

A generalization of the *classical* Laplace operator Δ from flat spaces to curved manifolds is known as Laplace-Beltrami operator Δ_Γ [61, 138]. For solving models involving the Laplace Beltrami operator, a straightforward extension of the finite element approach may be used based on tangential differential calculus which was first done by Dziuk [60]. The strong form of the Poisson problem on curved surfaces is [101]

$$-\Delta_\Gamma u = f \quad \text{in } \Gamma, \tag{4.3}$$

$$u = u_D \quad \text{on } \partial\Gamma_D, \tag{4.4}$$

$$\boldsymbol{n}_{\partial\Gamma} \cdot \nabla_\Gamma u = t_N \quad \text{on } \partial\Gamma_N. \tag{4.5}$$

Herein, f is a source function, $\partial\Gamma_D$ the Dirichlet boundary, $\partial\Gamma_N$ the Neumann boundary, and $\boldsymbol{n}_{\partial\Gamma}$ the unit co-normal vector on the boundary in the tangent plane of the manifold. The surface gradient ∇_Γ of a scalar function u is defined as

$$\nabla_\Gamma u(\boldsymbol{x}) = \mathbf{P}(\boldsymbol{x}) \cdot \nabla_{\boldsymbol{x}} u(\boldsymbol{x}), \qquad \forall \boldsymbol{x} \in \Gamma, \tag{4.6}$$

based on the tangential projector

$$\mathbf{P}(\boldsymbol{x}) = [\mathbf{I} - \boldsymbol{n}_\Gamma(\boldsymbol{x}) \otimes \boldsymbol{n}_\Gamma(\boldsymbol{x})] = \left[\mathbf{I} - \boldsymbol{n}_\Gamma \cdot \boldsymbol{n}_\Gamma^T\right]. \tag{4.7}$$

$\mathbf{I}$ is the identity matrix, $\boldsymbol{n}_\Gamma$ a unit normal vector on the manifold, and $\nabla_{\boldsymbol{x}} u(\boldsymbol{x})$ is the 'classical' gradient of the function u in the physical space. That is, Eq. 4.6 requires the partial derivatives of $u(\boldsymbol{x})$ in global coordinates. For the case of a parametrised representation of $u(\boldsymbol{x}(\boldsymbol{\xi}))$, global derivatives are not directly available in contrast to the local ones, wherefore Eq. 4.6 can not be used in the present form. The surface gradient can be expressed in terms of partial derivatives in local coordinates based on the Jacobi matrix $\mathbf{J} = {}^{\partial \boldsymbol{x}}/_{\partial \boldsymbol{\xi}}$ with

$$\nabla_\Gamma u(\boldsymbol{x}) = \mathbf{J} \cdot \left(\mathbf{J}^T \mathbf{J}\right)^{-1} \cdot \nabla_{\boldsymbol{\xi}} u(\boldsymbol{\xi}) = \mathbf{J} \cdot \mathbf{G}^{-1} \cdot \nabla_{\boldsymbol{\xi}} u(\boldsymbol{\xi}), \tag{4.8}$$

where $\mathbf{G}$ is the metric tensor (first fundamental form).

As previously mentioned, the solution of Eq. 4.3 is used to evaluate distances along its corresponding streamlines on an explicit surface mesh, therefore, the problem is solved on a discrete manifold Γ_h described with two-dimensional elements in three dimensions. For solving the problem, the standard surface FEM as described in [45, 61] is used which

leads to the following problem statement. For u^h and w^h being composed by finite element functions living on the discrete manifold Γ_h, find the one function u^h such that the following discrete weak form is fulfilled for all test functions w^h:

$$\int_{\Gamma_h} \nabla_{\Gamma_h} w^h \cdot \nabla_{\Gamma_h} u^h dA = \int_{\Gamma_h} w^h \cdot f dA + \int_{\partial\Gamma_N} w^h \cdot t_N dS. \tag{4.9}$$

For the sake of clarity, the index h of the discrete manifold Γ_h is not written anymore within this chapter, however, it is noted that all further discussions are based on a discrete manifold Γ_h which, in this context, coincides with the explicitly defined crack geometry.

For a two-dimensional manifold which is embedded in three dimensions the global surface derivatives of the shape functions $^{\partial N_\Gamma}/_{\partial \boldsymbol{x}}$ which are required to solve Eq. 4.9 can be calculated based on Eq. 4.8 in the following form

$$N_{\Gamma,\boldsymbol{x}} = \mathbf{J} \cdot \mathbf{G}^{-1} \cdot N_{\Gamma,\boldsymbol{\xi}} \tag{4.10}$$

$$\begin{pmatrix} \frac{\partial N_\Gamma}{\partial x} \\ \frac{\partial N_\Gamma}{\partial y} \\ \frac{\partial N_\Gamma}{\partial z} \end{pmatrix} = \begin{bmatrix} \frac{\partial x}{\partial \xi} & \frac{\partial x}{\partial \eta} \\ \frac{\partial y}{\partial \xi} & \frac{\partial y}{\partial \eta} \\ \frac{\partial z}{\partial \xi} & \frac{\partial z}{\partial \eta} \end{bmatrix} \cdot \left(\begin{bmatrix} \frac{\partial x}{\partial \xi} & \frac{\partial y}{\partial \xi} & \frac{\partial z}{\partial \xi} \\ \frac{\partial x}{\partial \eta} & \frac{\partial y}{\partial \eta} & \frac{\partial z}{\partial \eta} \end{bmatrix} \begin{bmatrix} \frac{\partial x}{\partial \xi} & \frac{\partial x}{\partial \eta} \\ \frac{\partial y}{\partial \xi} & \frac{\partial y}{\partial \eta} \\ \frac{\partial z}{\partial \xi} & \frac{\partial z}{\partial \eta} \end{bmatrix} \right)^{-1} \cdot \begin{pmatrix} \frac{\partial N_\Gamma}{\partial \xi} \\ \frac{\partial N_\Gamma}{\partial \eta} \end{pmatrix}. \tag{4.11}$$

It is noted that for the numerical evaluation of the integrals in Eq. 4.9 over the manifold, the integration weights in the reference element are modified by Gram's determinant,

$$\omega_i^{\boldsymbol{x}} = \omega_i^{\boldsymbol{\xi}} \cdot \sqrt{\det(\mathbf{J}^T \mathbf{J})} = \omega_i^{\boldsymbol{\xi}} \cdot \sqrt{\det(\mathbf{G})}. \tag{4.12}$$

That is, the integration weight $w_i^{\boldsymbol{x}}$ within the physical space is the integration weight within the reference element $w_i^{\boldsymbol{\xi}}$ scaled with the square-root of the determinant of the first fundamental form $\mathbf{G}$.

4.4.1.1 Boundary conditions for the evaluation of virtual distances

The Laplace-Beltrami problem is a basis for a physical interpretation of a fluid flow within a fracture which is induced by pumping a fracking fluid through a well into the fracture. For this problem, u is prescribed with 1 on $\partial\Gamma_D = \partial\Gamma$ and with 0 at the injection point $\boldsymbol{x}_S$. That is, no source function f and Neumann boundary $\partial\Gamma_N$ are required. To keep the algorithm simple, it is recommended to describe the discrete manifold such that the location of the injection point $\boldsymbol{x}_S$ is already considered by placing a node at this position.

4.4.2 Computation of streamlines

In this section, the evaluation of the streamlines on Γ_h is discussed based on the obtained solution of Eq. 4.9 with the applied boundary conditions of Sec. 4.4.1.1. In this thesis, the explicit crack description is restricted to crack representations based on simplex elements which simplifies the determination of streamlines on Γ_h because the gradients are constant within a surface element. This restriction also simplifies the evaluation of level-set functions which are based on distance functions, see Sec. 3.1.3. The proposed procedure could easily be extended to crack representations with higher-order quadrilaterals or triangles elements, however, such elements increase the computational effort dramatically as the gradient is no longer constant within an element, wherefore the resulting streamlines are curved in general. The general procedure to determine the streamlines $s(\boldsymbol{x}_0, \boldsymbol{x}_S)$ and $s(\boldsymbol{x}_0, \partial\Gamma_h)$ of a point $\boldsymbol{x}_0$ to the injection point $\boldsymbol{x}_S$ and to the crack-front $\partial\Gamma_h$, respectively, is discussed next.

1. The Laplace-Beltrami problem is solved on the explicitly defined crack surface mesh with the applied boundary conditions of Sec. 4.4.1.1. Hence, the scalar function $u(\boldsymbol{x})$ on the crack surface is computed.

2. Some point $\boldsymbol{x}_0 \in \Gamma_h$ is chosen for which the streamlines shall be computed. It is noted that the proposed procedure demands that $\boldsymbol{x}_0$ is located within an element. A special treatment is introduced in Sec. 4.4.2.3 which deals with starting points which are located at element nodes or edges.

3. The gradient of this point is evaluated based on the global derivatives of the element shape functions and their corresponding nodal values with

$$[\nabla_\Gamma u(\boldsymbol{x}_0)]_i^\star = \sum_{j=1}^{n_e} \nabla_\Gamma N_j(\boldsymbol{x}_0) \cdot u_j. \tag{4.13}$$

   Herein, the lower index i identifies the gradient of the corresponding element i. If two or more indices are used, e.g., $(i;j)$ it indicates that the gradient is averaged over the elements i and j, see Eq. 4.14. The * represents that the gradient has no unit length in general. Gradients with unit length are easily provided by Eq. 4.14. It is noted that simplex elements lead to constant gradients within an element, wherefore all gradients $[\nabla_\Gamma u]_k^\star$ must be calculated only once per element which decreases the computational effort of the procedure.

4. Start from the point $\boldsymbol{x}_0$ and follow the gradient $[\nabla_\Gamma u(\boldsymbol{x}_0)]_i$ until an element edge is reached. In this thesis, the j-th intersection of the streamline with an element edge is identified by its corresponding point $\boldsymbol{x}_j^\star$.

5. The gradient at the intersection $\boldsymbol{x}_j^\star$ is discontinuous because the element edge belongs to two simplex elements i and j. Therefore, it is suggested to determine an averaged gradient $[\nabla_\Gamma u]_{i;j}$ as follows

$$[\nabla_\Gamma u]_{i;j} = \frac{[\nabla_\Gamma u]^\star_{i;j}}{||\,[\nabla_\Gamma u]^\star_{i;j}\,||} \quad \text{with} \quad [\nabla_\Gamma u]^\star_{i;j} = \frac{\sum_{k=i,j} A_k \cdot [\nabla_\Gamma u]_k}{\sum_k A_k}, \tag{4.14}$$

   through the corresponding element areas A_k and their gradients $[\nabla_\Gamma u]_k$.

6. Based on the averaged gradient, the next intersection $\boldsymbol{x}^\star_{j+1}$ of the streamline with an element edge is determined which is discussed in more detail in Sec. 4.4.2.1.

7. Repeat the last two steps until the injection point or the crack-front is reached setting $\boldsymbol{x}^\star_j$ to $\boldsymbol{x}^\star_{j+1}$.

In this thesis, elements which consist of the injection point $\boldsymbol{x}_S$ or the crack-front $\partial\Gamma_h$ are called 'injection point elements' or 'crack-front elements' and are specially treated, see Sec. 4.4.2.2, which decreases the numerical effort. The major steps of the proposed procedure are summarized in Fig. 4.8. It is noted that the proposed procedure describes the streamline $s(\boldsymbol{x}_0, \partial\Gamma_h)$ between $\boldsymbol{x}_0$ and the crack-front $\partial\Gamma_h$. The streamline $s(\boldsymbol{x}_0, \boldsymbol{x}_S)$ between $\boldsymbol{x}_0$ and the injection point $\boldsymbol{x}_S$ can be computed with the same procedure by using the *negative* gradient pointing in the opposite direction.

4.4.2.1 Evaluation of streamline/element edge intersections

The evaluation of streamline intersections with element edges is based on the determination of line-plane intersections. Such a procedure is required due to the fact that the averaged gradients $[\nabla_\Gamma u]_{i;j}$ of two elements i and j are usually not in the plane of the discrete manifold Γ_h. That is, in addition to the averaged gradients it is also necessary to provide averaged normal vectors $\boldsymbol{n}_{i;j}$ at $\boldsymbol{x}^\star_j$ which together with $[\nabla_\Gamma u]_{i;j}$ define the required plane, see Fig. 4.9. These special normal vectors are computed equivalently to the averaged gradients with the corresponding element areas. The line-plane intersection can be formulated within the concrete application as

$$\boldsymbol{x}^\star_j + r \cdot \boldsymbol{n}_{i;j} + s \cdot [\nabla_\Gamma u]_{i;j} = \boldsymbol{x}_k + t \cdot \boldsymbol{q}_k. \tag{4.15}$$

Herein, $\boldsymbol{x}_k$ are the Cartesian coordinates of a corresponding element node, $\boldsymbol{q}_k$ the direction of the corresponding element edge, and $\{r, s, t\}$ represent the unknown scaling values which are required to fulfill Eq. 4.15. The requirements of the unknowns are

$$0 - \varepsilon_{\text{tol}} \leq t \leq 1 + \varepsilon_{\text{tol}}, \tag{4.16}$$

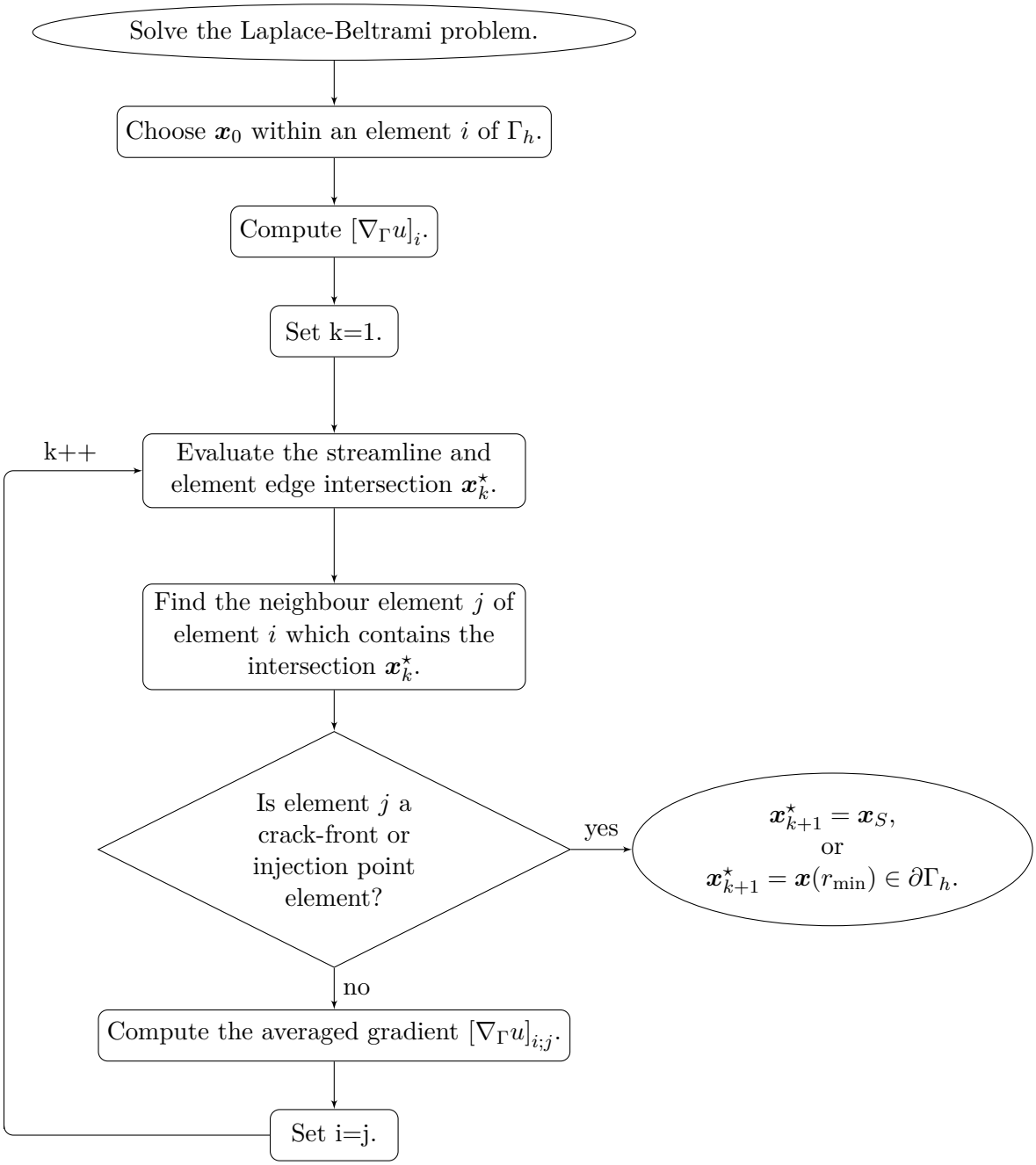

Figure 4.8: Algorithm of the streamline procedure.

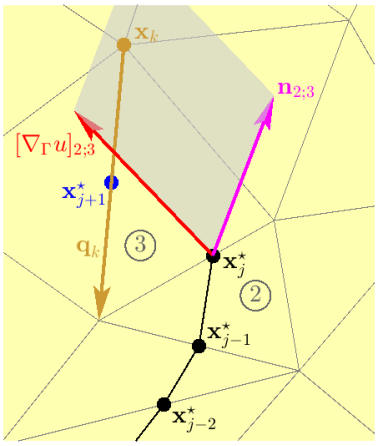

Figure 4.9: Illustration of streamline search.

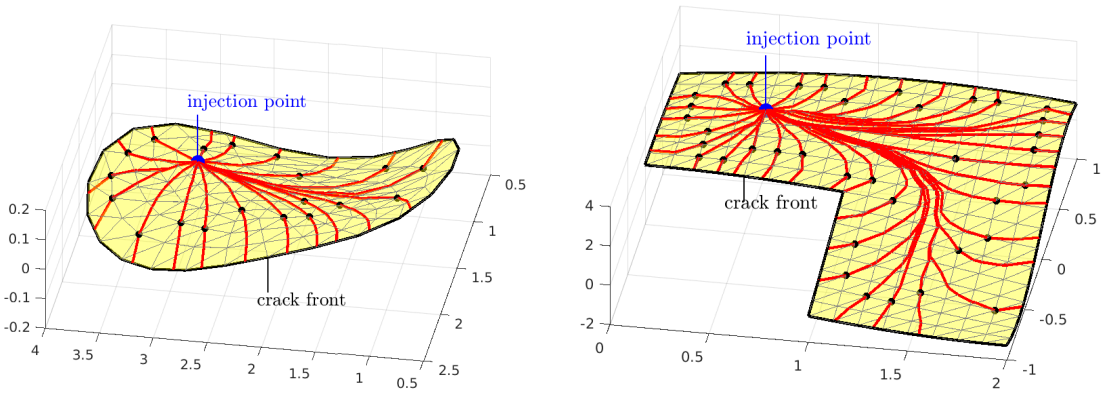

(a) (b)

Figure 4.10: Resulting streamlines on two different crack geometries with an arbitrarily arranged injection point.

and

$$s > -\varepsilon_{\text{tol}} \cdot l_{\text{Elem}} \tag{4.17}$$

which ensure that the determined intersection is in direction of the gradient and on an element edge. Herein, ε_{tol} is a globally defined tolerance and l_{Elem} characterizes the size of the current element. These tolerances are required for a robust calculation of intersections close to element nodes which is discussed in the next paragraphs. It will also be discussed where the new intersections can be and what special issues are associated with them.

Evaluation of the next intersection Based on the presented procedure, there are two possibilities where the new intersection $\boldsymbol{x}^\star_{j+1}$ can be found: (*i*) In the neighbour element j of element i which is the usual case, see Fig. 4.11(a), or (*ii*) in the same element where the intersections $\boldsymbol{x}^\star_{j-1}$ and $\boldsymbol{x}^\star_j$ were, see Fig. 4.11(b). In most cases, the intersection will be in

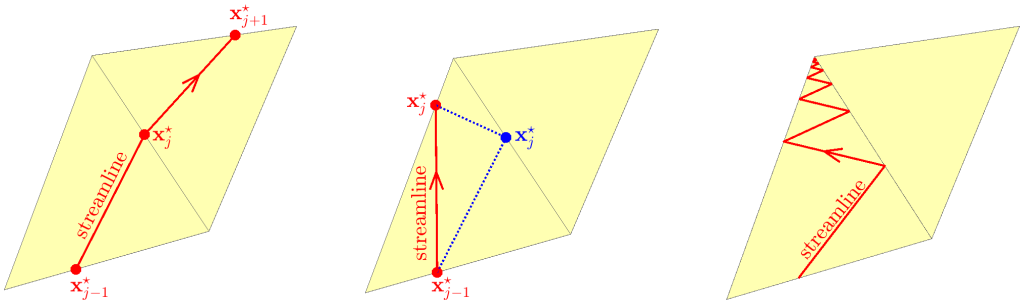

(a) (b) (c)

Figure 4.11: Intersection in (a) neighbour element or (b) in same element. (c) Iterations within one element.

the neighbour element, however, due to the averaging, the gradient may point back to the current element. That would lead to an unphysical streamline, wherefore a modification of the standard procedure is suggested. If the new intersection $\boldsymbol{x}^\star_{j+1}$ is within an element where also the two previous intersections $\boldsymbol{x}^\star_{j-1}$ and $\boldsymbol{x}^\star_j$ are, then the current intersection $\boldsymbol{x}^\star_j$ is removed and the streamline is defined as a connection of the intersections $\boldsymbol{x}^\star_{j-1}$ and $\boldsymbol{x}^\star_{j+1}$. After that $\boldsymbol{x}^\star_{j+1}$ is set to $\boldsymbol{x}^\star_j$ and the next intersection is computed. This procedure is repeated until an intersection is found in a neighbour element. Usually, this happens already after the first update, however, in extreme cases where the gradients change strongly between neighbouring elements it could happen that the method converges to an element node, see Fig. 4.11(c). In such cases, the introduced tolerances of Eqs. 4.16 and 4.17 ensure that the proposed edge-based method does not end at the element node which is discussed in more detail next.

Streamline converges to an element node The tolerances provide a robust procedure based on the fact that the algorithm firstly detects an intersection in the neighbour element and only if there is no intersection it goes back to the previous element. Fig. 4.12(a) shows the effect of the tolerance used in Eq. 4.16 which is discussed next based on the illustrated example: the intersection is found on the element edge of element 1 and 2 due to the averaged gradient $[\nabla_\Gamma u]_{2;3}$. At this intersection the averaged gradient $[\nabla_\Gamma u]_{1;2}$ would point back to the previous element which is illustrated by the red dashed line. That is, without a tolerance the procedure would only find intersections along the two element edges of element 2, wherefore the streamline would converge and end at the corner of the corresponding element. The tolerance applied in Eq. 4.16 avoids such behaviour by allowing intersections which are infinitesimally close on the straight extension of the element edge. Such an intersection is represented respectively in Fig. 4.12(a) as a black diamond. Due to the fact that the procedure is not able to deal with points outside

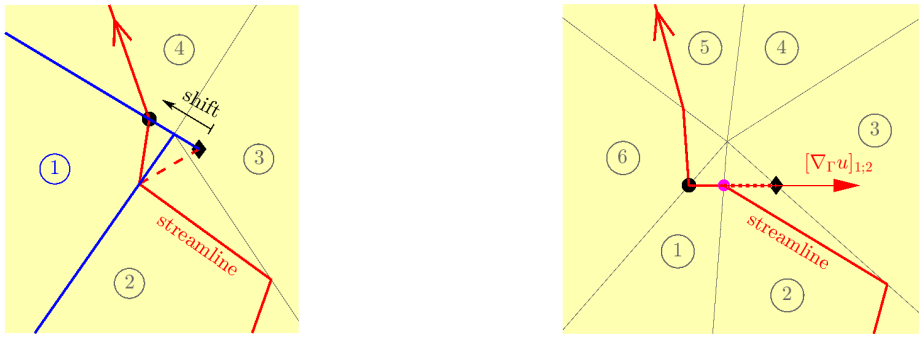

(a) (b)

Figure 4.12: Graphical interpretation of the tolerances for an (a) element edge, see Eq. 4.16, and (b) a negative gradient, see Eq. 4.17.

the observed element or with points which coincide exactly with element nodes these 'special' intersections are shifted back to the observed element. This shift arranges the new intersection on the corresponding element edge at a small distance away from the node, see Fig. 4.12(a). The second tolerance in Eq. 4.17 is used for the same reason as the previously discussed tolerance. It allows an intersection in the neighbour element which may be found with the negative gradient under the condition that the distance between the intersections $\boldsymbol{x}_j^\star$ and $\boldsymbol{x}_{j+1}^\star$ is sufficiently small. A relative definition of this tolerance is required to ensure that the element size and the global defined tolerance are not in the same range. Therefore, the global defined tolerance ε_{tol} is multiplied with the corresponding element length. The effect of the second tolerance is illustrated in Fig. 4.12(b) where the red line represents the achieved streamline and the dashed line represents the direction of the original gradient. Dependent on the mesh and the arrangement of the elements both tolerances may be relevant. It is noted that this special treatment is only needed if intersections are very close to element nodes.

4.4.2.2 Intersections in the vicinity of the injection point or the crack-front

Elements which consist of crack-front nodes ('crack-front elements') or the injection point ('injection point elements') are treated specially which increases the numerical robustness and avoids undesired features within these elements. Such modifications are required, for example, within two neighbouring crack-front elements i and j where $[\nabla_\Gamma u]_{i;j} = \mathbf{0}$ due to the applied boundary conditions of Sec. 4.4.1.1. The proposed treatment of injection point elements only reduces the numerical effort due to the avoidance of required iterations within these elements but is not necessary for increasing the robustness of the algorithm.

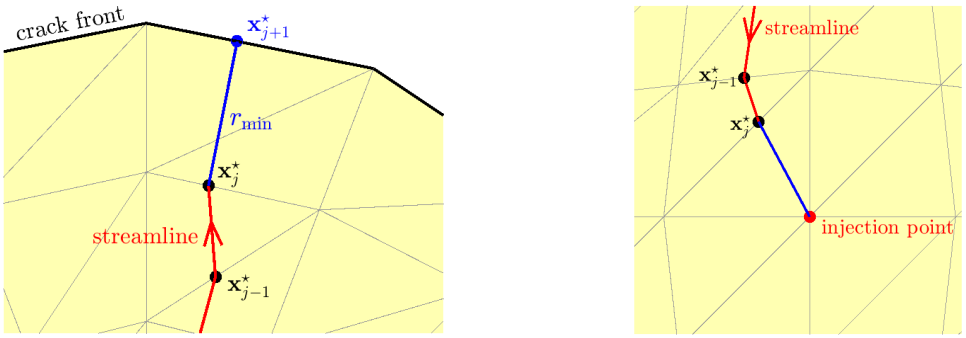

(a) (b)

Figure 4.13: Special treatment for (a) crack-front elements and (b) elements which consist of the injection node.

Injection point elements When an injection point element is reached, it is proposed to define the streamline as the direct connection of the last intersection and the injection point $\boldsymbol{x}_S$, see Fig. 4.13(b). This procedure is quite simple and avoids iterations which are usually required to reach the injection point within these elements. Similar to the definition of the crack-tip enriched nodes of Sec. 3.1.3 and their corresponding crack-tip enriched elements, there are two possibilities to define the injection point elements. These elements may either be those which (*i*) contain the injection point $\boldsymbol{x}_S$ or (*ii*) those where the minimum distance of at least one element node to the injection point is smaller than a pre-defined distance r_{IPE}. The first definition leads to almost the same streamline as the general procedure, however, it is computationally more expensive than the second definition because more intersections have to be found numerically until an injection point element is reached. The second definition decreases the number of required intersections, however, significant differences of the resulting streamline compared to the alternative procedure can occur. This follows, for example, from the fact that a direct connection of the last intersection and the injection point is not bounded on the crack surface, wherefore the resulting streamline is usually not on the manifold within this area. Therefore, the size of r_{IPE} should be chosen based on expected solution properties, element sizes, and the curvature of the surface mesh. Therefore, it is proposed to keep r_{IPE} small enough to obtain sufficiently accurate results.

Crack-front elements As mentioned above, a special treatment of the crack-front elements is essential to provide a robust procedure. If a crack-front element is reached the streamline is defined by the direct connection of the last intersection and the nearest corresponding point of the crack-front. This computation is based on the algorithm which is used to evaluate the second level-set function of Sec. 3.1.3, wherefore no further

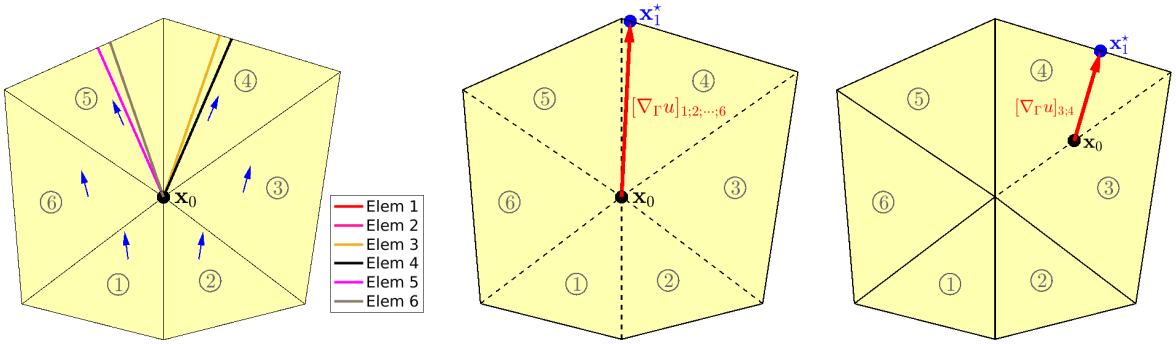

(a) (b) (c)

Figure 4.14: Resulting streamlines (a) in dependency of the corresponding starting elements. Special treatment of the streamline detection when the starting point is (b) an element node, or (c) is located along an element edge.

implementations are required. It is noted that this procedure does not guarantee that the resulting streamline is on the manifold, however, it is stable and can also deal with intersections in the vicinity of the crack-front where the averaged gradient $[\nabla_\Gamma u]_{i;j}$ is zero.

4.4.2.3 Starting point is an element node or is located along an element edge

As previously mentioned, the starting point $\boldsymbol{x}_0$ has to be within an element. That is, if $\boldsymbol{x}_0$ is chosen as an element node, this point has to be shifted within an element i so that the first streamline and element edge intersection is at an element edge of element i. In general, the resulting streamlines depend on the shifting, in particular, into which element the starting point $\boldsymbol{x}_0$ is moved, see Fig. 4.14(a). There, the resulting streamlines due to different elements which are used as starting elements are illustrated. The gradients of the individual elements are illustrated as blue arrows. To overcome this dependency, a special treatment is introduced for starting points which are located at element nodes or along element edges. This treatment is frequently used in Sec. 4.4.3 where streamlines are evaluated for points which are located at the element nodes of the surface mesh. These streamlines are used for the computation of virtual distances at these nodes.

If the starting point $\boldsymbol{x}_0$ is an element node, an averaged gradient $[\nabla_\Gamma u]_{i;j;\cdots;k}$ and averaged normal vector $\boldsymbol{n}_{i;j;\cdots;k}$ are determined based on Eq. 4.14 and all elements $\{i;j;\cdots;k\}$ which consist of the corresponding node. Then, based on Eq. 4.15 the first intersection $\boldsymbol{x}_1^\star$ is determined at an element edge which does not consist of $\boldsymbol{x}_0$, see Fig. 4.14(b). If $\boldsymbol{x}_0$ is located along an element edge, see Fig. 4.14(c), the general procedure can be used by replacing the first gradient $[\nabla_\Gamma u]_i$ through the averaged gradient $[\nabla_\Gamma u]_{i;j}$ of the corresponding elements.

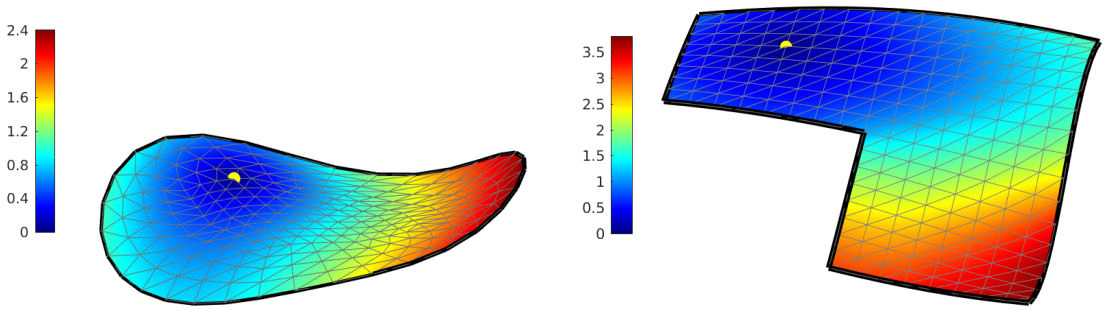

(a) (b)

Figure 4.15: Absolute virtual distances on two different crack geometries with an arbitrarily arranged injection point (yellow dot).

4.4.3 Absolute and dimensionless virtual distances

Based on the streamlines $s(\boldsymbol{x}_0, \boldsymbol{x}_S)$ and $s(\boldsymbol{x}_0, \partial\Gamma_h)$, the corresponding absolute virtual distances $d_v(\boldsymbol{x}_0, \boldsymbol{x}_S)$ and $d_v(\boldsymbol{x}_0, \partial\Gamma_h)$ are computed with

$$d_v(\boldsymbol{x}_0, j) = \int_\Gamma s(\boldsymbol{x}_0, j) d_\Gamma \quad \text{with } j = \{\boldsymbol{x}_S, \partial\Gamma_h\}. \tag{4.18}$$

In Fig. 4.15, the absolute virtual distances $d_v(\boldsymbol{x}_0, \boldsymbol{x}_S)$ are illustrated for the two crack geometries shown in Fig. 4.2 where also the injection point $\boldsymbol{x}_S$ is arranged arbitrarily. It is noted that the virtual distances are used in the context of HF, wherefore the entire boundary of the crack geometry shown in Fig. 4.2(b) is set to an active crack-front here.

These absolute virtual distances can also be used to describe the dimensionless virtual distance $\tilde{d}_v(\boldsymbol{x}_0)$ of a point $\boldsymbol{x}_0$ between the injection point $\boldsymbol{x}_S$ and the crack-front $\partial\Gamma_h$. Minimum requirements on $\tilde{d}_v(\boldsymbol{x}_0)$ are

$$\tilde{d}_v(\boldsymbol{x}_0) = \begin{cases} 0 & \text{if: } \boldsymbol{x}_0 = \boldsymbol{x}_S \\ 1 & \text{if: } \boldsymbol{x}_0 \in \partial\Gamma_h \\ 0 \leq \tilde{d}_v(\boldsymbol{x}_0) \leq 1 & \text{if: } \boldsymbol{x}_0 \in \Gamma_h. \end{cases} \tag{4.19}$$

It is easily shown that the ratio of the absolute virtual distances,

$$\tilde{d}_v(\boldsymbol{x}_0) = \frac{d_v(\boldsymbol{x}_0, \boldsymbol{x}_S)}{d_v(\boldsymbol{x}_0, \boldsymbol{x}_S) + d_v(\boldsymbol{x}_0, \partial\Gamma_h)} \qquad \forall \boldsymbol{x}_0 \in \Gamma_h \tag{4.20}$$

fulfills these conditions in general. These distances are illustrated in color in Fig. 4.16 based on the same crack configurations as for the absolute virtual distances. The accuracy of the resulting dimensionless virtual distances is investigated based on a parabolic crack

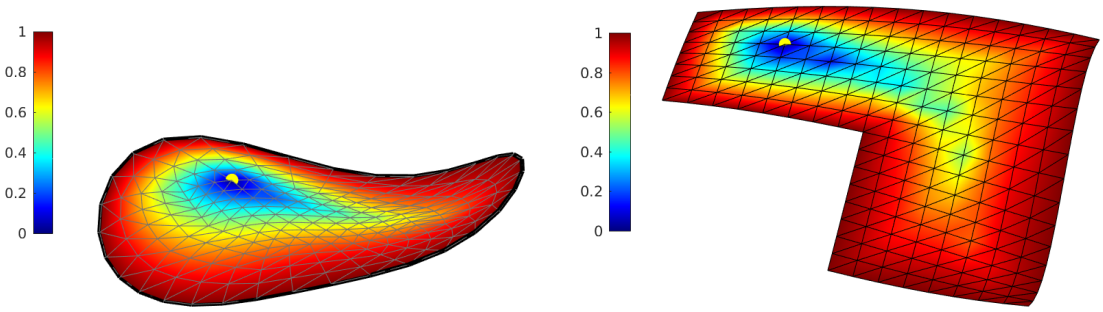

(a) (b)

Figure 4.16: Dimensionless virtual distances on two different crack geometries with an arbitrarily arranged injection point (yellow dot).

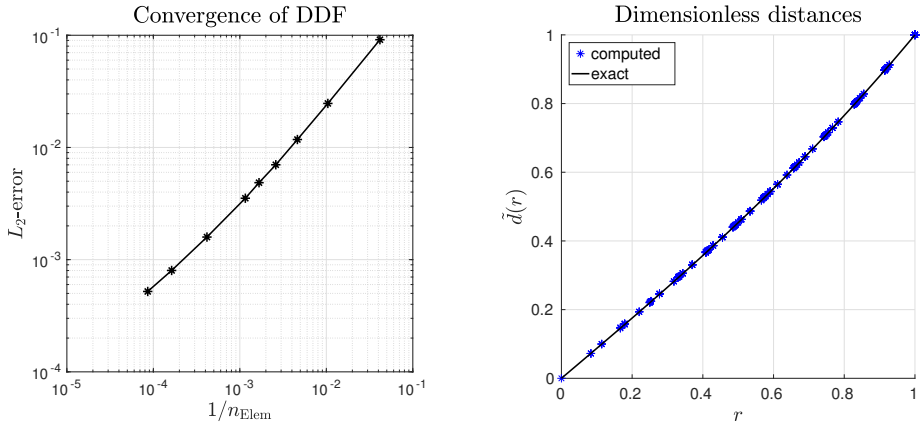

(a) (b)

Figure 4.17: Dimensionless distances on a parabolic-shaped manifold. (a) Convergence and (b) comparison of computed and exact dimensionless distances.

surface with $r(x,y) = \sqrt{x^2+y^2}$ and $z = 0.5 \cdot r^2(x,y)$ which is bounded with $0 \leq r \leq r_{\max}$. The injection point $\boldsymbol{x}_S$ is arranged in the center of the surface mesh ($\boldsymbol{x}_S = [0,0,0]^T$) and $r_{\max}$ is set to 1. For this configuration the analytical dimensionless distance $\tilde{d}_v^{\text{ref}}(r_i)$ of a point $\boldsymbol{x}_i$ is given with

$$\tilde{d}_v^{\text{ref}}(r_i) = \frac{\int_0^{r_i} \sqrt{1+r^2}dr}{\int_0^{r_{\max}} \sqrt{1+r^2}dr}. \tag{4.21}$$

The L_2-error of the proposed procedure is illustrated in Fig. 4.17(a) for different mesh refinements and the computed dimensionless distances are shown in Fig. 4.17(b) based on a surface mesh which is described with 864 simplex elements. As can be seen, the obtained and analytical results are in good agreement.

5 Stresses and loadings of crack surfaces

There are many applications where the crack surface is loaded, in fact, this load may be the dominant driving force for the potential propagation of the crack. Examples are: magma-driven dykes [155], the heat production from geothermal reservoirs [142], the fault reactivation in mining [24], corrosion and freezing processes in fractured structures etc. Another example is HF for reservoir stimulation where a fracking fluid is pumped into some rock formation to induce fractures and increase the permeability and, thereby, the productivity [2, 113, 141]. In this section, the definitions of stress or pressure functions on the explicit surface mesh based on the introduced coordinate systems and distances of Sec. 4 are discussed. It is noted that the explicit surface mesh can also be used in the context of the standard surface FEM [45, 61] to approximate some physical models such as, e.g., fluid models which provide pressures as part of the solution. Due to the fact that such models are not the focus of this thesis, this possibility of pressure definitions is not discussed in further details. Another focus of this section is the data transfer between an implicit and explicit crack description which is required due to the fact that these crack geometries may not coincide exactly.

5.1 Stress functions based on Euclidean coordinates

Stress functions which can be related to Euclidean coordinates are, e.g., far field tractions such as in-situ stresses. Such a stress function is discussed next in the context of the at-rest lateral earth pressure [41, 42], respectively.

For an un-cracked homogeneous soil with a unit weight γ, the stress state $\boldsymbol{\sigma}(\boldsymbol{x})$ at a point $\boldsymbol{x}$ which is located in a depth z below the earth's surface can be defined based on the 'at-rest earth pressure coefficient K_0' [41, 42, 97, 124]. This coefficient describes the ratio of the vertical normal stress σ_{zz} to the horizontal normal stresses σ_{xx} and σ_{yy}. If shear stresses are neglected, the Cauchy stress tensor $\boldsymbol{\sigma}(\boldsymbol{x})$ at the point $\boldsymbol{x}$ is defined with

$$\boldsymbol{\sigma}(\boldsymbol{x}) = \begin{bmatrix} K_0 \cdot \gamma \cdot z & 0 & 0 \\ 0 & K_0 \cdot \gamma \cdot z & 0 \\ 0 & 0 & \gamma \cdot z \end{bmatrix}. \tag{5.1}$$

That is, based on the Euclidean coordinates $\boldsymbol{x}_e$ of Sec. 4.1 which are extracted from

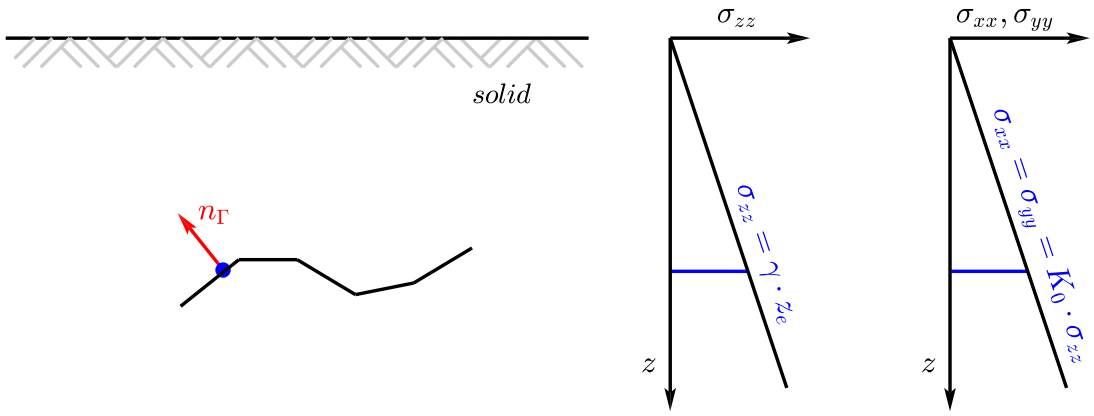

Figure 5.1: In-situ stresses on a crack path/surface based on the at-rest lateral earth pressure.

the Cartesian coordinate system, the entire stress state $\boldsymbol{\sigma}(\boldsymbol{x}_e)$ on a closed (imaginary) crack surface is defined, see Fig. 5.1. Based on the conversion of boundary tractions into equivalent crack face tractions, see Sec. 2.2.4, the in-situ stresses can be applied through the corresponding crack surface tractions $\boldsymbol{t}_C(\boldsymbol{x}_e)$

$$\boldsymbol{t}_C(\boldsymbol{x}_e) = \boldsymbol{\sigma}(\boldsymbol{x}_e) \cdot \boldsymbol{n}_\Gamma(\boldsymbol{x}_e), \tag{5.2}$$

which are evaluated based on the corresponding normal vectors $\boldsymbol{n}_\Gamma(\boldsymbol{x}_e)$ of the crack surface Γ_h, see Fig. 5.1. The advantage of the conversion of boundary tractions into equivalent crack face tractions is that in-situ stresses can be considered without additional deformations of the domain which occur, e.g., due to applied Neumann boundary conditions. It is also noted that this conversion is not limited to any specified properties of the Cauchy stress tensor $\boldsymbol{\sigma}$, wherefore also shear stresses can be considered. That is, there are no restrictions on the geomechanical models which are used to determine the in-situ stresses.

It is also possible to define scalar pressure functions $p(\boldsymbol{x}_e)$ on Γ_h based on the Euclidean coordinates $\boldsymbol{x}_e$. An example is the hydrostatic pressure $p_w(z_e)$ exerted by the water at a point $\boldsymbol{x}(z_e)$ which is located in a water depth of z_e. With the water density ρ_w, the acceleration g due to gravity, and the pressure p_0 which acts at $z_e = 0$, the hydrostatic pressure $p_w(z_e)$ is defined based on Pascal's law with: $p_w(z_e) = \rho_w g z_e + p_0$. Pressures $p(f(\boldsymbol{x}_e))$ can also be associated with other physical fields $f(\boldsymbol{x}_e)$ which are extracted from the Euclidean coordinates such as, e.g., a temperature field $T(\boldsymbol{x})$ which is provided globally for the domain and is evaluated on the crack surface. Such models are required, e.g., for freezing processes in fractured structures and to evaluate gas pressures because the exerted loads are strongly temperature dependent.

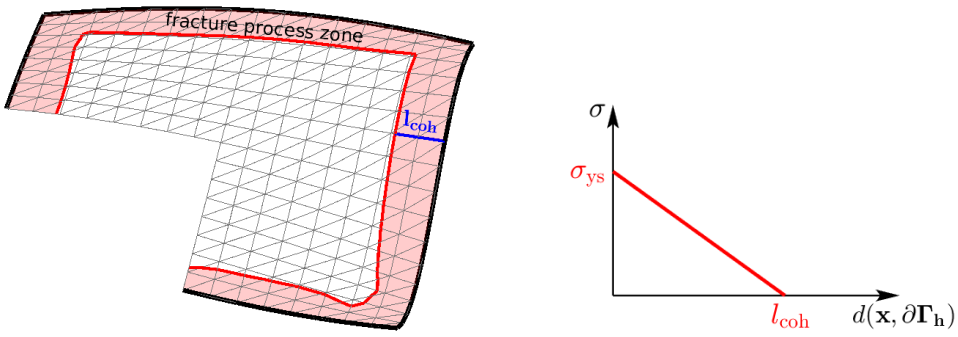

(a) (b)

Figure 5.2: Simplified cohesive crack model. (a) Fracture process zone and (b) cohesive law.

5.2 Stress functions based on distances to the crack-front

The spatial or geodesic distances to the crack-front (Secs. 4.2 and 4.3) are very important for the evaluation of the local coordinate system (a, b) or the polar coordinate system (r, θ), see Sec. 3.1.3.1. They can also be used to define pre-defined stress functions on Γ_h which is discussed next in the context of a simplified cohesive crack model, respectively.

As soon as the inelastic region at the crack-tip (fracture process zone) is no longer negligible small, the assumptions of LEFM becomes inaccurate. A very simple correction can be performed by applying some crack closure tractions $\boldsymbol{t}_{\mathrm{coh}}$ in the vicinity of the crack-tip/front which is known as the cohesive crack model [12, 59, 89]. Usually, these tractions depend on the crack opening, see, e.g., [76, 89, 110, 127] for different traction-opening relationships. In the proposed simplified cohesive model, crack closure tractions are applied within a fixed region around the crack-front which is defined based on the length l_{coh} of the fracture process zone, see Fig. 5.2(a). Furthermore, it is assumed that the tractions $\boldsymbol{t}_{\mathrm{coh}}(\boldsymbol{x})$ of a point $\boldsymbol{x}$ within this region rather depend on the distance between $\boldsymbol{x}$ and $\partial\Gamma_h$ than on the opening, see Fig. 5.2(b) where a corresponding cohesive law is illustrated, respectively. That is, the spatial distances $d_{\boldsymbol{x}}(\boldsymbol{x})$ or geodesic distances $d_{\Gamma}(\boldsymbol{x})$ of a point $\boldsymbol{x}$ to the crack-front are used to evaluate $\boldsymbol{t}_{\mathrm{coh}}(\boldsymbol{x})$. The corresponding length of the plastic zone l_{coh} is determined based on the strip-yield model [12, 59], the fracture toughness K_{Ic} and the yield stress σ_{ys} with [187]

$$l_{\mathrm{coh}} = \frac{\pi}{8}\left(\frac{K_{\mathrm{Ic}}}{\sigma_{\mathrm{ys}}}\right). \tag{5.3}$$

It is noted that cohesive crack models are not the focus of this thesis and are only mentioned to show an application in which stress functions can be related to distances to the crack-front. The proposed procedure is not restricted to a specific model, wherefore

any stress functions which can be related to such distances can be applied.

5.3 Stress functions based on virtual distances

A simplified fluid model is introduced in the context of HF based on the dimensionless virtual distances $\tilde{d}_v$ which were discussed in Sec. 4.4.3. HF processes are usually described as non-linear and time-dependent coupled problems, where the fluid pressure p is related to the crack width w. This relation can be expressed by a non-linear model known as the Reynolds equation [2, 15]

$$\frac{\partial w}{\partial t} = \frac{1}{\mu'} \nabla \cdot \left(w^3 \nabla p \right) + Q(t)\delta(\boldsymbol{x}) - q_l. \tag{5.4}$$

It is obtained by combining Poiseulle's law for fluid flux with the continuity equation. Injection rates are assumed to be small enough that the assumption of a laminar flow subjected to friction between two infinite parallel plates is valid. Based on the Reynolds equation the fluid pressure mainly depends on the injection rate Q, the crack width w, the fluid viscosity μ, the leak-off q_l and the time t. Additional influences through a fluid lag l_f were investigated, e.g., in [74, 90]. For simple crack geometries, resulting pressure distributions are given in the literature according to different propagation regimes, e.g., [1, 3, 5, 48, 157]. It was observed that the assumption of a uniform pressure,

$$\Pi_{k0} = \text{const}, \tag{5.5}$$

is suitable for large toughness (zero viscosity) problems [48]. The magnitude of the pressure depends on the investigated problem, for example, $\Pi_{k0} = \frac{\pi^{1/3}}{8}$ for the KGD-model and $\Pi_{k0} = \frac{\pi}{8}\left(\frac{\pi}{12}\right)^{1/5}$ for a penny-shaped crack [1, 5, 48]. On the other hand, zero toughness (viscosity-dominated) problems lead to singular pressures at the crack-tip. Dimensionless pressure distributions are given for a viscosity-dominated propagation based on the KGD-model and a penny-shaped crack, for example, in [3, 157]. The first order approximations of the dimensionless pressure distributions due to a viscosity-dominated propagation for the KGD-model can be written as [3]

$$\Pi_{m0}^{\mathrm{KGD}}(\rho) = \frac{1}{3\pi} B(1/2, 2/3) \left[\sqrt{3} \cdot {}_2F_1(-1/6, 1, 1/2, \rho^2) - 10/7 \cdot 0.156 \cdot {}_2F_1(-7/6, 1, 1/2, \rho^2) \right] + 0.0663(2 - \pi\rho), \tag{5.6}$$

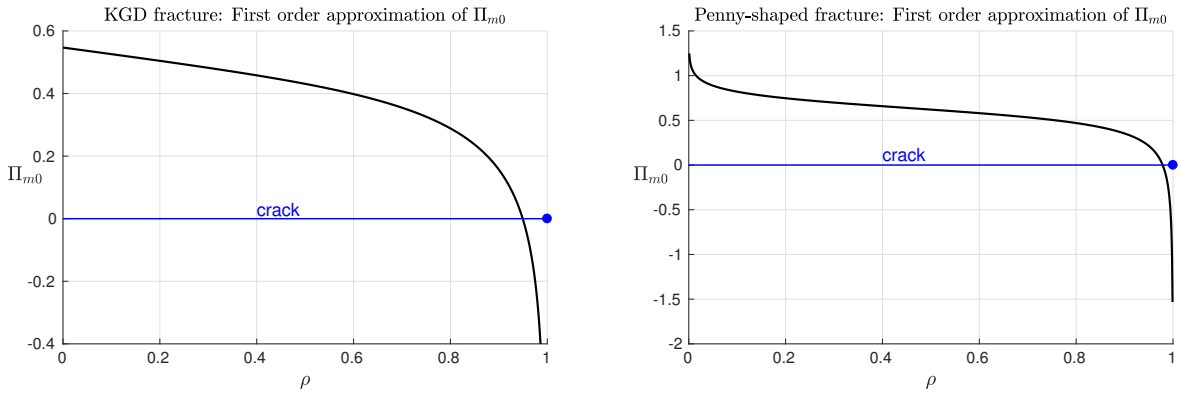

(a) (b)

Figure 5.3: First order approximation of the pressure Π_{m0} for a viscosity-dominated (a) KGD fracture, and (b) penny-shaped fracture.

and for a penny shaped crack as [157]

$$\Pi_{m0}^{\text{Penny}}(\rho) = 0.795 - \frac{0.239}{(1-\rho)^{1/3}} - 0.0911 \cdot \ln(0.5\rho). \tag{5.7}$$

Herein, B is the Euler beta function, ${}_2F_1$ is the hypergeometric function, and ρ is the scaled coordinate which is 0 at the injection point and 1 at the crack-tip/front. Fig. 5.3 shows a graphical illustration of Eq. 5.6 and Eq. 5.7.

The coupling of the elasticity and fluid problem is often associated with numerical problems often leading to a large number of iterations giving rise to instabilities [2]. Furthermore, due to the fact that the evaluation of the pressure is computationally expensive and there are only few experimental data available for the validation, there is a strong motivation to simplify this delicate coupled problem. Furthermore, in most industrial applications of HF the focus may rather be on the resulting shape of the fracture, pressure and fluid volume over time and less complicated models may serve this purpose as well. In this contribution, we introduce a simplified model which has the advantage that it is very robust and computationally cheap because no iterations between different models, e.g., fluid-structure interactions, are required. It is noted that the proposed model is not restricted to a specific application but can be used for a wide range of applications with loaded crack surfaces. Herein, the simplified model is discussed in the context of HF, respectively.

In HF, one may suggest to replace the Reynolds equation by pre-defined pressure distributions similar to those from above but scaled by only few parameters which increases the robustness and decreases the computational efforts. Herein, the assumed distribution is based on the knowledge of the dominated regimes (toughness and viscosity) which can

vary during the time. The aim is to develop a simple, robust and computationally cheap simulation tool for '*quasi static*' HF-processes which enables a satisfactory prediction of the obtained crack configuration, in particular to the corresponding crack geometry or volume and the corresponding pressure over time t. In the next section, a simplified fluid model is introduced based on a scaling function $\Phi(t)$ and the known pressure distributions Π_{k0} and Π_{m0}.

5.3.1 Scaling function

As a simplification it is assumed that all pressure distributions during the propagation are reproduced as a linear combination of the toughness-dominated distribution $p(p_0, \rho) = p_0$ and the viscosity-dominated case $p(p_0, \rho) = p_0 \cdot \Pi_{m0}(\rho)$. The influence of each regime is considered by a time-dependent (crack-size dependent) scaling function $0 \leq \Phi(t) \leq 1$ which represents the dominance of the toughness-dominated regime [163]. That is, the propagation is with $\Phi(t) = 1$ purely toughness- and with $\Phi(t) = 0$ purely viscosity-dominated. Based on this scaling function, the current pressure distribution at a time t is given by [163, 164]

$$p(p_0, \rho, t) = p_0 \left[\Phi(t) + (1 - \Phi(t))\, \Pi_{m0}(\rho)\right]. \tag{5.8}$$

Fig. 5.4(a) shows an exemplary scaling function which describes the time-dependent transition of a viscosity-dominated propagation to a toughness-dominated propagation. Based on Eq. 5.8 the resulting pressure distribution due to a prescribed scaling value $\Phi(t) = 0.95$ of a KGD-model is illustrated in Fig. 5.4(b).

It is noted that this kind of pressure distribution should only highlight the construction of some general yet physically motivated pressure distributions as possible loadings on crack surfaces. In this work, different distributions are used for the validation of the proposed method and the focus is here rather on the availability of reference solutions than practical examples of industrial relevance. The critical pressure magnitude which leads to a crack propagation, see Sec. 6, is determined based on the superposition principle of LEFM. It is important that the original Reynolds model may also be used within the proposed approach. However, as this may induce numerical problems we rather prefer to allow for arbitrary yet user-prescribed pressure profiles in this approach as mentioned above. The transition between the different regimes may itself be a (time-dependent) function which is an additional free parameter in the proposed approach.

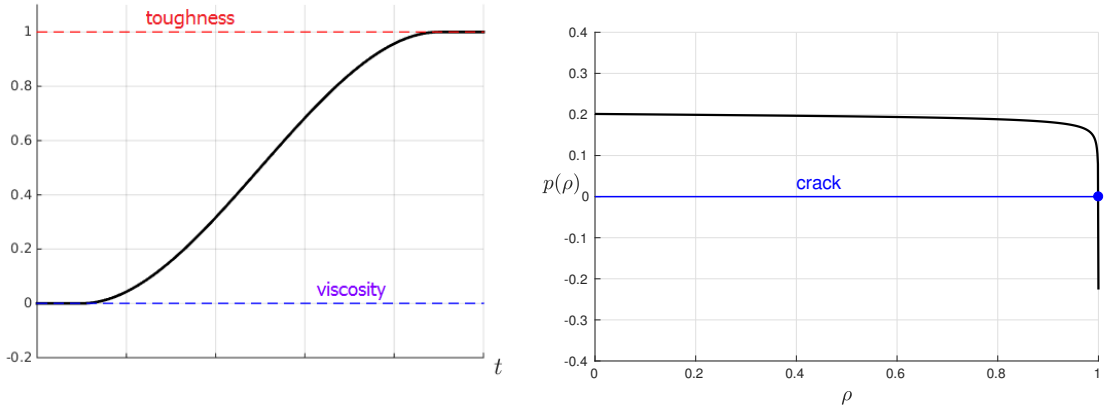

(a) (b)

Figure 5.4: (a) Scaling function which considers time-dependent changes of the pressure distribution during propagation and (b) the resulting pressure distribution due to a prescribed scaling value $\Phi(t) = 0.95$ in the context of a simplified fluid model in HF.

5.3.2 Mapping of dimensionless pressure distributions onto Γ_h

The pre-defined pressure distributions of Eq. 5.8 which were introduced in the context of HF are defined based on a scaled coordinate ρ which is 0 at the injection point and 1 at the crack-tip/front, see Fig. 5.3. A challenging task is the mapping of these dimensionless distributions onto the physical crack geometry of the structure which could be curved and arbitrarily shaped. In addition, also the injection point may be arranged arbitrarily, see Sec. 4.4.

The mapping is based on the dimensionless virtual distances $\tilde{d}_v(\boldsymbol{x})$ which represent the scaled coordinate ρ of Eq. 5.8. Its construction in Γ_h was carefully discussed in Sec. 4.4 and the projection of these distances from the explicit to the implicit crack geometry is discussed in Sec. 5.4. If $\tilde{d}_v(\boldsymbol{x}_i)$ of a point $\boldsymbol{x}_i$ is known, the corresponding pressure value of the simplified fluid model (Eq. 5.8) is given by

$$p(\boldsymbol{x}_i) = p(\tilde{d}_v(\boldsymbol{x}_i)). \tag{5.9}$$

It is noted that the proposed projection procedure of Sec. 5.4.1 can also be used in a more general framework to project arbitrary functions (pressure profiles) which are defined on Γ_h onto the implicitly defined zero level-sets.

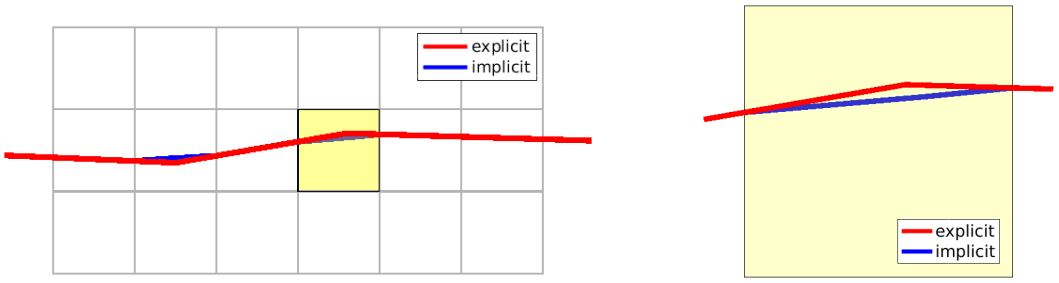

(a) (b)

Figure 5.5: Explicit and implicit crack geometry within the physical (a) mesh and a (b) physical element.

5.4 Data transfer between the explicit and implicit crack description

As discussed in Sec. 3, a hybrid explicit-implicit crack description has many advantages over a purely implicit or explicit description. However, this combined formulation leads to two different crack geometries which may not coincide exactly, wherefore data has to be transferred between these descriptions [164]. The difference between these two crack descriptions is illustrated in Fig. 5.5 where the explicit and implicit crack geometry is shown within the physical mesh of the domain or within a physical element.

5.4.1 Projection from the explicit to the implicit crack geometry

In this section, the focus is placed on the mapping of a function f^h from the explicit crack geometry Γ_h to the implicitly defined zero level-sets which is required, e.g., to determine the function value $f^h(\boldsymbol{x}_i^\star)$ at the (integration) points $\boldsymbol{x}_i^\star$ of the implicit crack geometry. This projection may also be used in a more general framework, for example, in the context of HF, where fluid models are often solved on explicitly defined surface meshes and their results are then mapped to the implicit description of the crack surface. This projection is discussed here in a general framework where a function f is given by its nodal values f_j on the explicit surface mesh Γ_h and is interpolated at points of the implicit description of the surface. As mentioned above, this implicitly defined crack geometry may not coincide exactly with the explicit description which complicates the interpolation of the required functions.

In the following, $\boldsymbol{r}_i^\star$ represent integration points within the two-dimensional reference 'crack elements' which were introduced in Sec. 3.3.1 and $\boldsymbol{x}_i^\star$ represent the mapped integration points in the global Cartesian coordinates of the mesh. The detection of the zero level-sets and the mapping of $\boldsymbol{r}_i^\star$ to $\boldsymbol{x}_i^\star$ was already discussed in Sec. 3.3. The task is now to obtain a proper function value at $\boldsymbol{x}_i^\star$ based on given nodal function values at

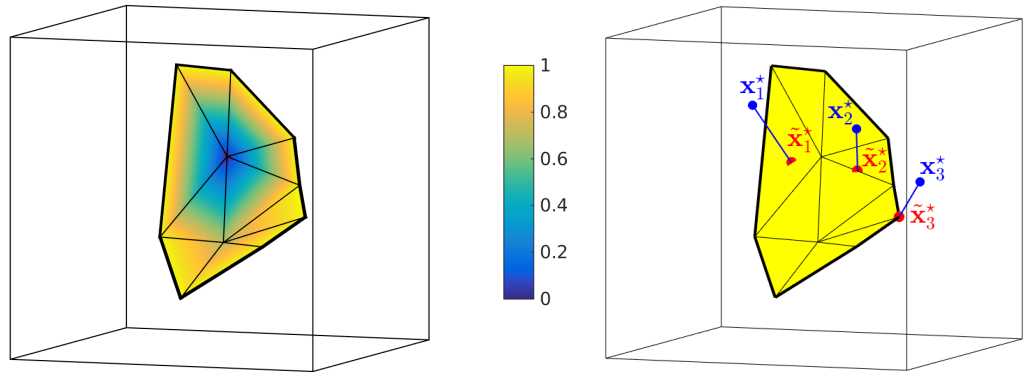

(a) Function given on the explicit crack geometry.

(b) Find closest point on the surface mesh.

Figure 5.6: Data projection from the explicit to the implicit crack geometry.

the nodes of the explicit surface mesh. Therefore, the closest point on the surface mesh has to be identified and labelled $\tilde{\boldsymbol{x}}_i^\star$. Examples are seen in Fig. 5.6 where the closest point $\tilde{\boldsymbol{x}}_1^\star$ is within a triangle, $\tilde{\boldsymbol{x}}_2^\star$ on an edge, and $\tilde{\boldsymbol{x}}_3^\star$ at a vertex, respectively. At this point the function value is interpolated based on the finite element shape functions N_i on the explicit crack surface mesh and their corresponding nodal function values. Then, it is assumed that the function value $f^h(\tilde{\boldsymbol{x}}_i^\star)$ is equivalent to the function value $f^h(\boldsymbol{x}_i^\star)$. That is, the proposed data transfer procedure defines the function value $f^h(\boldsymbol{x}_i^\star)$ at the integration points $\boldsymbol{x}_i^\star$ of the implicit crack geometry as follows

$$f^h(\boldsymbol{x}_i^\star) := \sum_{j \in I_\Gamma} N_j(\tilde{\boldsymbol{x}}_i^\star) f_j. \tag{5.10}$$

I_Γ is the set of element nodes of the explicitly defined surface mesh and f_j are the corresponding nodal values of the function f.

Such a projection is well-known in the context of non-matching meshes, see [25] for an example in fluid-structure interaction. Since the distance between the explicit and implicit crack description is generally very small, see Fig. 5.5(a), and the changes of the explicitly defined functions are often moderate over the crack surface, it is seen that this approach provides satisfactory results in general.

5.4.2 Data transfer from the implicit to the explicit crack geometry

A data transfer from the implicit to the explicit crack description may also be desired. An example is found in HF where the crack width based on the XFEM-approximation may be needed for the flow model on the crack surface. A very simple and fast procedure is based on a nearest neighbour interpolation [185] where the required information are

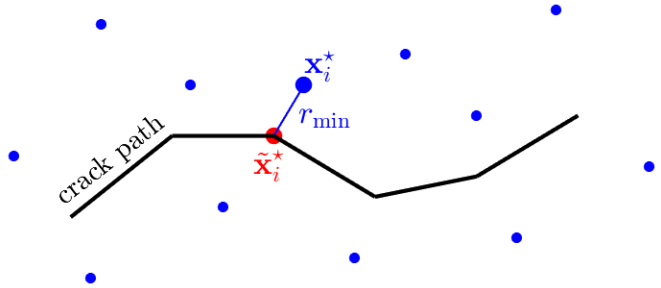

Figure 5.7: Data transfer from the implicit to the explicit crack geometry based on a nearest neighbour interpolation.

obtained from the closest point of the other mesh. For example, displacement quantities such as openings are computed at different points on the implicit crack surface in a post-processing of the XFEM-approximation. These points are mapped with their stored information to the global coordinate system. For all required points on the explicit surface mesh, the value of the closest point to this point cloud is used, see Fig. 5.7. It is noted that the maximum element size of the surface mesh and the background mesh should be in a similar range to represent physically meaningful quantities on both meshes.

6 Crack propagation

In LEFM, the decision whether a crack propagates is often based on the SIF K_{I} or the material toughness K_{Ic}. It is assumed that a propagation occurs when the current mode I SIF K_{I} exceeds the material toughness. This criterion takes the form

$$K_{\mathrm{I}} = K_{\mathrm{Ic}}, \tag{6.1}$$

which only considers mode I loadings. For an arbitrary three-dimensional crack configuration, a more general formulation is based on the energy release rate G which is a measure of the energy available for the creation of new crack faces, see Sec. 2.2.1. Similar to Eq. 6.1, a propagation occurs when the current energy release rate G reaches a critical value G_c:

$$G = G_c. \tag{6.2}$$

A commonly used technique for the evaluation of G is the J-integral [152] (Sec. 2.2.5) because they are equivalent in LEFM [117, 187]. This procedure has the advantage that only a small region around the crack-tip/front has to be considered for the computation of G instead of the entire domain. In this thesis, another technique is used where G is computed based on Eq. 2.13 through the corresponding SIFs. The required SIFs can be obtained, e.g., from the interaction integral [195] (Sec. 2.2.6) or from correlation methods [30, 87, 94, 159, 161]. A disadvantage of the J-integral and the interaction integral is that their extensions to three dimensions causes some difficulties [195]. In contrast, correlation methods allow a straightforward extension to three dimensions which is discussed in more detail in Sec. 6.1.

It is important to note that in three dimensions, that is, in the context of crack *surfaces*, every point on the crack-front may be associated with an individual value for the energy release rate G. It is, however, not useful to propagate a single point (including a tiny part of its neighborhood on the front) when G_c is met at one point of the front. Therefore, we assume that the critical point where G_c is reached grows with an increment length $\Delta r_{\max}$ and all other points grow with proportionally scaled lengths. These scalings are based on the corresponding ratios of the varying local energy release rates G_i and the critical G_c. For this, it follows that a point i with an energy release rate G_i grows with an increment

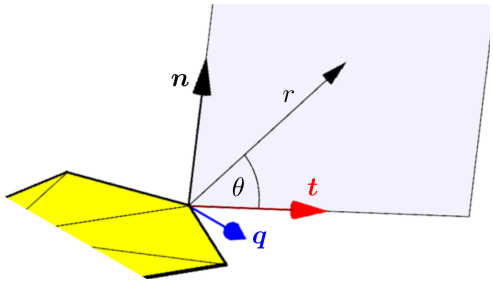

Figure 6.1: Coordinate system at the crack-front.

length Δr_i of

$$\Delta r_i = \frac{G_i}{G_c} \cdot \Delta r_{\max}. \tag{6.3}$$

For keeping the number of considered points along the crack-front reasonable, we restrict the assessment of the propagation to 'crack-front nodes' which are the nodes of the explicit crack surface mesh at the front. Their connection represents the crack-front by a three-dimensional C_0-continuous polygon which bounds the explicit crack surface mesh of Sec. 3.1.3.

In the literature, a wide range of reliable and accurate propagation criteria exists for the evaluation of the propagation direction. Common criteria are, e.g., the maximum circumferential stress criterion [63], the maximum strain criterion [122], the maximal strain energy release rate criterion [91], and the minimum strain energy density criterion [170]. In this contribution, the evaluation of the propagation direction is based on the maximum circumferential stress criterion [63] where the propagation angle θ_c can be evaluated in the $\boldsymbol{n}$-$\boldsymbol{t}$-plane, see Fig. 6.1, based on the corresponding SIFs. For $K_{\mathrm{II}} \neq 0$ this criterion leads to the following expression

$$\theta_c = 2 \arctan \frac{1}{4} \left(\frac{K_{\mathrm{I}}}{K_{\mathrm{II}}} - \operatorname{sign}(K_{\mathrm{II}}) \cdot \sqrt{\left(\frac{K_{\mathrm{I}}}{K_{\mathrm{II}}} \right)^2 + 8} \right). \tag{6.4}$$

When $K_{\mathrm{II}} = 0$ the crack propagates straight which means that the propagation angle $\theta_c = 0$. The propagation out of the $\boldsymbol{n}$-$\boldsymbol{t}$-plane due to mode III is neglected in the maximum circumferential stress criterion, wherefore it is only suitable for situations where mode III is small compared to the other modes [16, 31]. For fluid-driven fractures this is often justified by the fact that the fluid pressure dominates the propagation against other loadings leading to a dominant SIF K_{I} compared to K_{II} and K_{III}. The influence of K_{III} in the crack propagation is a matter of ongoing research [119, 153].

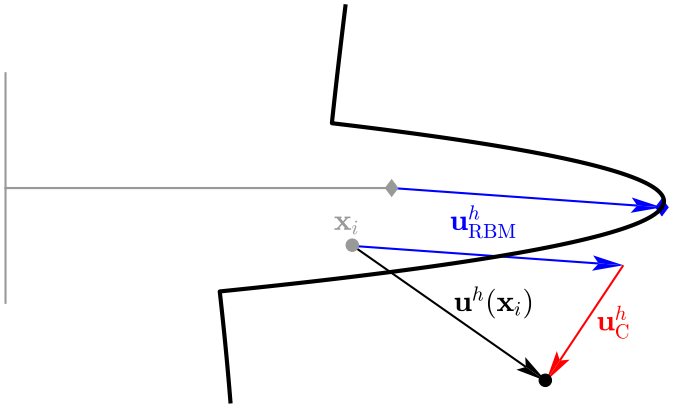

Figure 6.2: Approximated displacements of a point $\boldsymbol{x}_i$ in two dimensions.

6.1 Computation of SIFs through crack opening displacements

We propose a method for computing SIFs which investigates the displacement field in the vicinity of the crack-tip/front. Similar approaches using crack opening displacements (CODs) are found in [30, 94, 135] in the field of classical FEM and in [87, 161] in XFEM-related approaches. This method is intuitive and the extension from two to three dimensions is straightforward and treats mode III as the other modes. Furthermore, no modification is necessary for curved and loaded cracks. The approximated displacements $\boldsymbol{u}^h(\boldsymbol{x}_i)$ of a point $\boldsymbol{x}_i$, which are extracted from the XFEM simulation, are compared with the expected displacements for a pure mode I, II and III crack. Because the situation at $\boldsymbol{x}_i$ is compared to some reference situation, we may also think of this as fitting and call the respective point *fitting point*. That is, two different states are involved which are described in more detail in the Secs. 6.1.1 and 6.1.2.

It is noted that the approximated displacement $\boldsymbol{u}^h(\boldsymbol{x}_i)$ of a fitting point $\boldsymbol{x}_i$ consists of a displacement $\boldsymbol{u}^h_{\mathrm{RBM}}$ due to a rigid body motion and a displacement $\boldsymbol{u}^h_{\mathrm{C}}$ due to the crack opening, see Fig. 6.2. For the computation of SIFs, the displacement $\boldsymbol{u}^h_{\mathrm{RBM}}$ has to be extracted because rigid body motions are not considered in the reference states for pure mode I, II and III cracks which complicates the computation. Therefore, we prefer to use relative displacements $\Delta\boldsymbol{u}$, particularly the CODs, as shown in Fig. 6.3 which consider rigid body motions automatically. The relative displacement $\Delta\boldsymbol{u}^h_{\mathrm{COD}}$ contains the first two modes in two dimensions and all three modes in three dimensions, wherefore all modes can be extracted from this opening. In the following, the computation of the approximated and expected CODs is discussed in more detail. In Sec. 6.1.3, the computation of SIFs is discussed based on selected directions of the CODs where the best results can be expected.

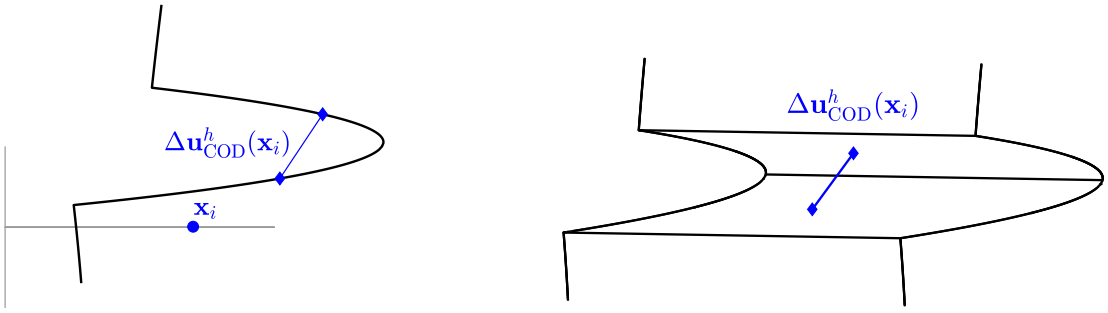

(a) (b)

Figure 6.3: Approximated CODs in (a) two and (b) three dimensions.

6.1.1 Approximated state

This section shows the computation of the approximated crack opening $\Delta \boldsymbol{u}^h_{\mathrm{COD}}(\boldsymbol{x}_i)$ of a fitting point $\boldsymbol{x}_i$ on the crack path/surface. The crack openings of the fitting point $\boldsymbol{x}_i$ are computed after solving the LEFM problem based on Eq. 3.21 as a post-processing step. The difficulty here is that the enrichment and shape functions have to be evaluated in a special setting so that CODs are obtained. Starting point is a fitting point $\boldsymbol{x}_i$ on the implicitly defined crack geometry which is 'split' into two opposite but infinitesimally close points $\boldsymbol{x}_{i^+}$ and $\boldsymbol{x}_{i^-}$ being on either side of the crack surface. The detection of the fitting point on the crack surface and its splitting is done equivalently to the proposed procedure which is used in Sec. 3.3.3 for the surface integration. The level-set functions and the corresponding local coordinates (a,b) are interpolated at these points. Based on these interpolated functions, the corresponding polar coordinates $r(\boldsymbol{x}_{i^\pm})$ and $\theta(\boldsymbol{x}_{i^\pm})$ are determined with Eqs. 3.9 and 3.10. These coordinates are used in Eq. 3.21 to define the enriched shape functions of the approximation which are required for the computation of the approximated displacements $\boldsymbol{u}^h_{\mathrm{COD}}(\boldsymbol{x}_{i^+})$ and $\boldsymbol{u}^h_{\mathrm{COD}}(\boldsymbol{x}_{i^-})$. Based on these displacements the crack opening $\Delta \boldsymbol{u}^h_{\mathrm{COD}}(\boldsymbol{x}_i)$ is given with

$$\Delta \boldsymbol{u}^h_{\mathrm{COD}}(\boldsymbol{x}_i) = \boldsymbol{u}^h_{\mathrm{COD}}(\boldsymbol{x}_{i^+}) - \boldsymbol{u}^h_{\mathrm{COD}}(\boldsymbol{x}_{i^-}). \tag{6.5}$$

For the sake of clarity, the index 'COD' is not written anymore, instead, the index is used to give information about the current coordinate system, where $(\boldsymbol{x})$ describes the global coordinate system and $(\boldsymbol{a})$ the local coordinate system mentioned in Sec. 3.1.3.1.

6.1.2 Reference states for pure mode I, II and III cracks

In this section, the reference state is discussed which is needed for the evaluation of the expected CODs for a pure mode I, II and III crack, respectively. For straight or planar crack

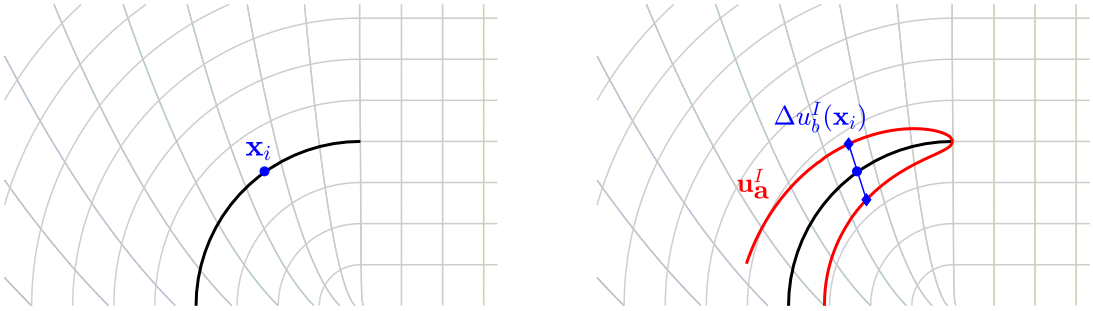

(a) (b)

Figure 6.4: Reference state of a curved crack in the (a,b)-coordinate system in (a) a closed and (b) an open setting.

geometries, the definition of the reference configuration can be based on an orthonormal coordinate system which is aligned with the tangent at the crack-tip/front. However, in practical applications, cracks are often curved, especially for propagating cracks where mode II is dominant. For such problems, the use of an orthonormal coordinate system is not easily justified and leads to the wrong crack opening in the reference state. We propose the definition of a reference state based on the local coordinate system (a,b) which is also valid for curved cracks, see Fig. 6.4. The definition of this coordinate system has been discussed in Sec. 3.1.3.1.

A complete description of the crack-tip/front behaviour is given by a linear combination of three independent crack modes which are scaled by the SIFs $K_\mathrm{I}, K_\mathrm{II}$ and K_III, see Sec. 2.2.3. Under general mixed-mode loadings, the displacements are given in the (a,b,c)-coordinate system by [187]:

$$\begin{bmatrix} u_a \\ u_b \\ u_c \end{bmatrix} = \begin{bmatrix} \frac{K_\mathrm{I}}{2\mu}\sqrt{\frac{r}{2\pi}}\cos\frac{\theta}{2}\left(\kappa - 1 + 2\sin^2\frac{\theta}{2}\right) + \frac{K_\mathrm{II}}{2\mu}\sqrt{\frac{r}{2\pi}}\sin\frac{\theta}{2}\left(\kappa + 1 + 2\cos^2\frac{\theta}{2}\right) \\ \frac{K_\mathrm{I}}{2\mu}\sqrt{\frac{r}{2\pi}}\sin\frac{\theta}{2}\left(\kappa + 1 - 2\cos^2\frac{\theta}{2}\right) - \frac{K_\mathrm{II}}{2\mu}\sqrt{\frac{r}{2\pi}}\cos\frac{\theta}{2}\left(\kappa - 1 - 2\sin^2\frac{\theta}{2}\right) \\ \frac{2K_\mathrm{III}}{\mu}\sqrt{\frac{r}{2\pi}}\sin\frac{\theta}{2} \end{bmatrix}, \tag{6.6}$$

with μ being the shear modulus which is defined in Eq. 2.14 and the material parameter κ

$$\kappa = \begin{cases} \frac{3-\nu}{1+\nu} & \text{for plane stress,} \quad (6.7) \\ 3 - 4\nu & \text{for plane strain.} \quad (6.8) \end{cases}$$

As Eq. 6.6 shows, displacements out of the plane only exist if mode III is non-zero. However, displacements in direction of a and b consist of a combination of mode I and II for any $0 < |\theta| < \pi$. It is noted that in three dimensions, only Eq. 6.8 makes sense and

each point on the crack-front has its own SIFs.

Based on the interpolated polar coordinates $r(\boldsymbol{x}_{i\pm})$ and $\theta(\boldsymbol{x}_{i\pm})$ of the split fitting point $\boldsymbol{x}_i$ (see Sec. 6.1.1), the expected displacements $\boldsymbol{u}_{\boldsymbol{a}}^m(\boldsymbol{x}_{i^+})$ and $\boldsymbol{u}_{\boldsymbol{a}}^m(\boldsymbol{x}_{i^-})$ are computed with Eq. 6.6 due to a pure mode $m = \{\mathrm{I}, \mathrm{II}, \mathrm{III}\}$. This can be achieved by setting the current SIF K_m to 1 and the others to 0. The expected COD of mode m is then given in the local coordinate system by the difference of the expected displacements of both points with

$$\Delta\boldsymbol{u}_{\boldsymbol{a}}^m(\boldsymbol{x}_i) = \boldsymbol{u}_{\boldsymbol{a}}^m(\boldsymbol{x}_{i^+}) - \boldsymbol{u}_{\boldsymbol{a}}^m(\boldsymbol{x}_{i^-}). \tag{6.9}$$

In Fig. 6.4(b), the expected opening (red line) for a pure mode I is presented in the (a,b)-coordinate system. Furthermore, the expected COD of the fitting point $\boldsymbol{x}_i$ in direction of b (blue line) is illustrated. In the following section, the computation of SIFs based on the evaluated CODs in the approximated and reference state is discussed.

6.1.3 Evaluation of SIFs

A comparison of the approximated and expected openings is only possible if both openings are described in the same coordinate system. Therefore, the approximated CODs, which are given in the global coordinate system (x,y,z), are transformed into the local coordinate system (a,b,c). In two dimensions, this is done based on the Jacobi-matrix $\mathbf{J}$ of the coordinate transformation, hence,

$$\Delta\boldsymbol{u}_{\boldsymbol{a}}^h = \mathbf{J} \cdot \Delta\boldsymbol{u}_{\boldsymbol{x}}^h \qquad \text{with} \quad \mathbf{J} = \begin{bmatrix} a_{,x} & a_{,y} \\ b_{,x} & b_{,y} \end{bmatrix}. \tag{6.10}$$

It is noted that ∇a and ∇b are only orthonormal for straight/planar cracks. In three dimensions, we define the gradient of a third function c through the cross-product of ∇a and ∇b:

$$\nabla c = \nabla a \times \nabla b. \tag{6.11}$$

With this information of the third direction, Eq. 6.10 is straightforwardly extended to the third dimension and the transformation into the local coordinate system is performed as follows

$$\Delta\boldsymbol{u}_{\boldsymbol{a}}^h = \mathbf{J} \cdot \Delta\boldsymbol{u}_{\boldsymbol{x}}^h \qquad \text{with} \quad \mathbf{J} = \begin{bmatrix} a_{,x} & a_{,y} & a_{,z} \\ b_{,x} & b_{,y} & b_{,z} \\ c_{,x} & c_{,y} & c_{,z} \end{bmatrix}. \tag{6.12}$$

Now that both CODs are available in the local coordinate system, the comparison of the approximated and expected CODs leads to the following system of equations:

$$\Delta \boldsymbol{u}_{\boldsymbol{a}}^{h} = K_{\mathrm{I}} \cdot \Delta \boldsymbol{u}_{\boldsymbol{a}}^{\mathrm{I}} + K_{\mathrm{II}} \cdot \Delta \boldsymbol{u}_{\boldsymbol{a}}^{\mathrm{II}} + K_{\mathrm{III}} \cdot \Delta \boldsymbol{u}_{\boldsymbol{a}}^{\mathrm{III}}. \tag{6.13}$$

It is noted that the impact of the individual SIFs to the displacement components of a point which is 'quasi' on the crack surface with $\theta = \pm(\pi - \varepsilon)$ is quite different, see Eq. 6.6. K_{I} mainly leads to displacements in direction of b, K_{II} to displacements in direction of a and K_{III} to displacements in direction of c. Therefore, SIFs are directly computed by using these selected directions with

$$K_{\mathrm{I}} = \Delta u_b^h / \Delta u_b^{\mathrm{I}}; \qquad K_{\mathrm{II}} = \Delta u_a^h / \Delta u_a^{\mathrm{II}}; \qquad K_{\mathrm{III}} = \Delta u_c^h / \Delta u_c^{\mathrm{III}}. \tag{6.14}$$

The accuracy of the determined SIFs based on the proposed method has already been demonstrated for stress-free and uniform loaded crack surfaces by the author in [161] and shall later on be discussed in the numerical results presented in Sec 7. Recently developed improvements or extensions of the standard XFEM such as, e.g., adaptive mesh refinements [99, 191, 196] or applied consecutive interpolation procedures [103–105] may further increase the accuracy of the computed SIFs, however, they are not the focus of this thesis. It remains to specify the location of the considered fitting points and the consideration of the crack-front in the context of a numerical simulation.

6.1.4 Location of the fitting points

It is well-known that the SIFs and their related displacements only characterize the situation when asymptotically approaching the crack-tip/front. Therefore, it is obvious that the region where SIFs are obtained from the CODs must be restricted to the near tip/front region. Physically, the most accurate SIFs are evaluated at points which are located infinitesimally close to the crack-tip/front. However, the numerically obtained results are less accurate there due to the singular stresses, which renders the positioning of fitting points a difficult task. Therefore, it is proposed to use a number of points in a region near the crack-tip/front and compute averaged SIFs which also leads to an increased robustness. Numerical results indicate that 5% of a characteristic crack length l_a, see Fig. 6.5, yield satisfactory results. The evaluation ofl_a is based on four crack types which are described in Tab. 6.1 and are illustrated in Fig. 6.5. In two dimensions, l_a can be expressed directly through the crack path length l_{cp} taking into account the number of crack-tips (Type I or II), see Figs. 6.5(a-b). In three dimensions, there is no 'classical' crack length available, wherefore an *effective* crack length l_c^{eff} is introduced here which is described by

Crack type	Description
I	Crack path with one crack-tip.
II	Crack path with two crack-tip.
III	Crack surface with an open crack-front.
IV	Crack surface with a closed crack-front.

Table 6.1: Definition of the four crack types.

the ratio of the area of the crack surface A_c and the length of the crack-front l_{cf}:

$$l_c^{\mathrm{eff}} = \frac{A_c}{l_{\mathrm{cf}}}. \tag{6.15}$$

This definition is used because it is computationally cheap, robust and provides suitable results for the crack types III and IV, e.g., the effective crack length l_c^{eff} is for type III independent of the crack width b. For the four crack types, the relations between l_{cp} or l_c^{eff} and the characteristic crack length l_a are illustrated in Fig. 6.5.

6.1.5 Consideration of the crack-front

We have discussed how a point near the crack-tip/front may be used to obtain SIFs at a related node right on the crack-tip/front. For this purpose, several points may be used and their values averaged. The localisation of these points which are representative for one special point at the crack-front is not unique and the outcome of empirical studies. It is assumed that the point $\boldsymbol{x}_i$ is valid for the point $\hat{\boldsymbol{x}}_i$ on the crack-front where it has a minimum distance, see Fig. 6.6(a). When using an explicit-implicit crack description, the propagation is considered by adding new segments to the existing crack-front. In [68], a procedure has been introduced in which the crack geometry is updated based on the information available at the explicitly defined *nodes* of the crack-front. Based on this update procedure, it is sufficient that the SIFs are determined only in these special nodes where the direction and distance of the propagation is evaluated, see Sec. 6.3. It can be assumed that the change of the SIFs along the crack-front changes slowly for physically justified crack surfaces. Therefore, each evaluated point $\hat{\boldsymbol{x}}_i$ is assigned to the explicitly defined crack-front node $\bar{\boldsymbol{x}}_n$ where the distance is a minimum, see Fig. 6.6(b). It is noted that the distance of $\hat{\boldsymbol{x}}_i$ and $\bar{\boldsymbol{x}}_n$ is also limited by 5% of the effective crack length, so that only the SIFs of points $\hat{\boldsymbol{x}}_i$ are considered for $\bar{\boldsymbol{x}}_n$ which are in the vicinity of $\bar{\boldsymbol{x}}_n$. However, this limitation is only used for coarsely described crack geometries.

In Fig. 6.6, a three-dimensional crack-front (bold black line) is presented with possible

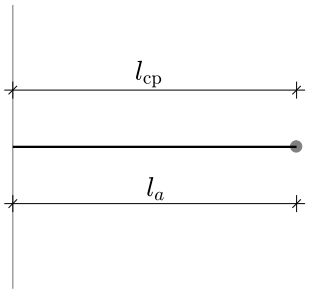

(a) Crack type I: $l_a = l_{\text{cp}}$

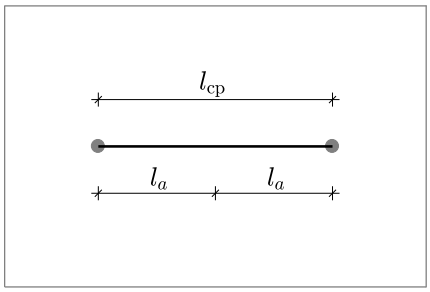

(b) Crack type II: $l_a = 0.5 \cdot l_{\text{cp}}$.

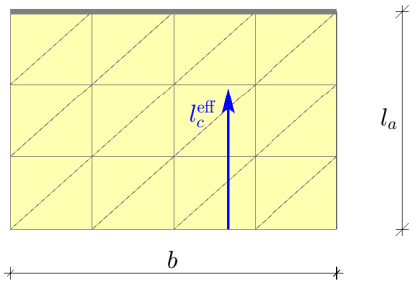

(c) Crack type III: $l_a = l_c^{\text{eff}}$.

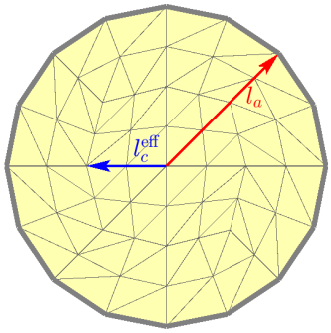

(d) Crack type IV: $l_a = 2 \cdot l_c^{\text{eff}}$.

Figure 6.5: Crack lengths which are used to limit the distances between fitting points and the crack-tip/front. For two-dimensional crack configurations with (a) one crack-tip and (b) two crack-tips or for crack surfaces with (c) open crack-fronts and (d) closed crack-front in three dimensions.

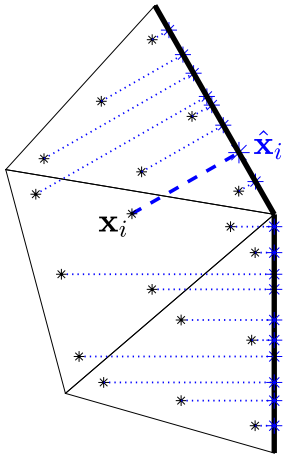

(a)

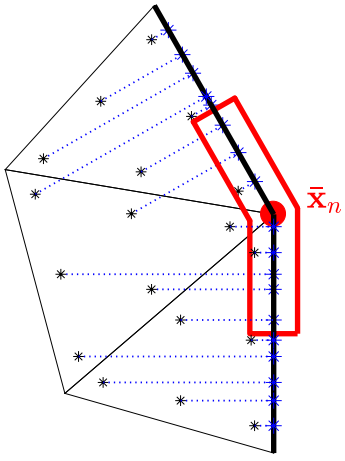

(b)

Figure 6.6: Three-dimensional crack-front: (a) Scope of computed SIFs and (b) assignment to crack-front node.

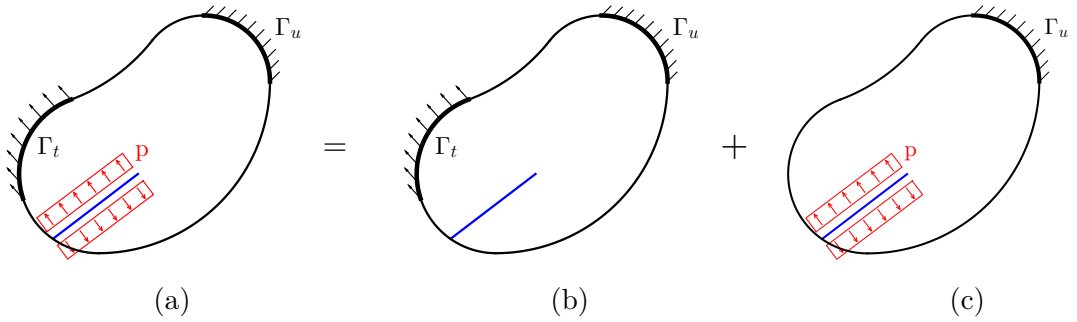

Figure 6.7: Superposition of an externally and internally loaded crack by means of the principle of superposition. (a) Total load, (b) external load, (c) internal load [162].

points $\boldsymbol{x}_i$ on the crack surface (black stars). The assignment of these points to the crack-front is illustrated by the blue dashed lines and the scope of the crack-front node $\bar{\boldsymbol{x}}_n$ is illustrated in red. The SIFs $K_m(\bar{\boldsymbol{x}}_n)$ are obtained by the average of all SIFs $K_m(\hat{\boldsymbol{x}}_i)$ of the points $\hat{\boldsymbol{x}}_i$ related to mode m which are assigned to this crack-front node. This can be expressed by

$$K_m(\bar{\boldsymbol{x}}_n) = \sum_{i=1}^{N} \frac{K_m(\hat{\boldsymbol{x}}_i)}{N}. \tag{6.16}$$

Based on the proposed procedure the SIFs are evaluated for each node of the crack-front in the explicit crack description. These SIFs are used in Sec. 6.3 to explicitly update the crack geometry.

6.2 External and internal loading cases

Two different loadings are distinguished here. The first is called 'external' and contains all stresses which come from the structure, such as body forces, prescribed tractions at the boundary, prescribed displacements etc. The second type of forces are stresses on the crack surface, typically pressure distributions, and are called 'internal' [162]. Fig. 6.7(a) shows a cracked domain where both loading types are present. This distinction is required as an increase of the internal load, e.g., through the pumping of the fracking fluid into the fracture, does not influence the external loads.

In LEFM, the energy release rate G_m of a mode m due to a number of n superimposed loads is given by

$$G_m = \left[\sqrt{G_m(f_1)} + \sqrt{G_m(f_2)} + \cdots + \sqrt{G_m(f_n)}\right]^2, \tag{6.17}$$

and the corresponding total energy release rate G_{total} is given by the sum of all three

modes $G_{\text{total}} = G_{\text{I}} + G_{\text{II}} + G_{\text{III}}$ [88, 146]. That is, the superposition of the external and internal loading case leads to

$$G_{\text{total}} = \left(\sqrt{G_{\text{I}}^{f}} + \sqrt{G_{\text{I}}^{p}}\right)^2 + \left(\sqrt{G_{\text{II}}^{f}} + \sqrt{G_{\text{II}}^{p}}\right)^2 + \left(\sqrt{G_{\text{III}}^{f}} + \sqrt{G_{\text{III}}^{p}}\right)^2, \tag{6.18}$$

where G_m^f and G_m^p represent the energy release rates due to the external loads f and the internal load p of mode m. As Eq. 6.18 shows, a modification of the pressure leads to a non-linear behaviour of the energy release rate. In the following, it is shown how to evaluate the critical pressure magnitude of a pre-defined pressure distribution based on Eq. 6.18.

6.2.1 Evaluation of critical pressure values

In this section, the evaluation of a critical pressure magnitude is discussed based on the superposition principle of LEFM. Although, the behaviour of a crack is strongly dependent on the crack geometry such as the crack length, there holds for a given crack configuration in a linear elastic material with a negligible plastic zone, for an initial prescribed pressure p_0 that their associated SIFs scale proportionally with

$$K_m^p(\lambda \cdot p_0) = \lambda \cdot K_m^p(p_0). \tag{6.19}$$

That is, the critical pressure p_c for a purely internally loaded crack configuration can be computed by a combination of Eqs. 6.2, 2.13 and 6.19 as

$$p_c = \lambda \cdot p_0 \qquad \text{with} \quad \lambda = \sqrt{\frac{G_c}{G\left(K_m^p(p_0)\right)}}. \tag{6.20}$$

Eq. 6.20 only holds when the initial pressure p_0 of an assumed pressure distribution $p(p_0, t)$ has no effect on the distribution which means that p_0 only describes the magnitude of the distribution.

When also external loads are present, a separate assessment of the crack behaviour caused by the external and internal loadings is necessary. A simple approach is possible by the superposition principle of LEFM where the crack configuration is decoupled into a part with only internal loadings and a part with only external loadings as shown in Fig. 6.7. The associated SIFs are denoted by K_m^f for the external case, K_m^p for the internal case and K_m^{total} for the combined case. It is noted that the proposed procedure allows an overlap of the crack surfaces due to the external loads f which causes no problems because this overlap is only used for the computation of p_c and is not allowed for the superimposed configuration, see Eq. 6.24. That is, for the external loads f the mode I SIF can be

negative and the following relation applies

$$K_m(f) = -K_m(-f). \tag{6.21}$$

For a λ-scaled pressure state the total SIFs K_m^{total} are given based on Eq. 2.12 by the sum of the external and the λ-scaled internal case as follows

$$K_m^{\text{total}} = K_m^f + \lambda K_m^p. \tag{6.22}$$

By using the crack propagation criterion of Eq. 6.2, a quadratic equation for the evaluation of the scaling factor λ is obtained [164], when Eq. 6.22 is inserted into Eq. 2.13 and Eq. 6.18, hence,

$$\begin{aligned} 0 = a\lambda^2 + b\lambda + c \qquad \text{with} \quad & a = G_m^p, \\ & b = \frac{2(1-\nu^2)}{E}\left(K_{\text{I}}^f K_{\text{I}}^p + K_{\text{II}}^f K_{\text{II}}^p\right) + \frac{1}{\mu} K_{\text{III}}^f K_{\text{III}}^p, \\ & c = G_m^f - G_c. \end{aligned} \tag{6.23}$$

This scaling factor λ enables the evaluation of the critical pressure p_c based on Eq. 6.20. It is noted that Eq. 6.23 generally has two solutions which are denoted by λ_1 and λ_2 herein. Usually, one of these scaling values is negative which describes the case where the crack surfaces overlap. If both solutions are positive, just one of these factors fulfills the required condition

$$K_{\text{I}}^{\text{total}}(\lambda_i) > 0. \tag{6.24}$$

The critical pressure fulfills the propagation criterion of Eq. 6.2 and the crack geometry can be explicitly updated based on Eq. 6.3 and Eq. 6.4 which is discussed next.

6.3 Update of the crack geometry

If the propagation criterion (Eq. 6.2) is fulfilled at least at one crack-front node, the crack geometry is explicitly updated. Therefore, the SIFs are computed for each crack-front node based on the proposed procedure of Sec. 6.1. The corresponding energy release rates G_i, crack increment lengths Δr_i and propagation angles θ_c^i are determined with Eqs. 2.13, 6.3 and 6.4 which describe the movement of each crack-front node. It is noted that the movement is restricted to the $\boldsymbol{n}$-$\boldsymbol{t}$-plane, see Fig. 6.1. That is, the propagation direction is independent of mode III, however, the out-of-plane shear mode influences the crack increment length Δr_i or the critical pressure magnitude p_c (see Sec. 6.2.1) which

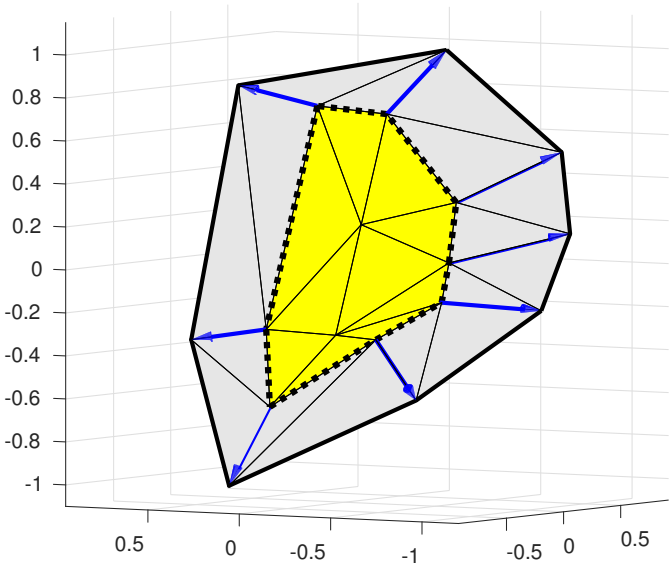

Figure 6.8: Update of the explicit crack geometry by adding new segments.

fulfills the applied propagation criterion.

In Fig. 6.8, the previous (initial) crack geometry is illustrated by the yellow triangles and the corresponding crack-front by the dashed line. The propagation of each crack-front node is shown by a blue arrow whose length varies depending on the current energy release rate G_i or the crack increment length Δr_i. The propagation of the crack surface is shown by the grey triangles which are added based on the new crack-front nodes, whose connection forms the new crack-front (bold black line).

6.4 Crack propagation algorithm

In this section, the required steps which are needed to simulate the crack propagation of a loaded crack with the XFEM are summarized. At first, the domain and the initial crack are defined and discretized, see Sec. 3. Then, a stress function or pressure distribution is defined on the explicit crack geometry Γ_h, see Sec. 5, based on coordinate systems or distances in the crack surface which were discussed in Sec. 4. For the XFEM approximation with a hybrid explicit-implicit crack description, three level set-functions $\phi_1(\boldsymbol{x})$, $\phi_2(\boldsymbol{x})$ and $\phi_3(\boldsymbol{x})$ are derived from the explicit crack representation whose zero-level sets implicitly define the crack geometry. All computations during a propagation step are based on this implicitly defined crack surface, wherefore the crack surface load is projected from the explicit crack geometry to the implicit one based on the procedure which was discussed in Sec. 5.4.1. Then, the boundary value problem is solved with the extended approximation of the displacement field (Eq. 3.21) due to the external loads $\boldsymbol{f}_{\text{ext}}$ and the internal

loads $\boldsymbol{f}_{\text{int}}$. Therefore, an initial magnitude p_0 of the internal load has to be defined. In a post-processing step, the corresponding SIFs and energy release rates are evaluated for both loading types based on a displacement fitting, see Sec. 6.1. Then, the critical internal loading magnitude p_c which fulfills the propagation criterion is determined based on the superposition principle of LEFM, see Sec. 6.2.1. For this critical loaded crack, the directions and lengths of the propagation are computed for all crack-front nodes. Finally, the crack geometry is updated as described in Sec. 6.3 and the simulation is continued with the next propagation step until the maximum number of iteration steps is reached. These steps are illustrated in a flow diagram in Fig. 6.9.

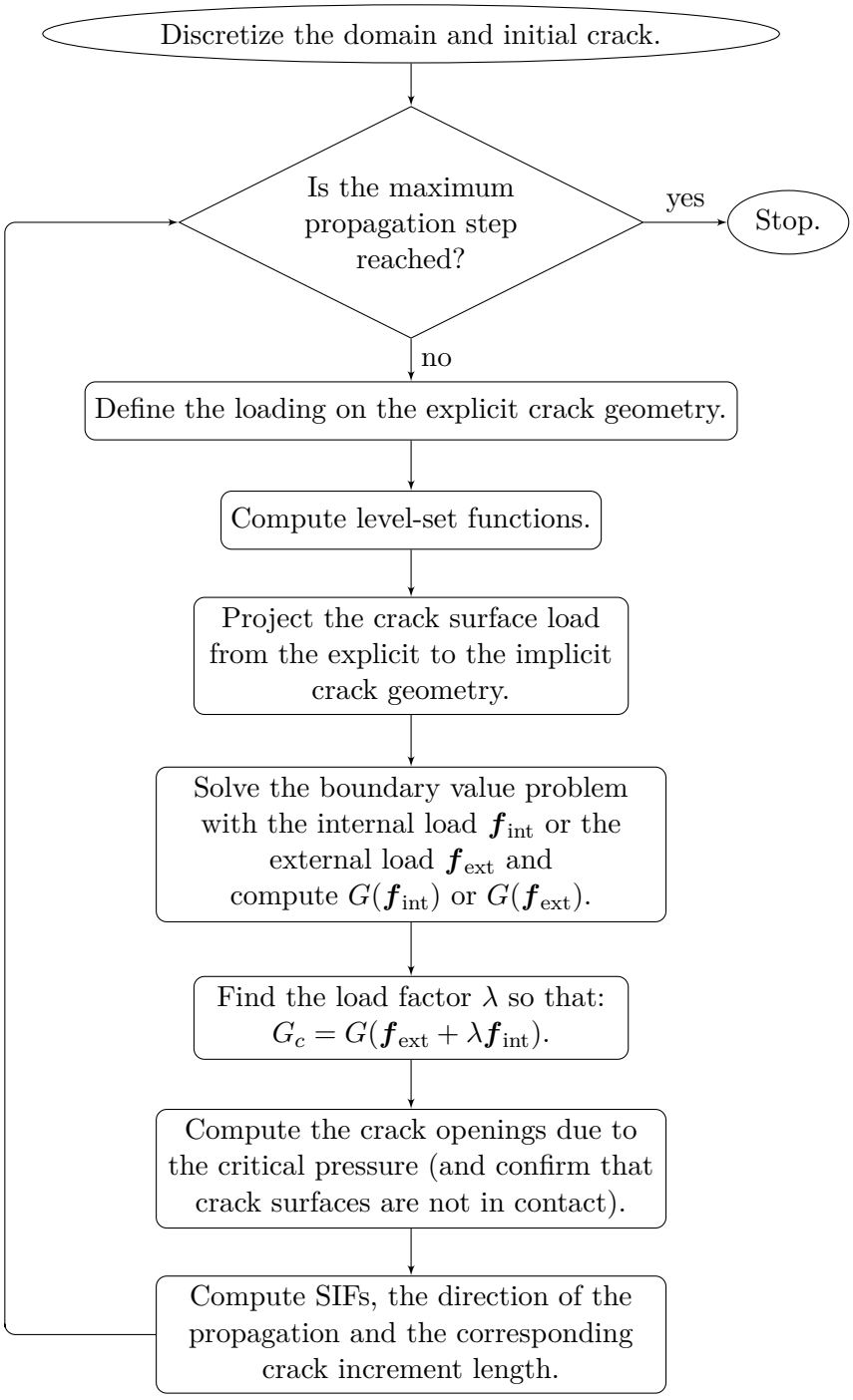

Figure 6.9: Crack propagation algorithm [164].

7 Numerical results

This section presents test cases with stress-free and loaded crack surfaces in two and three dimensions based on LEFM to verify and illustrate the performance of the proposed method. Achieved results are compared with analytical or empirical results when available. For all examples a brittle, isotropic and linearly elastic material is assumed with a Young's modulus $E = 37\,800\,\mathrm{MPa}$, a Poisson's ratio $\nu = 0.3$ and a critical energy release rate $G_c = 680\,{}^{\mathrm{J}}/_{\mathrm{m}^2}$. Furthermore, plane stress conditions are assumed in two dimensions. It is noted that the focus of this work is only the propagation of an arbitrarily, already existing mixed-mode loaded macro-fracture within an isotropic material with prescribed pressure distributions. No crack initiations, micro-fracture fields, dynamic effects, are considered. Instead, the obtained final crack paths or surfaces and their corresponding critical pressure magnitudes are presented. For all examples, the enriched nodes $J^\star$ are defined as the set of element nodes of elements where the minimum distance of at least one element node to the crack-tip/front is smaller than the pre-defined distance $r_{\mathrm{tip}} = 0.05 \cdot l_a$, with l_a being the characteristic crack length which was introduced in Sec. 6.1.4. A pseudo-time is used for the propagation to establish a connection of the critical pressure with time which is obtained based on the assumption of an impermeable material without fluid lag. Therefore, the injected fluid is equal to the crack volume, wherefore the time t can be expressed based on a surface integral over the crack surface Γ_h with

$$t = \frac{\int_{\Gamma_h} u_b d\Gamma_h}{Q_0}. \tag{7.1}$$

There, u_b are the CODs in direction of the local coordinate b of Sec. 3.1.3 and Q_0 is the injection rate of the fluid which is assumed with $1\,{}^{\mathrm{ml}}/_{\mathrm{sec}}$. Again, the HF examples are rather academic with focus on the presence of possibly complex loadings on the crack surfaces. The aim is to show the versatility and flexibility of the proposed numerical treatment which is also suited for other applications with loaded crack surfaces. All systems of equations are solved with the Parallel Sparse Direct Solver PARDISO [108, 165, 166].

7.1 Accuracy of the obtained SIFs

The first examples investigate the accuracy of the obtained SIFs which are evaluated based on the proposed displacement fitting which was discussed in Sec. 6.1. Therefore, static fractures with stress-free and loaded crack surfaces in two and three-dimensions are investigated and the obtained SIFs are compared with those available in the literature.

7.1.1 Eccentric three-point bending test

The first test case investigates an edge cracked three-point bending test with an eccentric load, where $F = 100\,\mathrm{kN}$ and the eccentricity $d = 75\,\mathrm{cm}$. The beam is 600 cm long (l) and 150 cm high (h) and exhibits an $l_c = 75\,\mathrm{cm}$ long initial crack in the middle, see Fig. 7.1(a). The expected SIFs are given by [64]

$$\begin{bmatrix} K_{\mathrm{I}} \\ \\ K_{\mathrm{II}} \end{bmatrix} = \begin{bmatrix} \frac{3Fl\sqrt{\pi l_c}}{h^2} \cdot \frac{F_{\mathrm{I}}^{'}}{\left(1-\frac{l_c}{h}\right)^{\frac{3}{2}}} \\ \\ \frac{3Fl\sqrt{\pi l_c}}{h^2} \cdot F_{\mathrm{II}} \end{bmatrix}. \tag{7.2}$$

With $F_{\mathrm{I}}^{'} = 0.4010$ and $F_{\mathrm{II}} = 0.0876$, Eq. 7.2 leads to: $K_{\mathrm{I}} = 69.64$ and $K_{\mathrm{II}} = 5.38$. A local refinement in the vicinity of the crack allows a limitation of the element number, see Fig. 7.1(b). Starting with a coarse mesh with 931 elements, SIFs are computed on seven different meshes which are generated by a refinement until a fine mesh with 48 511 elements is obtained. Fig. 7.1(c) shows the normalized results of the computed SIFs for mode I (red) and II (blue).

In this test case, the displacement fitting provides results within 2% for mode I on any of the meshes. The results of mode II are a little bit worse, however the achieved error is also limited to 12% on the coarse mesh and improves upon refinement.

7.1.2 Cantilever with an edge crack

A shear loaded edge cracked rectangular plate with stress-free crack surfaces is investigated next. The extent of the plate is given by: $h = 7\,\mathrm{m}$, $l = 16\,\mathrm{m}$ and exhibits an initial crack with a length $l_c = 3.5\,\mathrm{m}$, as shown in Fig. 7.2(a). The plate is clamped on the left side and loaded by a shear traction $\tau = 1\,\mathrm{GPa}$ at the opposite side as Fig. 7.2(a) shows. This configuration leads to a mixed-mode loading, where the SIFs are given, e.g., in [17] with $K_{\mathrm{I}} = 34$ and $K_{\mathrm{II}} = 4.55$. The SIFs are computed on seven different meshes. Starting with a coarse mesh (187 elements) which is locally refined at the crack, as illustrated in Fig. 7.2(b). This mesh is refined until 29 051 elements are obtained. The obtained results

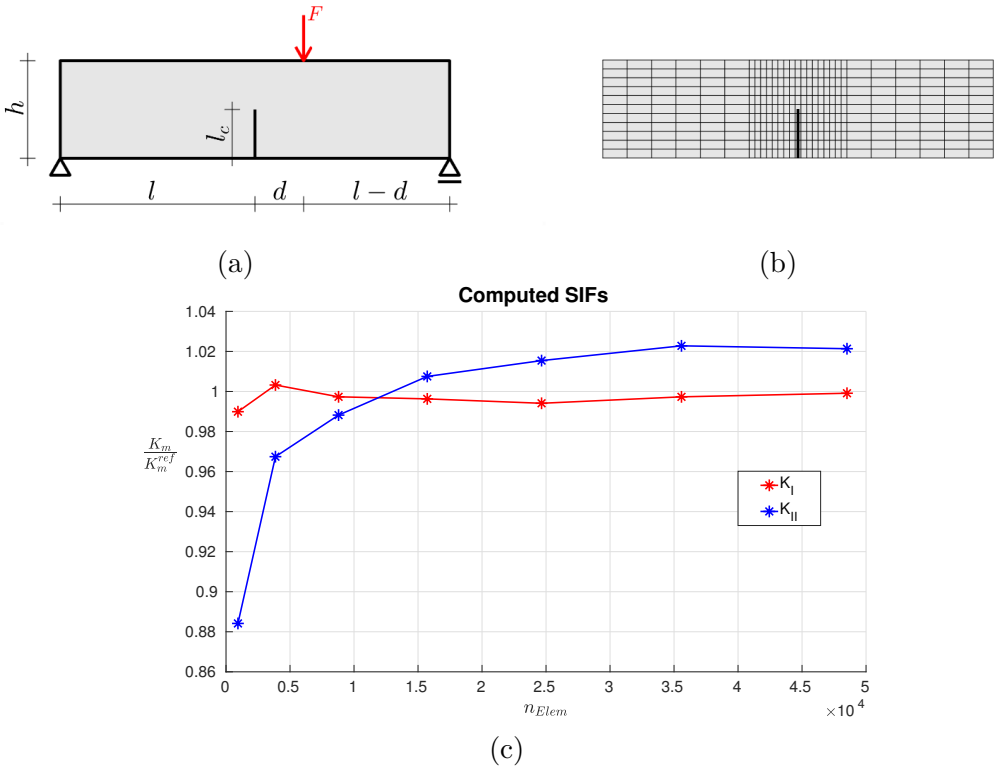

Figure 7.1: Eccentric three-point bending test in two dimensions (a) geometry parameters, (b) mesh and (c) results.

are illustrated in Fig. 7.2(c), where the red line represents the normalized mode I and the blue line the normalized mode II SIF. This test case also achieves good results, where the error of K_I is below 5% for all used meshes. Mode II has again less accurate results, but also converges upon refinement.

In these two externally loaded test cases with stress-free crack surfaces, most meshes provided mode I SIFs within an error of 2% and mode II SIFs within 5%. The next examples investigate loaded crack surfaces which would lead to issues in the 'classical' interaction integral (Eq. 2.20). A big advantage of the displacement fitting is that no modifications are necessary as the following examples show.

7.1.3 Loaded crack surfaces in rectangular plate with finite width

In this test case, the evaluation of SIFs due to different crack surface loadings is investigated within an edge cracked plate of finite width. The plate is 2 m wide and 4 m high and exhibits a 1 m long initial crack, see Fig. 7.3. The performance of the displacement fitting procedure is examined based on different mesh refinements, see Fig. 7.3(c) for an example mesh. Dirichlet boundary conditions are prescribed at the top and bottom nodes of the right side. The crack surface is loaded by a combination of shear and normal stresses

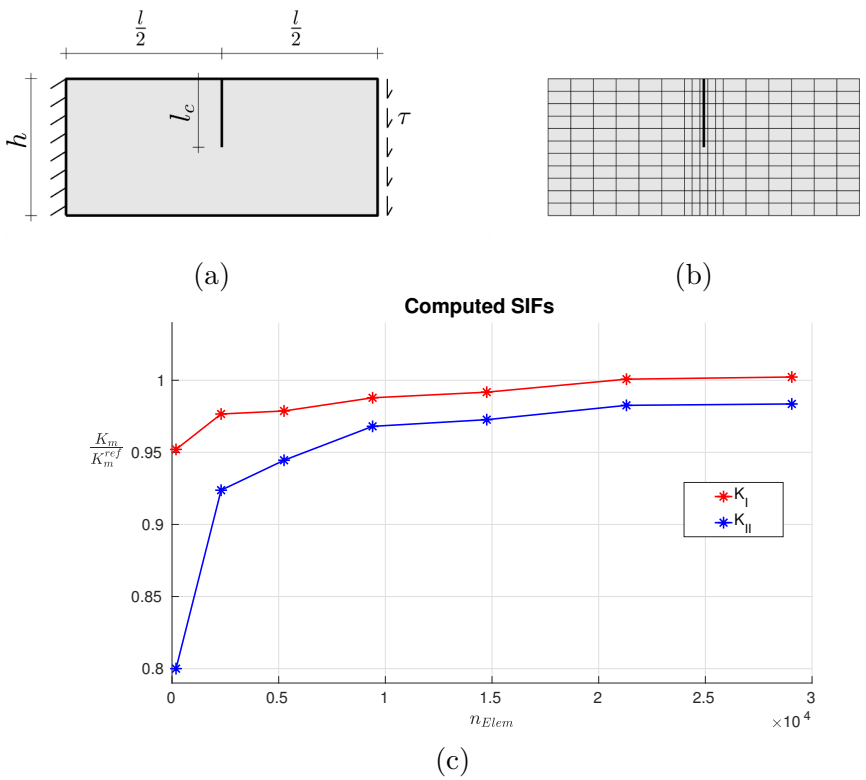

Figure 7.2: Edge cracked cantilever (a) geometry parameters, (b) mesh, and (c) results.

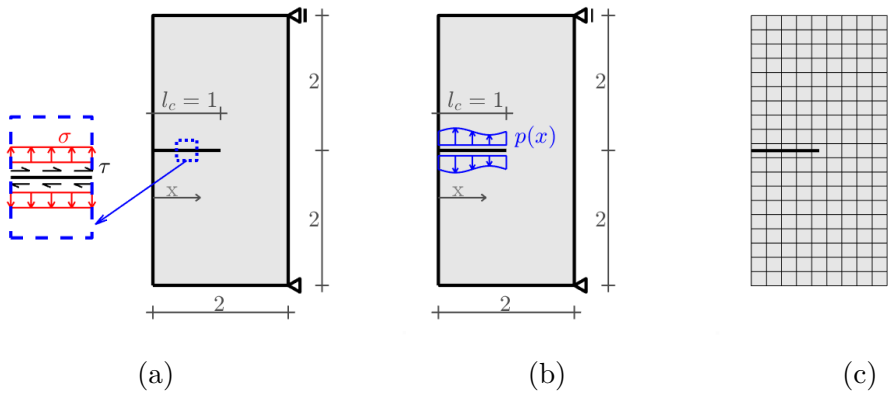

Figure 7.3: Edge crack in two dimensions which is loaded with (a) a shear-pressure load and with (b) different pressure distributions. (c) Mesh.

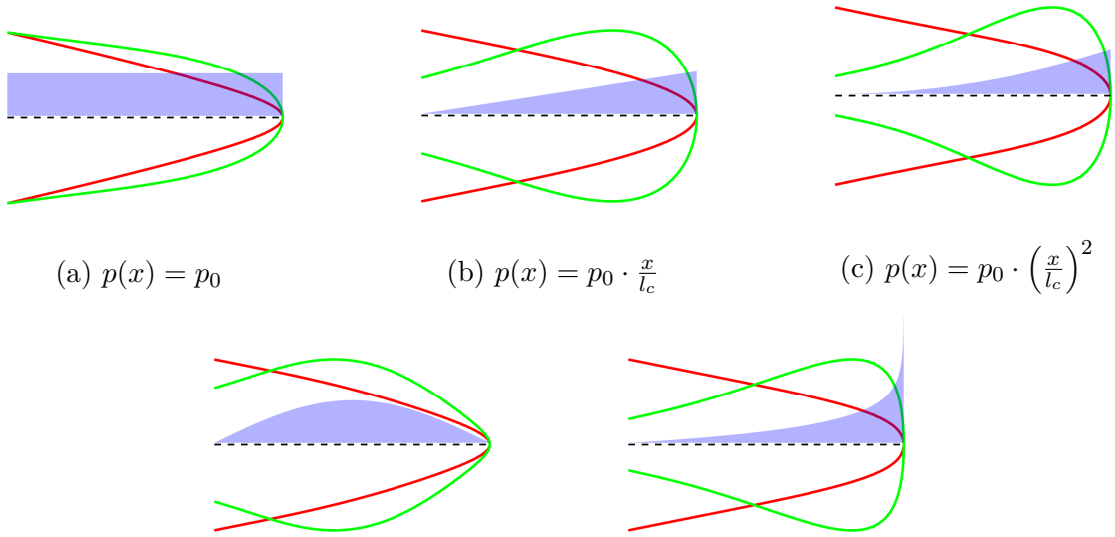

(a) $p(x) = p_0$ (b) $p(x) = p_0 \cdot \frac{x}{l_c}$ (c) $p(x) = p_0 \cdot \left(\frac{x}{l_c}\right)^2$

(d) $p(x) = p_0 \cdot \sin(x\pi)$ (e) $p(x) = -p_0 \cdot \ln(l_c - x)$

Figure 7.4: Applied pressure distributions and their corresponding crack openings.

(LC-1, see Fig. 7.3(a)) or by five different pressure distributions $p(x)$

$$p(x) = \begin{cases} p_0 & \text{LC-2} \\ p_0 \cdot \frac{x}{l_c} & \text{LC-3} \\ p_0 \cdot \left(\frac{x}{l_c}\right)^2 & \text{LC-4} \\ p_0 \cdot \sin(x\pi) & \text{LC-5} \\ -p_0 \cdot \ln(l_c - x) & \text{LC-6} \end{cases} \tag{7.3}$$

which is illustrated in Fig. 7.3(b), respectively. A graphical illustration of the different pressure distributions and their corresponding crack openings are shown in Fig. 7.4. Herein, the red lines represent the openings which are obtained from the configuration shown in Fig. 7.3(b). The green lines are the openings of the same configuration, however, with fixed displacements on the top and bottom of the plate. Analytical mode I SIFs are given for all cases in [77, 109] with

$$K_I = \int_0^a p(x) m(x, a) dx, \tag{7.4}$$

where a is the crack length, $p(x)$ the pressure applied within the fracture, and $m(x, a)$ the weight function. For these examples, an initial pressure magnitude p_0 of 1 MPa is

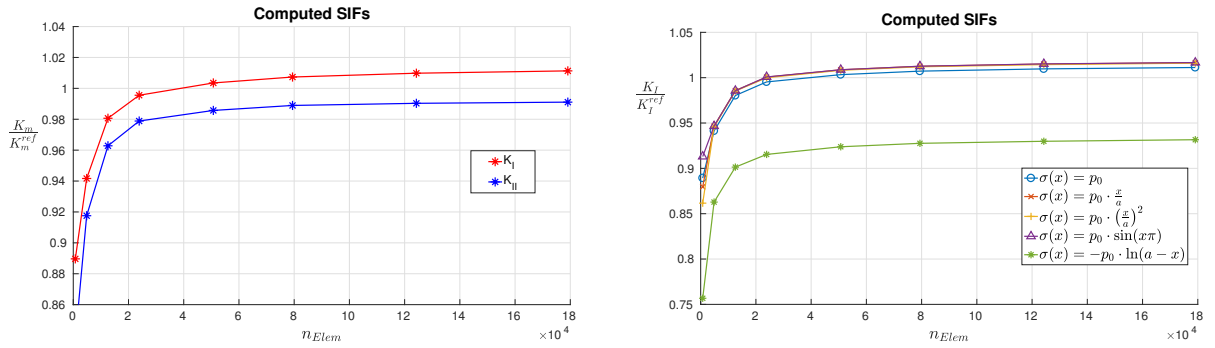

(a) (b)

Figure 7.5: Normalized SIFs due to (a) a shear-pressure load, see Fig. 7.3(a), and due to (b) different pressure distributions, see Fig. 7.3(b).

assumed which leads to following expected mode I SIFs:

LC-1	**LC-2**	**LC-3**	**LC-4**	**LC-5**	**LC-6**
4.960	4.960	2.294	1.505	3.008	5.075

Table 7.1: Reference mode I SIFs for the different crack surface loadings.

The expected mode II SIF of LC-1 is given in [88] with

$$K_{\mathrm{II}} = \tau \sqrt{\frac{\pi l_c}{1 - \frac{l_c}{h}}} \left(1.122 - 0.561 \frac{l_c}{h} + 0.085 \frac{l_c^2}{h^2} + 0.180 \frac{l_c^3}{h^3}\right) = 2.219\,. \tag{7.5}$$

Fig. 7.5 shows the achieved results where the normalized SIFs are plotted over the used number of elements. It can be seen that the errors of the computed SIFs are for the finite pressure distributions in the same range as in the previous examples with stress-free crack surfaces. The singular pressure distribution (LC-6) leads to little bit worse results. This can be explained by the fact that singular pressure values are applied at a location where also singular stress and strain fields are present.

7.1.4 Mixed-mode pressurized crack under compression

In this example, the accuracy of the computed critical pressure magnitudes is investigated based on a 3 m long pressurized crack in a domain subjected to far field compressive bi-axial tractions $\sigma_x = 10\,\mathrm{MPa}$ and $\sigma_y = 7\,\mathrm{MPa}$, see Fig. 7.6. The crack is oriented at an angle α with respect to the direction of horizontal traction σ_x. A structured background-mesh consisting of bilinear quadrilateral elements is used to describe a $10\,\mathrm{m} \cdot 10\,\mathrm{m}$ domain. Critical pressure magnitudes according to a constant prescribed pressure distribution are

evaluated for different orientations of the initial crack based on different mesh refinements. The computed magnitudes are compared with reference solutions which are based on Eq. 2.13. The resulting SIFs of a two-dimensional infinite domain are given by [86, 151]

$$K_I = \sqrt{\pi l_a}\left[p - \left(\sigma_x \sin^2\alpha + \sigma_y \cos^2\alpha\right)\right] \tag{7.6}$$

$$K_{II} = 0.5\sqrt{\pi l_a}\left[\sigma_x - \sigma_y\right]\sin 2\alpha$$

where l_a is the half crack length, α is the orientation of the crack and p is the pressure magnitude of a constant internal pressure. Achieved results are shown in Fig. 7.6(c) where the ratios of the computed and analytical critical pressure magnitudes are plotted over the used number of elements.

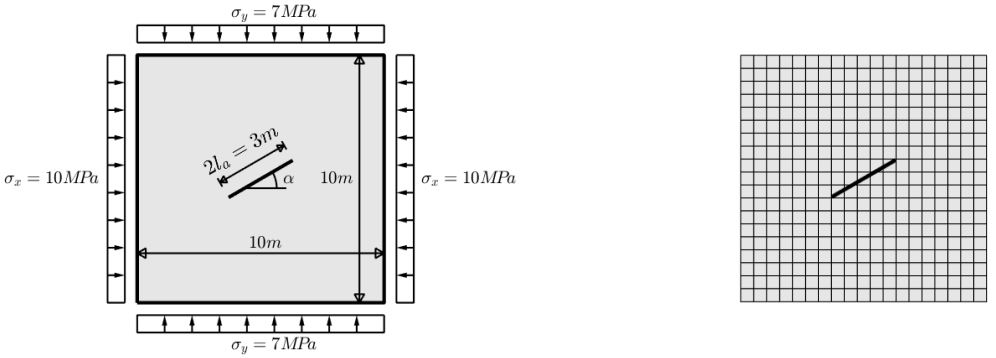

(a) (b)

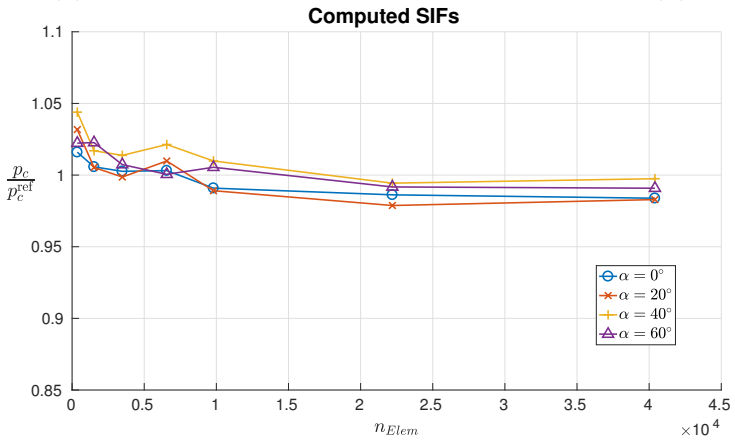

(c)

Figure 7.6: Mixed-mode pressurized crack under compression: (a) dimensions and loading, (b) mesh, and (c) results.

The numerical results are in good agreement with those available in the literature, where most of the meshes achieve pressure magnitudes with an error of less than 3%. In

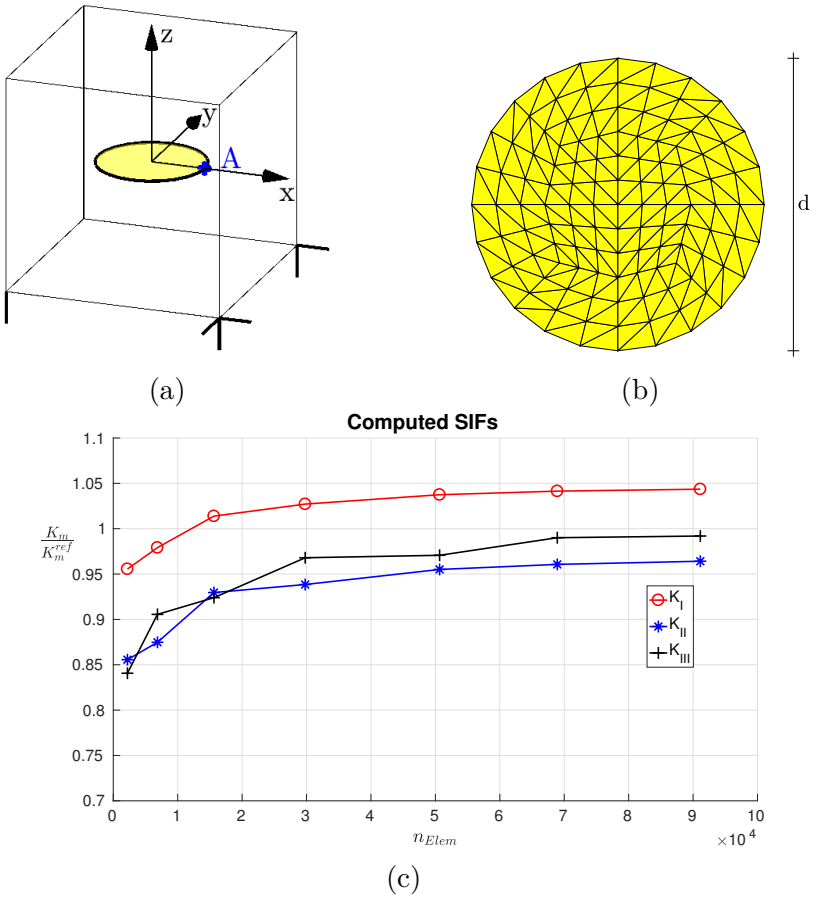

Figure 7.7: Penny-shaped crack with loaded crack surfaces: (a) system, (b) crack surface, and (c) results.

addition, these solutions also show a mesh independency as the same background mesh is used for all orientations of the crack and no significant deviations are observed.

7.1.5 Penny-shaped crack with loaded crack surfaces

The last static test case deals with a penny-shaped crack which is embedded in the three-dimensional space and is loaded by applied tension and shear tractions at the crack surface. The crack has a diameter $d = 2\,\mathrm{m}$ and is explicitly described by 216 flat triangles and the crack-front by 24 line segments as shown in Fig. 7.7(b). The crack is located within a cube-like domain with a side length of 4 m. Displacements are prescribed to zero at some corner nodes on the bottom. An illustration of the situation is presented in Fig. 7.7(a). The individual components of the loading are given in the global coordinate system by $\sigma = 1\,\mathrm{MPa}$ and $\tau_x = \tau_y = \frac{1}{\sqrt{2}}\,\mathrm{MPa}$, see Fig. 7.7(a). For this test case, seven different meshes with trilinear hexahedral elements are used. The number of elements along an edge varies between 13 and 45.

In this general example, SIFs vary along the crack-front. The expected SIFs for the whole front are given by [88]

$$\begin{bmatrix} K_{\mathrm{I}} \\ K_{\mathrm{II}} \\ K_{\mathrm{III}} \end{bmatrix} = \begin{bmatrix} \frac{2}{\pi}\sigma\sqrt{\pi\frac{d}{2}} \\ \frac{4}{\pi(2-\nu)}\left(\tau\cos\omega\right)\sqrt{\pi\frac{d}{2}} \\ \frac{4(1-\nu)}{\pi(2-\nu)}\left(\tau\sin\omega\right)\sqrt{\pi\frac{d}{2}} \end{bmatrix}, \tag{7.7}$$

where ω describes the angle between the direction of the resultant shear traction and the reviewed point. In this example, the accuracy of the obtained SIFs is investigated based on a point A which is located at an angle $\omega = \frac{\pi}{4}$, see Fig. 7.7(a). For this point, all three modes are present which are given based on Eq. 7.7 as follows: $K_{\mathrm{I}} = 1.128$, $K_{\mathrm{II}} = 0.939$ and $K_{\mathrm{III}} = 0.657$. The obtained results are presented in Fig. 7.7(c).

The result shows that with only 25^3 elements, SIFs can be computed with an error of less than 10% and 37^3 elements lead to results below 5%. That is, SIFs are well obtained for a three-dimensional crack configuration with stresses on the crack surface without any modifications.

7.2 Crack propagation in two dimensions

In this section, the propagation of two-dimensional cracks due to different loads is investigated. In particular, the first example investigates the propagation of a mixed-mode loaded edge crack with stress-free crack surfaces which is embedded in a square specimen and is loaded by prescribed displacements on the upper and lower boundary. The other examples deal with loaded crack surfaces where either the influence of the external loads (far field tractions) or the influence of different pressure distributions within the fracture are investigated. For the last example, the simplified fluid model which was introduced in Sec. 5.3 is used.

7.2.1 Edge crack under tension and shear

In this test case, the propagation of a mixed-mode loaded edge crack in a square specimen with the extent $l = 1\,\mathrm{m}$ is investigated. The initial crack with a length of $l_c = 0.5\,\mathrm{m}$ is loaded through prescribed displacements $u_D = 1\,\mathrm{mm}$ on the upper and lower side of the domain in direction of the specified angle α, as illustrated in Fig. 7.8(a). These boundary conditions produce an opening of the crack, wherefore no other loadings are needed. The domain is discretized by a structured mesh which consists of 101×101 bilinear quadrilat-

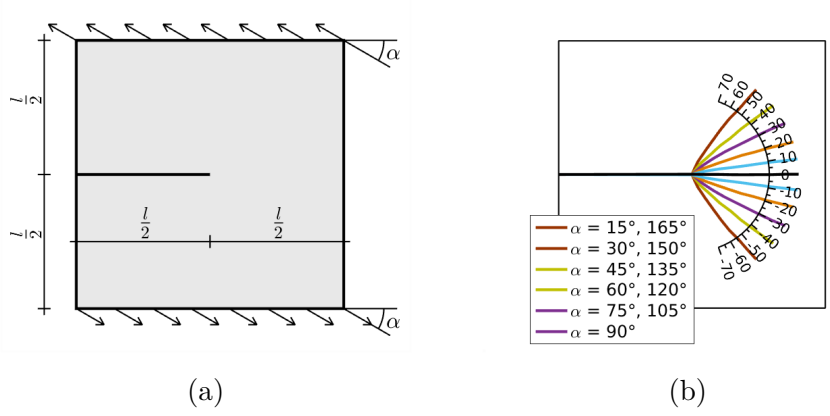

(a) (b)

Figure 7.8: Edge crack in a squared plate (a) geometry parameters and supports and (b) results of the crack propagation.

eral elements. It is noted that the focus of this example is the evaluation of the resulting crack paths due to different directions of the prescribed boundary conditions. Therefore, it is assumed that the crack propagates ten times in the direction of the maximum circumferential stresses with a maximum crack increment length of $da = 5\,\text{cm}$, independently, whether the propagation criterion G_c is fulfilled or not. The prescribed direction of the boundary conditions is varied from $15° \leq \alpha \leq 165°$ and the corresponding results are presented in Fig. 7.8(b). As expected, for $\alpha = 90°$ the crack propagates horizontally as for a pure tension loading where only mode I is relevant. The greater the boundary conditions deviate from a pure tension loading, the more dominant the impact of mode II is. The obtained crack paths for the different α are in good agreement to [28].

7.2.2 Propagation of a mixed-mode pressurized crack under compression

In this section, the crack configuration of Sec. 7.1.4 is used to investigate the influences of different far field tractions onto the resulting crack paths and the corresponding magnitudes of the fluid pressure which are required to fulfill the propagation criterion $G_i \leq G_c$ with $G_c = 680\,\text{J/m}^2$. A similar setting is investigated in the works of Dong [54] and Gupta [86]. The crack is oriented at an angle $\alpha = 40\,°$ with respect to the horizontal traction σ_x, see Fig. 7.6(a). In this test case, 10 time-steps are considered where the maximum crack increment da is set to 3 cm. The domain is described with 69×69 bilinear quadrilateral elements.

7.2.2.1 Constant far field tractions

The influence of different ratios of vertical (σ_y) and horizontal (σ_x) tractions onto the resulting crack paths and the corresponding magnitudes of the critical fluid pressure due

	LC-1	LC-2	LC-3	LC-4	LC-5
σ_x	2.0	1.75	1.5	1.25	1.0
σ_y	1.0	1.25	1.5	1.75	2.0

Table 7.2: Variations of the constant far field tractions.

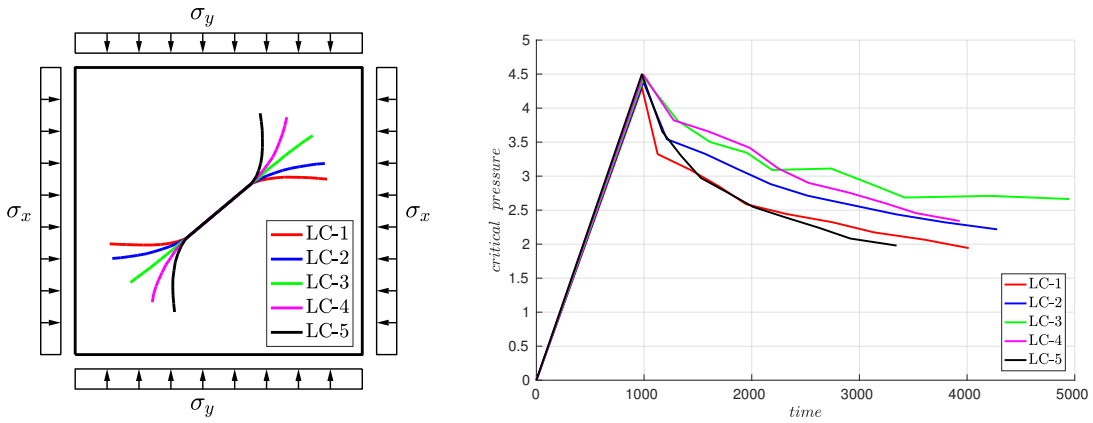

(a) (b)

Figure 7.9: Rotated pressurized crack loaded by constant far field tractions. (a) Resulting crack paths and (b) corresponding pressure magnitudes.

to constant far field tractions is investigated next. Therefore, 5 different loading cases are considered which are summarized in Tab. 7.2. The resulting crack paths are illustrated in Fig. 7.9(a) and the corresponding pressure magnitudes are illustrated in Fig. 7.9(b). It can be observed that the crack propagates in direction of the maximum load but it should be noted that this is just the case when the magnitudes of external loads and the required pressure are similar. When the internal pressure dominates the propagation, *quasi* straight crack extensions are expected as internal loads mainly lead to a mode I behaviour. An almost straight propagation is achieved where the horizontal and vertical tractions are equal as this behaviour presents a hydrostatic pressure. The behaviour of the pressure is for all load cases as expected, where a high pressure is required at the beginning of the propagation which decreases during the propagation.

7.2.2.2 Variable far field tractions

The example of Sec. 7.2.2.1 is also used for linearly changed far field tractions, see Fig. 7.10(a). This far field behaviour leads to different loaded crack-tips as the internal pressure is still prescribed as constant over the whole crack. Different gradients of the horizontal tractions σ_x are investigated. Therefore, 5 loading cases are defined in Tab. 7.3

	LC-1	LC-2	LC-3	LC-4	LC-5
$\sigma_{x,o}$	2.9	2.5	2.0	1.5	1.0
$\sigma_{x,u}$	3.1	3.5	4.0	4.5	5.0

Table 7.3: Variations of the linear far field tractions.

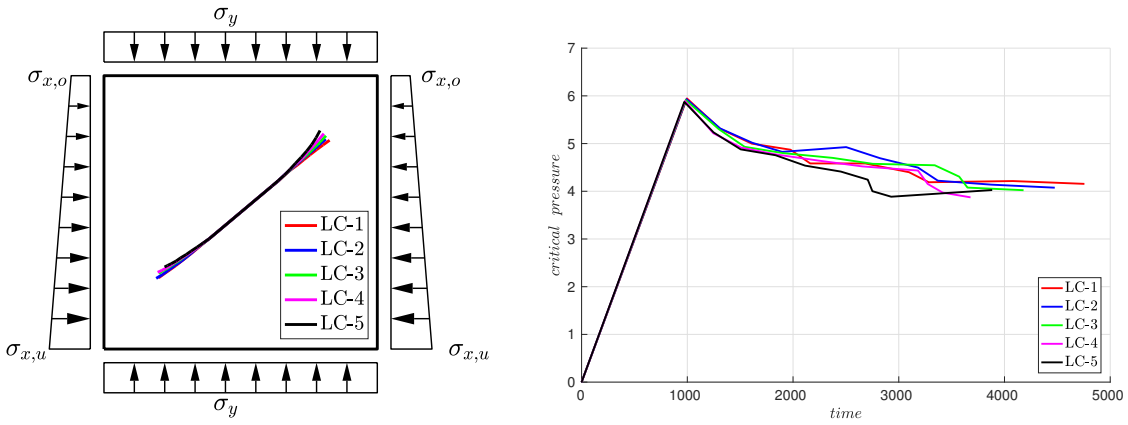

(a) (b)

Figure 7.10: Rotated pressurized crack loaded by linear far field tractions. (a) Resulting crack paths and (b) corresponding pressure magnitudes.

based on $\sigma_{x,o}$ and $\sigma_{x,u}$ which represent the upper and lower pressure magnitude of the horizontal tractions, see Fig. 7.10(a). The vertical traction σ_y is kept constant by a value of 3 MPa. The resulting crack paths are illustrated in Fig. 7.10(a) and the corresponding pressure magnitudes are illustrated in Fig. 7.10(b).

It can be observed that in this case the internal pressure dominates the propagation as the crack extension is almost straight. However, the propagation of the upper crack-tip slightly tilts to the vertical direction whereas the lower one slightly tilts to the horizontal direction. This can be explained by the fact that the horizontal traction is at the lower crack-tip higher than the vertical traction whereas the behaviour is opposite at the upper crack-tip. It should be noted that our model does not (yet) consider contact of the crack faces so that the internal pressure should dominate the external loading throughout the simulation.

7.2.3 Propagation based on the simplified fluid model

In the last two-dimensional example, the propagation of a curved crack due to the simplified fluid model of HF (Sec. 5.3) is investigated. The crack is located in a $10\,\mathrm{m} \cdot 10\,\mathrm{m}$ square specimen which is discretized with 69×69 bilinear quadrilateral elements. The

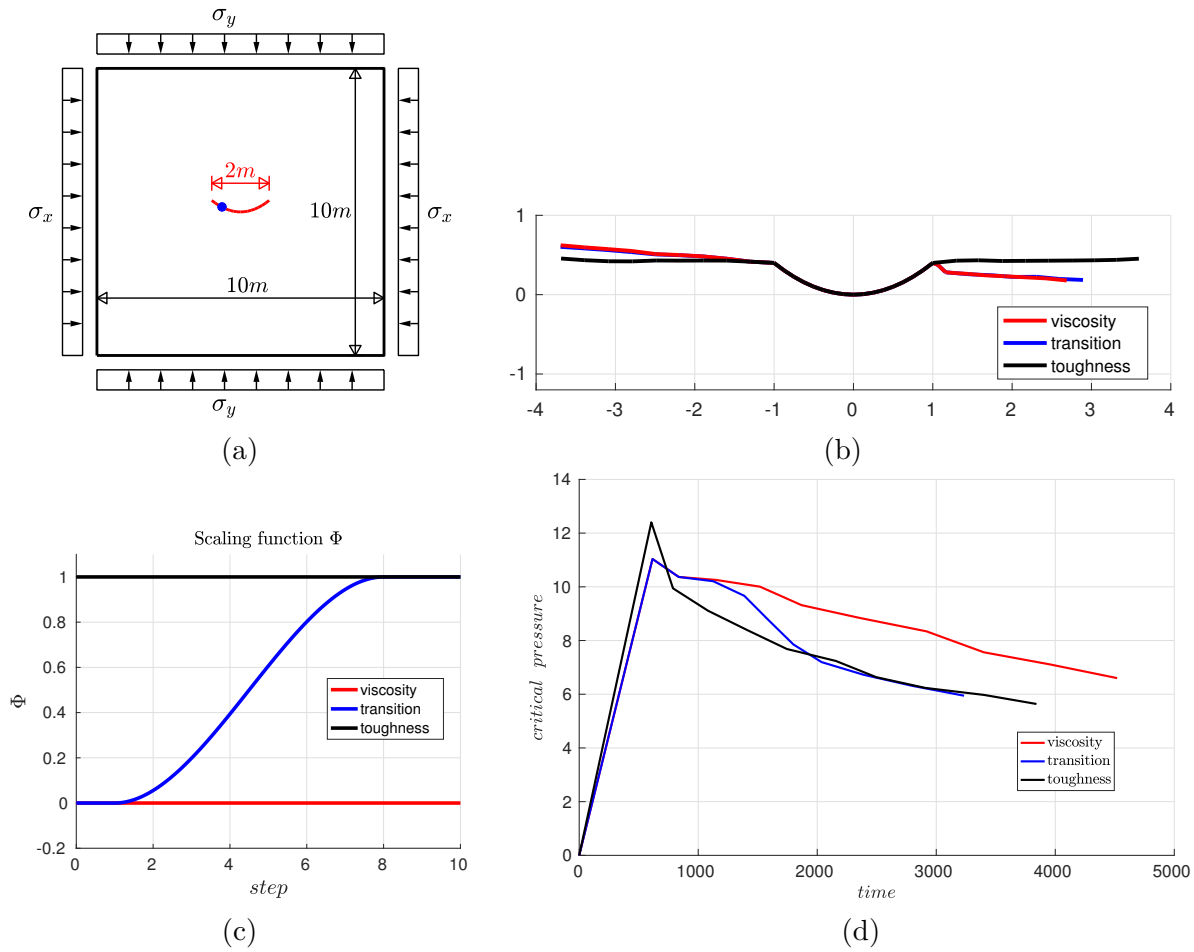

Figure 7.11: Curved two-dimensional crack under compression which is additionally loaded by the simplified fluid model. (a) Configuration, (b) resulting crack paths, (c) corresponding scaling function, and (d) corresponding critical pressures.

domain is subjected to constant far field tractions $\sigma_x = \sigma_y = 1\,\text{MPa}$, see Fig. 7.11(a). Additionally, a fluid pressure is applied within the fracture which is obtained from the simplified fluid model based on Eq. 5.8 and the investigated scaling functions which are illustrated in Fig. 7.11(c). Here, the red or black scaling function represents a pure viscosity-dominated or toughness-dominated propagation. In contrast, the blue scaling function describes an arbitrarily transition from the viscosity-dominated propagation to the toughness-dominated propagation. The injection point is arranged eccentrically on the left side which is illustrated in Fig. 7.11(a) by the blue point. The resulting crack paths are illustrated in Fig. 7.11(b) and the corresponding pressure magnitudes are illustrated in Fig. 7.11(d).

It can be seen that the eccentrically arranged injection point leads to unsymmetrical crack paths for the viscosity-dominated propagation and the transition case due to

the unsymmetrical location of the resultant force of the fluid pressure. In contrast, the crack propagates almost symmetrical for the toughness-dominated propagation due to the corresponding constant pressure distribution which is independent of the location of the injection point. In Fig. 7.11(d), it can be seen that at the beginning the required pressure of the transition case agrees with the required pressure of the viscosity-dominated propagation and then converges towards the toughness dominated solution which complies with the prescribed scaling function. The behaviour of the pressure is as expected where a high pressure is required at the beginning of the propagation which decreases during the propagation.

7.3 Crack propagation in three dimensions

The last examples investigate the propagation of two-dimensional crack surfaces which are embedded in three dimensions due to different loads. The first example deals with the propagation of an initially planar penny-shaped crack which is internally loaded by a constant pressure distribution. Herein, the accuracy of the obtained pressure magnitudes and the influence of different far field tractions are investigated. A more general framework is investigated in the last example. There, an arbitrarily curved crack surface is loaded by pressures which are obtained from the simplified fluid model.

7.3.1 Penny-shaped crack

In this section, the propagation of an initially planar penny-shaped due to different loadings is investigated. The cube-like domain which surrounds the embedded fracture is discretized with $39 \times 39 \times 39$ trilinear hexahedral elements. Herein, the dimension of each edge of the domain is 2 m and the radius r of the initial crack is set to $r = 30\,\text{cm}$. The fracture is described with 96 flat triangles in which 16 edges represent the crack-front, see Fig. 7.12. Two different configurations are considered in the following.

7.3.1.1 Pressurized penny-shaped crack within an infinite domain

This three-dimensional example, is motivated by a horizontal penny-shaped crack within an infinite domain which is pressurized with a constant fluid pressure p. Herein, the development of the pressure during time is observed and the obtained results are compared with a reference solution which is given, e.g., in [27, 86]. There, the critical crack radius r_c at a certain time t is given as

$$r_c = \left[\frac{9 Q_0^2 t^2 E'}{64\pi G_c}\right]^{1/5} \tag{7.8}$$

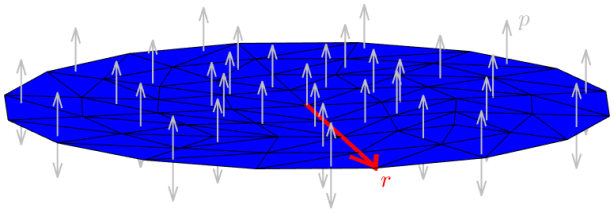

(a)

Figure 7.12: Pressurized penny-shaped crack.

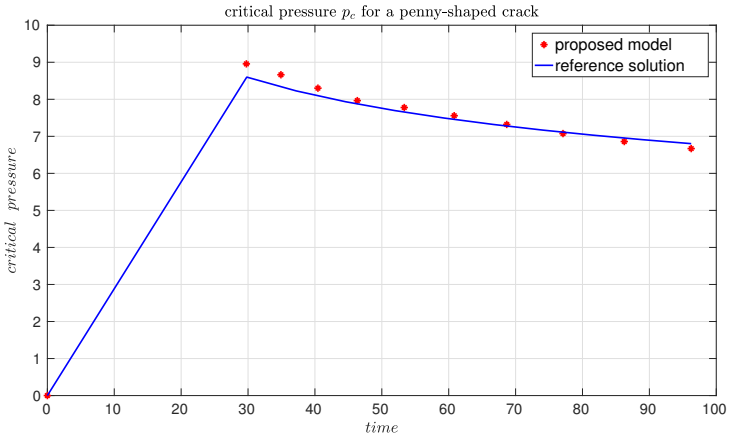

(a)

Figure 7.13: Critical pressure for a penny-shaped crack.

where Q_0 is the fluid injection rate, E' the plane-strain elastic modulus and G_c the critical energy release rate. The corresponding critical pressure is given with

$$p_c = \left[\frac{\pi G_c E'}{4 r_c}\right]^{1/2}. \tag{7.9}$$

For the simulation of the propagation 10 time-steps are considered where it is assumed that the crack propagates with a maximum increment length of $da = 2\,\mathrm{cm}$. Results are shown in Fig. 7.13 for a quasi static propagation simulation.

In the reference solution it can be seen that when the fluid is injected into the fracture the pressure begins to rise linearly until a critical value is reached. During this time the fluid fills and opens the fracture. After a critical value, a propagation starts and the pressure decreases which is in good agreement with our numerical results.

7.3.1.2 Mixed-mode loaded penny shaped crack

This example is an extension of the two-dimensional example presented in Sec. 7.2.2.1 where the influences of the external loads on the resulting crack surfaces of an initial

	LC-1	**LC-2**	**LC-3**	**LC-4**	**LC-5**
σ_z	5.0	4.0	3.0	2.0	1.0
$\sigma_x = \sigma_y$	1.0	2.0	3.0	4.0	5.0

Table 7.4: Variations of the globally applied far field tractions.

penny-shaped crack are investigated. Therefore, 5 different loading cases of the globally applied far field tractions (σ_x,σ_y,σ_z) are considered which are summarized in Tab. 7.4. The discretization of the domain and the penny-shaped crack is the same as in Sec. 7.3.1.1. However, here the fracture is rotated by 40° about the y-axis, see Fig. 7.14(a).

In this test case, 10 time-steps are considered where the maximum crack increment da is set to 5 cm. The resulting crack surfaces are shown in Fig. 7.14(b-f) for the different far field tractions and their corresponding pressure magnitudes are illustrated in Fig. 7.14(g).

The final crack surfaces and pressure distributions are in good agreement with those of the two-dimensional case which are shown and discussed in Sec. 7.2.2.1. Therefore, the same conclusions apply analogously to this example.

7.3.2 Propagation based on the simplified fluid model

In this last example, the propagation of an arbitrarily curved crack surface due to the simplified fluid model of HF (Sec. 5.3) is investigated. The crack is located in a $2\,\mathrm{m} \cdot 2\,\mathrm{m} \cdot 2\,\mathrm{m}$ cube-like specimen which is discretized with $39 \times 39 \times 39$ trilinear hexahedral elements. The domain is subjected to constant far field tractions $\sigma_x = \sigma_y = \sigma_z = 1\,\mathrm{MPa}$, see Fig. 7.15(a). Additionally, a fluid pressure is applied within the fracture which is obtained from the simplified fluid model based on Eq. 5.8 and the investigated scaling functions which are illustrated in Fig. 7.15(c). Here, the red or black scaling function represents a pure viscosity-dominated or toughness-dominated propagation. In contrast, the blue scaling function describes an arbitrarily transition from the viscosity-dominated propagation to the toughness-dominated propagation. The injection point is arranged almost in the center of the crack geometry as illustrated in Fig. 7.15(b) by the red point. The propagation is simulated with 5 time-steps and a maximum crack increment $da = 10\,\mathrm{cm}$. The resulting crack surfaces are illustrated in Figs. 7.15(d-f) and their corresponding pressure magnitudes are illustrated in Fig. 7.15(g).

It can be seen that the resulting crack surfaces due to the three scaling functions are quite similar which can be explained by the fact that the injection point is arranged almost in the center of the surface, wherefore the influence of the applied pressure distribution

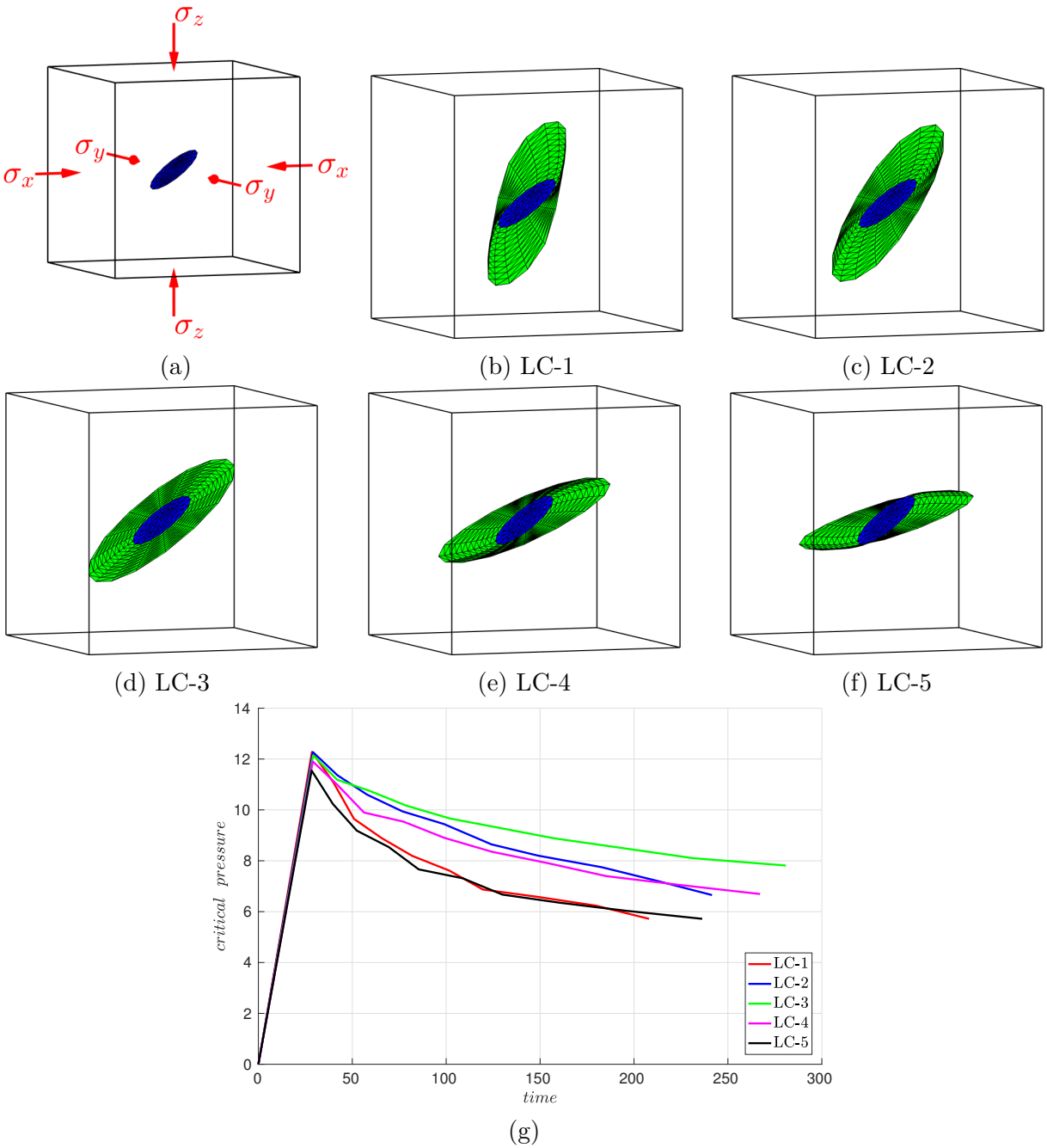

(a) (b) LC-1 (c) LC-2

(d) LC-3 (e) LC-4 (f) LC-5

(g)

Figure 7.14: Planar penny-shaped crack under compression with different far field tractions. (a) Configuration, (b-f) final crack surfaces, and (g) corresponding critical pressure magnitudes.

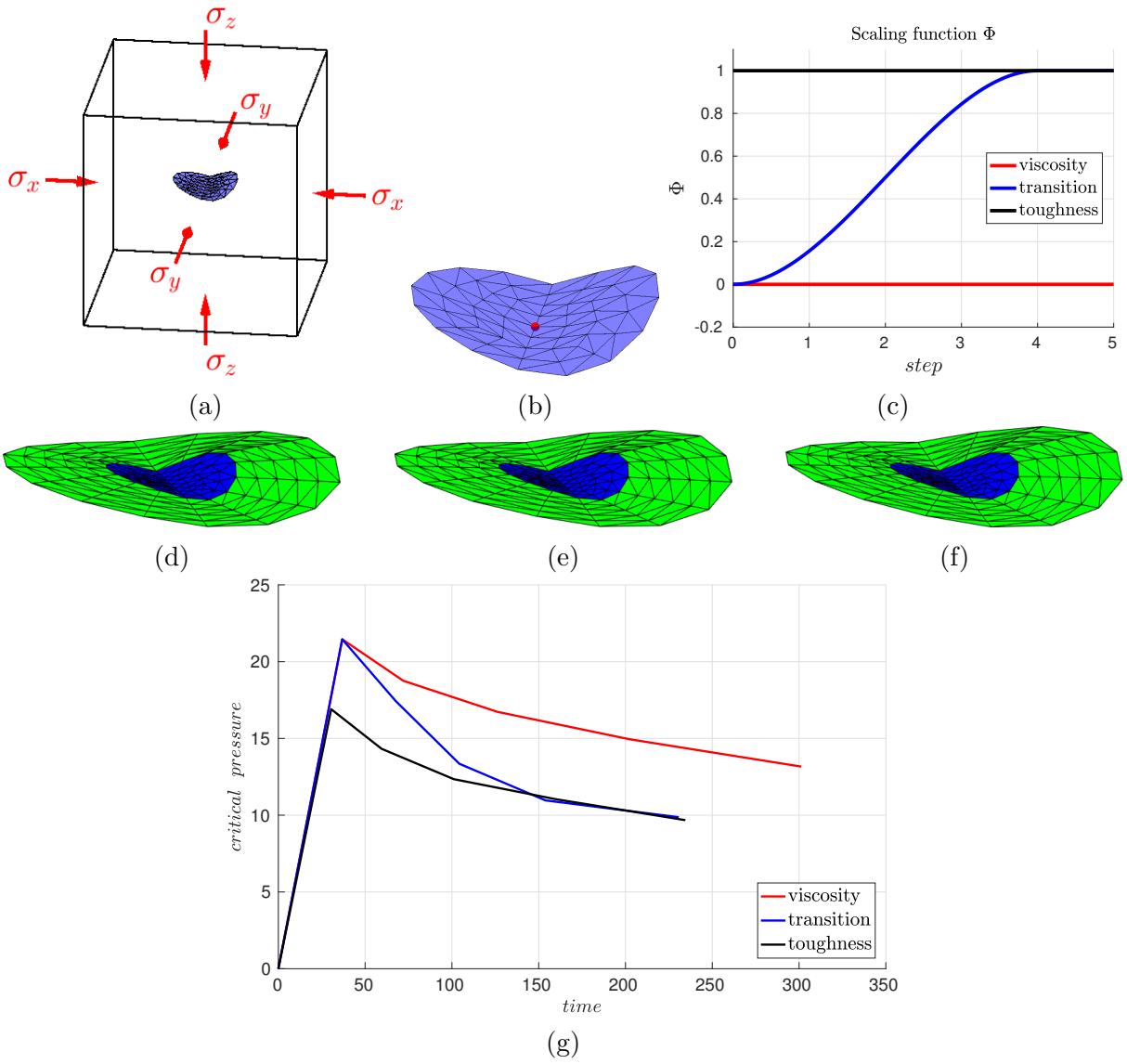

Figure 7.15: Arbitrarily curved three-dimensional crack under compression which is additionally loaded by the simplified fluid model. (a) Configuration, (b) initial crack geometry, and (c) applied scaling functions. The resulting crack surfaces due to the (a) viscosity-dominated propagation, the (b) transition case, and the (d) toughness dominated propagation. (d) Corresponding critical pressure magnitudes.

on the resulting crack geometry is less. However, Fig. 7.15(g) shows that the required pressure magnitudes strongly depend on the pressure distribution. At the beginning of the propagation, the required pressure of the transition case follows the viscosity-dominated propagation and converges towards the toughness-dominated solution which complies again with the prescribed scaling functions. The behaviour of the pressure is as expected where a high pressure is required at the beginning of the propagation which decreases during the propagation.

8 Conclusion

A numerical framework is presented which considers crack propagation induced by loaded crack surfaces which is relevant in a number of applications. Among the most important ones is hydraulic fracturing (HF), wherefore this thesis links to that context frequently and discusses concrete examples how to generate complex and meaningful pressure fields. The XFEM with a hybrid explicit-implicit crack description is used for the accurate approximation of displacement quantities in the cracked domain. The method is significantly improved for a more accurate representation of the crack front and the associated coordinate systems.

Coordinate systems and distances are introduced in explicitly defined crack surfaces which provide a useful path to define different stresses and loadings on the crack surface. In the context of HF, a simplified fluid model is presented based on: (i) known pressure distributions, (ii) a scaling function, and (iii) dimensionless virtual distances which are obtained by solving a Laplace-Beltrami problem on the surface mesh. Due to the fact that the explicitly defined crack geometry may not coincide exactly with the implicit crack geometry, a data transfer between these two descriptions is required. Therefore, integration points must be placed properly on the zero-level set of the implicit description. Then, closest point projections are employed to extract data from the explicit description.

A crack propagation model is developed where internal and external loadings are distinguished. The computation of a load factor for the internal loading on the crack surface while keeping the external loading constant is outlined. Finally, the computation of SIFs based on CODs is described in the context of implicit crack descriptions in the XFEM. The resulting model and numerical approach are simple and versatile and numerical results show the success of the approach.

In conclusion, the proposed framework provides a simple, robust and numerically efficient procedure to deal with arbitrarily curved and loaded crack surfaces. However, there are some challenges left in the context of crack propagation with the XFEM and a hybrid explicit-implicit crack description which could be addressed in future works to further expand the potential field of applications. Issues occur, e.g., in edge-cracked dams where cracks propagate along curved boundaries of the domain. Therefore, additional procedures have to be provided which ensure, e.g., that the propagated crack-front stays within the domain or is physically extended to the boundary. Other extensions of the

proposed framework can be done, e.g., in the context of: cohesive crack models, contact models, interaction of multiple cracks, interface cracks, different material models etc.

Bibliography

[1] Abe, H., Keer, L., Mura, T.: Growth rate of a penny-shaped crack in hydraulic fracturing of rocks, 2. *Journal of Geophysical Research* **81**(35), 6292–6298 (1976)

[2] Adachi, A., Siebrits, E., Peirce, A., Desroches, J.: Computer simulation of hydraulic fractures. *International Journal of Rock Mechanics and Mining Sciences* **44**(5), 739–757 (2007)

[3] Adachi, J.I., Detournay, E.: Self-similar solution of a plane-strain fracture driven by a power-law fluid. *International Journal for Numerical and Analytical Methods in Geomechanics* **26**(6), 579–604 (2002)

[4] Advani, S.H., Lee, T.S., Lee, J.K.: Three-dimensional modeling of hydraulic fractures in layered media: Part I—Finite element formulations. *Journal of Energy Resources Technology* **112**(1), 1–9 (1990)

[5] Advani, S.H., Torok, J.S., Lee, J.K., Choudhry, S.: Explicit time-dependent solutions and numerical evaluations for penny-shaped hydraulic fracture models. *Journal of Geophysical Research: Solid Earth* **92**(B8), 8049–8055 (1987)

[6] Ainsworth, M., Senior, B.: Aspects of an adaptive hp-finite element method: Adaptive strategy, conforming approximation and efficient solvers. *Computer Methods in Applied Mechanics and Engineering* **150**(1-4), 65–87 (1997)

[7] Atallah, S.: US History's Worst LNG Disaster (1979)

[8] Babuška, I., Banerjee, U.: Stable Generalized Finite Element Method (SGFEM). *Computer Methods in Applied Mechanics and Engineering* **201**, 91–111 (2012)

[9] Babuška, I., Melenk, J.M.: The partition of unity method. *International Journal for Numerical Methods in Engineering* **40**(4), 727–758 (1997)

[10] Baitsch, M., Hartmann, D.: Piecewise polynomial shape functions for hp-finite element methods. *Computer Methods in Applied Mechanics and Engineering* **198**(13-14), 1126–1137 (2009)

[11] Barenblatt, G.I.: The mathematical theory of equilibrium cracks in brittle fracture. pp. 55–129. Elsevier (1962)

[12] Barenblatt, G.I.: The mathematical theory of equilibrium cracks in brittle fracture. In: *Advances in Applied Mechanics*, vol. 7, pp. 55–129. Elsevier (1962)

[13] Barree, R.D., et al.: A practical numerical simulator for three-dimensional fracture propagation in heterogeneous media. In: *SPE Reservoir Simulation Symposium*. Society of Petroleum Engineers (1983)

[14] Basar, Y., Krätzig, W.B.: Mechanik der Flächentragwerke: Theorie, Berechnungsmethoden, Anwendungsbeispiele. Springer-Verlag (2013)

[15] Batchelor, C.K., Batchelor, G.K.: An introduction to fluid dynamics. Cambridge University Press (2000)

[16] Baydoun, M., Fries, T.P.: Crack propagation criteria in three dimensions using the XFEM and an explicit-implicit crack description. *International Journal of Fracture* **178**(1-2, SI), 51–70 (2012)

[17] Belytschko, T., Black, T.: Elastic crack growth in finite elements with minimal remeshing. *International Journal of Numerical Methods in Engineering* **45**(5), 601–620 (1999)

[18] Belytschko, T., Gracie, R., Ventura, G.: A review of extended/generalized finite element methods for material modeling. *Modelling and Simulation in Materials Science and Engineering* **17**(4), 043,001 (2009)

[19] Belytschko, T., Moës, N., Usui, S., Parimi, C.: Arbitrary discontinuities in finite elements. *International Journal for Numerical Methods in Engineering* **50**(4), 993–1013 (2001)

[20] Belytschko, T., Parimi, C., Moës, N., Sukumar, N., Usui, S.: Structured extended finite element methods for solids defined by implicit surfaces. *International Journal for Numerical Methods in Engineering* **56**(4), 609–635 (2003)

[21] Bieniawski, Z.T.: Mechanism of brittle fracture of rock: part I—theory of the fracture process. In: *International Journal of Rock Mechanics and Mining Sciences & Geomechanics Abstracts*, vol. 4, pp. 395–406. Elsevier (1967)

[22] Bieniawski, Z.T.: Stability concept of brittle fracture propagation in rock. *Engineering Geology* **2**(3), 149–162 (1967)

[23] Bischoff, M., Ramm, E., Irslinger., J.: Models and Finite Elements for Thin-walled Structures. In: *Encyclopedia of Computational Mechanics Second Edition (eds E. Stein, R. Borst and T. J. Hughes)* (2017)

[24] Board, M., Rorke, T., Williams, G., Gay, N., et al.: Fluid injection for rockburst control in deep mining. In: *The 33th US Symposium on Rock Mechanics (USRMS)*. American Rock Mechanics Association (1992)

[25] de Boer, A., van Zuijlen, A.H., Bijl, H.: Review of coupling methods for non-matching meshes. *Computer Methods in Applied Mechanics and Engineering* **196**(8), 1515–1525 (2007)

[26] Bose, P., Maheshwari, A., Shu, C., Wuhrer, S.: A survey of geodesic paths on 3D surfaces. *Computational Geometry* **44**(9), 486–498 (2011)

[27] Bourdin, B., Chukwudozie, C.P., Yoshioka, K., et al.: A variational approach to the numerical simulation of hydraulic fracturing. In: *SPE Annual Technical Conference and Exhibition*. Society of Petroleum Engineers (2012)

[28] Bourdin, B., Francfort, G.A., Marigo, J.J.: Numerical experiments in revisited brittle fracture. *Journal of the Mechanics and Physics of Solids* **48**(4), 797–826 (2000)

[29] Calladine, C.R.: Theory of shell structures. Cambridge University Press (1989)

[30] Chan, S.K., Tuba, I.S., Wilson, W.K.: On the finite element method in linear fracture mechanics. *Engineering Fracture Mechanics* **2**, 1–17 (1970)

[31] Chang, J., Xu, J.q., Mutoh, Y.: A general mixed-mode brittle fracture criterion for cracked materials. *Engineering Fracture Mechanics* **73**(9), 1249–1263 (2006)

[32] Chen, J., Han, Y.: Shortest paths on a polyhedron, Part I: Computing shortest paths. *International Journal of Computational Geometry & Applications* **6**(02), 127–144 (1996)

[33] Cheng, K.W., Fries, T.P.: Higher-order XFEM for curved strong and weak discontinuities. *International Journal of Numerical Methods in Engineering* **82**(5), 564–590 (2010)

[34] Cherepanov, G.P.: The propagation of cracks in a continuous medium. *Journal of Applied Mathematics and Mechanics* **31**(3), 503–512 (1967)

[35] Chessa, J., Belytschko, T.: An extended finite element method for two-phase fluids. *Journal of Applied Mechanics* **70**(1), 10–17 (2003)

[36] Chessa, J., Smolinski, P., Belytschko, T.: The extended finite element method (XFEM) for solidification problems. *International Journal for Numerical Methods in Engineering* **53**(8), 1959–1977 (2002)

[37] Chessa, J., Wang, H., Belytschko, T.: On the construction of blending elements for local partition of unity enriched finite elements. *International Journal for Numerical Methods in Engineering* **57**(7), 1015–1038 (2003)

[38] Chopp, D.L., Sukumar, N.: Fatigue crack propagation of multiple coplanar cracks with the coupled extended finite element/fast marching method. *International Journal of Engineering Science* **41**(8), 845–869 (2003)

[39] Clifton, R.J., Abou-Sayed, A.S., et al.: A variational approach to the prediction of the three-dimensional geometry of hydraulic fractures. In: *SPE/DOE Low Permeability Gas Reservoirs Symposium*. Society of Petroleum Engineers (1981)

[40] Cruz, F., Roehl, D., do Amaral Vargas Jr, E.: An XFEM element to model intersections between hydraulic and natural fractures in porous rocks. *International Journal of Rock Mechanics and Mining Sciences* **112**, 385–397 (2018)

[41] Das, B.M.: Principles of foundation engineering. Cengage learning (2015)

[42] Das, B.M., Sobhan, K.: Principles of geotechnical engineering. Cengage learning (2013)

[43] Daux, C., Moës, N., Dolbow, J., Sukumar, N., Belytschko, T.: Arbitrary branched and intersecting cracks with the extended finite element method. *International Journal for Numerical Methods in Engineering* **48**(12), 1741–1760 (2000)

[44] Delfour, M., Zolésio, J.: Shapes and Geometries: Metrics, Analysis, Differential Calculus, and Optimization. SIAM (2011)

[45] Demlow, A.: Higher-order finite element methods and pointwise error estimates for elliptic problems on surfaces. *SIAM Journal on Numerical Analysis* **47**(2), 805–827 (2009)

[46] Desroches, J., Detournay, E., Lenoach, B., Papanastasiou, P., Pearson, J.R.A., Thiercelin, M., Cheng, A.: The crack tip region in hydraulic fracturing. In: *Proceedings of the Royal Society of London A: Mathematical, Physical and Engineering Sciences*, vol. 447, pp. 39–48. The Royal Society (1994)

[47] Detournay, E.: Fluid and solid singularities at the tip of a fluid-driven fracture. In: *IUTAM Symposium on Non-Linear Singularities in Deformation and Flow*, pp. 27–42. Springer (1999)

[48] Detournay, E.: Propagation regimes of fluid-driven fractures in impermeable rocks. *International Journal of Geomechanics* **4**(1), 35–45 (2004)

[49] Detournay, E.: Mechanics of Hydraulic Fractures. In: Davis, SH and Moin, P (ed.) *Annual Review of Fluid Mechanics*, *Annual Review of Fluid Mechanics*, vol. 48, pp. 311–339 (2016)

[50] Detournay, E., Garagash, D.: The near-tip region of a fluid-driven fracture propagating in a permeable elastic solid. *Journal of Fluid Mechanics* **494**, 1–32 (2003)

[51] Detournay, E., Peirce, A., Bunger, A., et al.: Viscosity-dominated hydraulic fractures. In: *1st Canada-US Rock Mechanics Symposium*. American Rock Mechanics Association (2007)

[52] Dijkstra, E.W.: A note on two problems in connexion with graphs. *Numerische mathematik* **1**(1), 269–271 (1959)

[53] Dolbow, J., Moës, N., Belytschko, T.: Discontinuous enrichment in finite elements with a partition of unity method. *Finite Elements in Analysis and Design* **36**(3), 235–260 (2000)

[54] Dong, C.Y., de Pater, C.J.: Numerical implementation of displacement discontinuity method and its application in hydraulic fracturing. *Computer Methods in Applied Mechanics and Engineering* **191**(8-10), 745–760 (2001)

[55] Dontsov, E.V., Peirce, A.P.: An enhanced pseudo-3D model for hydraulic fracturing accounting for viscous height growth, non-local elasticity, and lateral toughness. *Engineering Fracture Mechanics* **142**, 116–139 (2015)

[56] Duflot, M.: A meshless method with enriched weight functions for three-dimensional crack propagation. *International Journal for Numerical Methods in Engineering* **65**(12), 1970–2006 (2006)

[57] Duflot, M.: A study of the representation of cracks with level sets. *International Journal for Numerical Methods in Engineering* **70**(11), 1261–1302 (2007)

[58] Dugdale, D.S.: Yielding of steel sheets containing slits. *Journal of the Mechanics and Physics of Solids* **8**, 100–104 (1960)

[59] Dugdale, D.S.: Yielding of steel sheets containing slits. *Journal of the Mechanics and Physics of Solids* **8**(2), 100–104 (1960)

[60] Dziuk, G.: Finite elements for the beltrami operator on arbitrary surfaces. In: *Partial differential equations and calculus of variations*, pp. 142–155. Springer (1988)

[61] Dziuk, G., Elliott, C.M.: Finite element methods for surface PDEs. *Acta Numerica* **22**, 289–396 (2013)

[62] Economides, M.J., Nolte, K.G., et al.: Reservoir stimulation, vol. 2. Prentice Hall Englewood Cliffs, NJ (1989)

[63] Erdogan, F., Sih, G.C.: On the crack extension in plates under plane loading and transverse shear. *Journal of Basic Engineering* **85**(4), 519–525 (1963)

[64] Fett, T.: Stress intensity factors and weight functions for special crack problems, vol. 6025. FZKA (1998)

[65] Frey, P.J., George, P.L.: Mesh generation: application to finite elements. ISTE (2007)

[66] Fries, T.P.: A corrected XFEM approximation without problems in blending elements. *International Journal of Numerical Methods in Engineering* **75**(5), 503–532 (2008)

[67] Fries, T.P.: Overview and comparison of different variants of the XFEM. *PAMM* **14**(1), 27–30 (2014)

[68] Fries, T.P., Baydoun, M.: Crack propagation with the extended finite element method and a hybrid explicit-implicit crack description. *International Journal of Numerical Methods in Engineering* **89**(12), 1527–1558 (2012)

[69] Fries, T.P., Belytschko, T.: The intrinsic XFEM: a method for arbitrary discontinuities without additional unknowns. *International Journal for Numerical Methods in Engineering* **68**(13), 1358–1385 (2006)

[70] Fries, T.P., Belytschko, T.: The extended/generalized finite element method: An overview of the method and its applications. *International Journal of Numerical Methods in Engineering* **84**(3), 253–304 (2010)

[71] Fries, T.P., Byfut, A., Alizada, A., Cheng, K.W., Schröder, A.: Hanging nodes and XFEM. *International Journal for Numerical Methods in Engineering* **86**(4-5), 404–430 (2011)

[72] Fries, T.P., Omerović, S.: Higher-order accurate integration of implicit geometries. *International Journal for Numerical Methods in Engineering* **106**(5), 323–371 (2016)

[73] Fries, T.P., Omerović, S., Schöllhammer, D., Steidl, J.: Higher-order meshing of implicit geometries-Part I: Integration and interpolation in cut elements. *Computer Methods in Applied Mechanics and Engineering* **313**, 759–784 (2017)

[74] Garagash, D.I.: Propagation of a plane-strain hydraulic fracture with a fluid lag: Early-time solution. *International journal of solids and structures* **43**(18-19), 5811–5835 (2006)

[75] Geertsma, J., De Klerk, F., et al.: A rapid method of predicting width and extent of hydraulically induced fractures. *Journal of Petroleum Technology* **21**(12), 1–571 (1969)

[76] Geubelle, P.H., Baylor, J.S.: Impact-induced delamination of composites: a 2d simulation. *Composites Part B: Engineering* **29**(5), 589–602 (1998)

[77] Glinka, G., Shen, G.: Universal features of weight functions for cracks in mode I. *Engineering Fracture Mechanics* **40**(6), 1135–1146 (1991)

[78] Goli, E., Bayesteh, H., Mohammadi, S.: Mixed mode fracture analysis of adiabatic cracks in homogeneous and non-homogeneous materials in the framework of partition of unity and the path-independent interaction integral. *Engineering Fracture Mechanics* **131**, 100–127 (2014)

[79] Gordeliy, E., Peirce, A.: Coupling schemes for modeling hydraulic fracture propagation using the XFEM. *Computer Methods in Applied Mechanics and Engineering* **253**, 305–322 (2013)

[80] Gordeliy, E., Peirce, A.: Implicit level set schemes for modeling hydraulic fractures using the XFEM. *Computer Methods in Applied Mechanics and Engineering* **266**, 125–143 (2013)

[81] Gosz, M., Dolbow, J., Moran, B.: Domain integral formulation for stress intensity factor computation along curved three-dimensional interface cracks. *International Journal of Solids and Structures* **35**(15), 1763–1783 (1998)

[82] Gosz, M., Moran, B.: An interaction energy integral method for computation of mixed-mode stress intensity factors along non-planar crack fronts in three dimensions. *Engineering Fracture Mechanics* **69**(3), 299–319 (2002)

[83] Gracie, R., Wang, H., Belytschko, T.: Blending in the extended finite element method by discontinuous galerkin and assumed strain methods. *International Journal for Numerical Methods in Engineering* **74**(11), 1645–1669 (2008)

[84] Gravouil, A., Moës, N., Belytschko, T.: Non-planar 3D crack growth by the extended finite element and level sets - Part II: Level set update. *International Journal for Numerical Methods in Engineering* **53**(11), 2569–2586 (2002)

[85] Griffith, A.A.: The phenomena of rupture and flow in solids. *Philosophical Transactions of the Royal Society of London. Series A, Containing Papers of a Mathematical or Physical Character* **221**, 163–198 (1921)

[86] Gupta, P., Duarte, C.A.: Simulation of non-planar three-dimensional hydraulic fracture propagation. *International Journal for Numerical and Analytical Methods in Geomechanics* **38**(13), 1397–1430 (2014)

[87] Gupta, P., Duarte, C.A., Dhankhar, A.: Accuracy and robustness of stress intensity factor extraction methods for the generalized/eXtended Finite Element Method. *Engineering Fracture Mechanics* **179**, 120–153 (2017)

[88] H. Tada, P.C. Paris, G.R. Irwin: The analysis of cracks handbook. New York: ASME Press (2000)

[89] Hillerborg, A., Modéer, M., Petersson, P.E.: Analysis of crack formation and crack growth in concrete by means of fracture mechanics and finite elements. *Cement and concrete research* **6**(6), 773–781 (1976)

[90] Hunsweck, M.J., Shen, Y., Lew, A.J.: A finite element approach to the simulation of hydraulic fractures with lag. *International Journal for Numerical and Analytical Methods in Geomechanics* **37**(9), 993–1015 (2013)

[91] Hussain, M.A., Pu, S.L., Underwood, J.: Strain energy release rate for a crack under combined mode I and mode II. In: *Fracture Analysis: Proceedings of the 1973 National Symposium on Fracture Mechanics, Part II.* ASTM International (1974)

[92] Hutchinson, J.: Singular behaviour at the end of a tensile crack in a hardening material. *Journal of the Mechanics and Physics of Solids* **16**(1), 13–31 (1968)

[93] Inglis, C.E.: Stresses in a plate due to the presence of cracks and sharp corners. *Trans Inst Naval Archit* **55**, 219–241 (1913)

[94] Ingraffea, A.R., Manu, C.: Stress-intensity factor computation in three dimensions with quarter-point elements. *International Journal for Numerical Methods in Engineering* **15**(10), 1427–1445 (1980)

[95] Irwin, G.: Fracture dynamics. *Fracturing of Metals* pp. 147–166 (1948)

[96] Irwin, G.R.: Analysis of stresses and strains near the end of a crack traversing a plate. *Journal of Applied Mechanics* **24**, 361–364 (1957)

[97] Jaky, J.: The coefficient of earth pressure at rest. *Journal of the Society of Hungarian Architects and Engineers* pp. 355–358 (1944)

[98] Jaśkowiec, J., van der Meer, F.P.: A consistent iterative scheme for 2d and 3d cohesive crack analysis in XFEM. *Computers & Structures* **136**, 98–107 (2014)

[99] Jin, Y., González-Estrada, O.A., Pierard, O., Bordas, S.P.A.: Error-controlled adaptive extended finite element method for 3D linear elastic crack propagation. *Computer Methods in Applied Mechanics and Engineering* **318**, 319–348 (2017)

[100] Kageyama, K., Okamura, H.: Elastic analysis of infinitesimally kinked crack under tension and transverse shear and the maximum energy release rate criterion. *Transactions of the Japan Society of Mechanical Engineers Series A* **48**(430), 783–791 (1982)

[101] Kamilis, D.: Numerical methods for the PDEs on curves and surfaces. Masters thesis, Umeå university, Umeå, Sweden (2013)

[102] Kanai, T., Suzuki, H.: Approximate shortest path on a polyhedral surface and its applications. *Computer-Aided Design* **33**(11), 801–811 (2001)

[103] Kang, Z., Bui, T.Q., Hirose, S., et al.: Dynamic stationary crack analysis of isotropic solids and anisotropic composites by enhanced local enriched consecutive-interpolation elements. *Composite Structures* **180**, 221–233 (2017)

[104] Kang, Z., Bui, T.Q., Saitoh, T., Hirose, S.: Quasi-static crack propagation simulation by an enhanced nodal gradient finite element with different enrichments. *Theoretical and Applied Fracture Mechanics* **87**, 61–77 (2017)

[105] Kang, Z., Bui, T.Q., Saitoh, T., Hirose, S., et al.: An extended consecutive-interpolation quadrilateral element (XCQ4) applied to linear elastic fracture mechanics. *Acta Mechanica* **226**(12), 3991–4015 (2015)

[106] Kanninen, M., Popelar, C.: Advanced Fracture Mechanics. Oxford engineering science series. Oxford University Press (1985)

[107] Karlsson, A., Bäcklund, J.: J-integral at loaded crack surfaces. *International Journal of Fracture* **14**(6), R311–R318 (1978)

[108] Karypis, G., Kumar, V.: A fast and high quality multilevel scheme for partitioning irregular graphs. *SIAM Journal on scientific Computing* **20**(1), 359–392 (1998)

[109] Kaya, A., Erdogan, F.: Stress intensity factors and COD in an orthotropic strip. *International Journal of Fracture* **16**(2), 171–190 (1980)

[110] Khoei, A.R.: Extended finite element method: theory and applications. John Wiley & Sons (2014)

[111] Khoei, A.R., Hirmand, M., Vahab, M., Bazargan, M.: An enriched FEM technique for modeling hydraulically driven cohesive fracture propagation in impermeable media with frictional natural faults: Numerical and experimental investigations. *International Journal for Numerical Methods in Engineering* **104**(6), 439–468 (2015)

[112] Khoei, A.R., Vahab, M., Haghighat, E., Moallemi, S.: A mesh-independent finite element formulation for modeling crack growth in saturated porous media based on an enriched-FEM technique. *International Journal of Fracture* **188**(1), 79–108 (2014)

[113] Khristianovic, S., Zheltov, Y.: Formation of vertical fractures by means of highly viscous fluids. In: *Proc. 4th world petroleum congress, Rome*, vol. 2, pp. 579–586 (1955)

[114] Kimmel, R., Sethian, J.A.: Computing geodesic paths on manifolds. *Proceedings of the national academy of Sciences* **95**(15), 8431–8435 (1998)

[115] Knott, J.: Fundamentals of Fracture Mechanics. Butterworths (1973)

[116] Kuhn, C., Müller, R.: A continuum phase field model for fracture. *Engineering Fracture Mechanics* **77**(18), 3625–3634 (2010)

[117] Kuna, M.: Finite elements in fracture mechanics, vol. 10. Springer (2013)

[118] Laborde, P., Pommier, J., Renard, Y., Salaün, M.: High-order extended finite element method for cracked domains. *International Journal for Numerical Methods in Engineering* **64**(3), 354–381 (2005)

[119] Lazarus, V., Buchholz, F.G., Fulland, M., Wiebesiek, J.: Comparison of predictions by mode II or mode III criteria on crack front twisting in three or four point bending experiments. *International Journal of Fracture* **153**(2), 141–151 (2008)

[120] Lecampion, B.: An extended finite element method for hydraulic fracture problems. *Communications in Numerical Methods in Engineering* **25**(2), 121–133 (2009)

[121] Lenoach, B.: The crack tip solution for hydraulic fracturing in a permeable solid. *Journal of the Mechanics and Physics of Solids* **43**(7), 1025–1043 (1995)

[122] Maiti, S.K., Smith, R.: Comparison of the criteria for mixed mode brittle fracture based on the preinstability stress-strain field. *International Journal of Fracture* **24**(1), 5–22 (1984)

[123] McLennan, J.D., Picardy, J.C., et al.: Pseudo-three-dimensional fracture growth modeling. In: *The 26th US Symposium on Rock Mechanics (USRMS)*. American Rock Mechanics Association (1985)

[124] Mesri, G., Hayat, T.M.: The coefficient of earth pressure at rest. *Canadian Geotechnical Journal* **30**(4), 647–666 (1993)

[125] Miehe, C., Hofacker, M., Welschinger, F.: A phase field model for rate-independent crack propagation: Robust algorithmic implementation based on operator splits. *Computer Methods in Applied Mechanics and Engineering* **199**(45-48), 2765–2778 (2010)

[126] Mitchell, J.S.B., Mount, D.M., Papadimitriou, C.H.: The discrete geodesic problem. *SIAM Journal on Computing* **16**(4), 647–668 (1987)

[127] Moës, N., Belytschko, T.: Extended finite element method for cohesive crack growth. *Engineering Fracture Mechanics* **69**, 813–833 (2002)

[128] Moës, N., Dolbow, J., Belytschko, T.: A finite element method for crack growth without remeshing. *International Journal of Numerical Methods in Engineering* **46**(1), 131–150 (1999)

[129] Moës, N., Gravouil, A., Belytschko, T.: Non-planar 3D crack growth by the extended finite element and level sets - Part I: Mechanical model. *International Journal of Numerical Methods in Engineering* **53**(11), 2549–2568 (2002)

[130] Moës, N., Stolz, C., Bernard, P.E., Chevaugeon, N.: A level set based model for damage growth: The thick level set approach. *International Journal of Numerical Methods in Engineering* **86**(3), 358–380 (2011)

[131] Mohammadnejad, T., Khoei, A.R.: An extended finite element method for hydraulic fracture propagation in deformable porous media with the cohesive crack model. *Finite Elements in Analysis and Design* **73**, 77–95 (2013)

[132] Moran, B., Shih, C.F.: Crack tip and associated domain integrals from momentum and energy balance. *Engineering Fracture Mechanics* **27**(6), 615–642 (1987)

[133] Moran, B., Shih, C.F.: A general treatment of crack tip contour integrals. *International Journal of Fracture* **35**(4), 295–310 (1987)

[134] Nahta, R., Moran, B.: Domain integrals for axisymmetric interface crack problems. *International Journal of Solids and Structures* **30**(15), 2027–2040 (1993)

[135] Nejati, M., Paluszny, A., Zimmerman, R.: On the use of quarter-point tetrahedral finite elements in linear elastic fracture mechanics. *Engineering Fracture Mechanics* **144**, 194–221 (2015)

[136] Nemat-Nasser, S., Abé, H., Hirakawa, S.: Hydraulic fracturing and geothermal energy. In: *Proceedings of First Japan-United States Joint Seminar on Hydraulic Fracturing and Geothermal Energy* (1982)

[137] Nordgren, R., et al.: Propagation of a vertical hydraulic fracture. *Society of Petroleum Engineers Journal* **12**(04), 306–314 (1972)

[138] Olshanskii, M.A., Reusken, A.: A finite element method for surface PDEs: matrix properties. *Numerische mathematik* **114**(3), 491–520 (2010)

[139] Orowan, E.: Fracture and strength of solids. *Reports on Progress in Physics* **12**, 185–232 (1948)

[140] Ortiz, J.E., Cisilino, A.P.: Boundary element method for J-integral and stress intensity factor computations in three-dimensional interface cracks. *International Journal of Fracture* **133**(3), 197–222 (2005)

[141] Perkins, T., Kern, L., et al.: Widths of hydraulic fractures. *Journal of Petroleum Technology* **13**(09), 937–949 (1961)

[142] Pine, R.J., Cundall, P.A.: Applications of the fluid-rock interaction program (FRIP) to the modelling of hot dry rock geothermal energy systems. In: *Proceedings of the International Symposium on Fundamentals of Rock Joints*, pp. 293–302. Bjorkliden Sweden, Centek (1985)

[143] Pommier, S., Gravouil, A., Moës, N., Combescure, A.: Extended finite element method for crack propagation. John Wiley & Sons (2013)

[144] Rabczuk, T., Belytschko, T.: A three-dimensional large deformation meshfree method for arbitrary evolving cracks. *Computer Methods in Applied Mechanics and Engineering* **196**(29-30), 2777–2799 (2007)

[145] Rahman, M.M., Rahman, M.K.: A review of hydraulic fracture models and development of an improved pseudo-3D model for stimulating tight oil/gas sand. *Energy Sources, Part A: Recovery, Utilization, and Environmental Effects* **32**(15), 1416–1436 (2010)

[146] Rans, C.D., Alderliesten, R.C.: Formulating an effective strain energy release rate for a linear elastic fracture mechanics description of delamination growth. In: *Proceedings of 17th International Conference on Composite Materials (ICCM-17)* (2009)

[147] Rao, B.N., Rahman, S.: An efficient meshless method for fracture analysis of cracks. *Computational Mechanics* **26**(4), 398–408 (2000)

[148] Rethore, J., de Borst, R., Abellan, M.A.: A two-scale approach for fluid flow in fractured porous media. *International Journal of Numerical Methods in Engineering* **71**(7), 780–800 (2007)

[149] Rethore, J., de Borst, R., Abellan, M.A.: A two-scale model for fluid flow in an unsaturated porous medium with cohesive cracks. *Computational Mechanics* **42**(2), 227–238 (2008)

[150] Rice, J., Rosengren, G.: Plane strain deformation near a crack tip in a power-law hardening material. *Journal of the Mechanics and Physics of Solids* **16**(1), 1–12 (1968)

[151] Rice, J.R.: Mathematical analysis in the mechanics of fracture. *Fracture: An Advanced Treatise* **2**, 191–311 (1968)

[152] Rice, J.R.: A path independent integral and the approximate analysis of strain concentration by notches and cracks. *Journal of Applied Mechanics* **35**(2), 379–386 (1968)

[153] Richard, H.A., Fulland, M., Sander, M.: Theoretical crack path prediction. *Fatigue & Fracture of Engineering Materials & Structures* **28**(1–2), 3–12 (2005)

[154] Ritchie, R.O.: Mechanisms of fatigue-crack propagation in ductile and brittle solids. *International Journal of Fracture* **100**(1), 55–83 (1999)

[155] Rubin, A.: Propagation of magma-filled cracks. *Annual Review of Earth and Planetary Sciences* **23**, 287–336 (1995)

[156] Salimzadeh, S., Khalili, N.: A three-phase XFEM model for hydraulic fracturing with cohesive crack propagation. *Computers and Geotechnics* **69**, 82–92 (2015)

[157] Savitski, A.A., Detournay, E.: Propagation of a penny-shaped fluid-driven fracture in an impermeable rock: asymptotic solutions. *International Journal of Solids and Structures* **39**(26), 6311–6337 (2002)

[158] Schapery, R.A.: Correspondence principles and a generalized J integral for large deformation and fracture analysis of viscoelastic media. *International Journal of Fracture* **25**(3), 195–223 (1984)

[159] Schätzer, M., Fries, T.P.: Fitting stress intensity factors from crack opening displacements in 2D and 3D XFEM. *PAMM* **15**(1), 149–150 (2015)

[160] Schätzer, M., Fries, T.P.: Hydraulic fracturing with a simplified fluid model and XFEM. *PAMM* **16**(1), 167–168 (2016)

[161] Schätzer, M., Fries, T.P.: Stress Intensity Factors Through Crack Opening Displacements in the XFEM. In: *Advances in Discretization Methods*, pp. 143–164. Springer (2016)

[162] Schätzer, M., Fries, T.P.: The XFEM for a simplified model in hydraulic fracturing. In: *ECCOMAS Congress 2016-Proceedings of the 7th European Congress on Computational Methods in Applied Sciences and Engineering*, pp. 1637–1646. National Technical University of Athens (2016)

[163] Schätzer, M., Fries, T.P.: Heuristic pressure profiles in hydraulic fracturing. *PAMM* **18**(1), e201800,068 (2018)

[164] Schätzer, M., Fries, T.P.: Loaded crack surfaces in two and three dimensions with XFEM. *Applied Mathematical Modelling* **78**, 863–885 (2020)

[165] Schenk, O., Gärtner, K.: Solving unsymmetric sparse systems of linear equations with pardiso. *Future Generation Computer Systems* **20**(3), 475–487 (2004)

[166] Schenk, O., Gärtner, K.: On fast factorization pivoting methods for sparse symmetric indefinite systems. *Electronic Transactions on Numerical Analysis* **23**(1), 158–179 (2006)

[167] Settari, A., Cleary, M.P., et al.: Development and testing of a pseudo-three-dimensional model of hydraulic fracture geometry. *SPE Production Engineering* **1**(06), 449–466 (1986)

[168] Sheng, M., Li, G., Shah, S., Lamb, A.R., Bordas, S.P.: Enriched finite elements for branching cracks in deformable porous media. *Engineering Analysis with Boundary Elements* **50**, 435–446 (2015)

[169] Shih, C.F., Asaro, R.J.: Elastic-plastic analysis of cracks on bimaterial interfaces: part I—small scale yielding. *Journal of Applied Mechanics* **55**(2), 299–316 (1988)

[170] Sih, G.C., Macdonald, B.: Fracture mechanics applied to engineering problems-strain energy density fracture criterion. *Engineering Fracture Mechanics* **6**(2), 361–386 (1974)

[171] Simo, J.C., Oliver, J., Armero, F.: An analysis of strong discontinuities induced by strain-softening in rate-independent inelastic solids. *Computational Mechanics* **12**(5), 277–296 (1993)

[172] Sneddon, I.N.: The distribution of stress in the neighbourhood of a crack in an elastic solid. *Proceedings of the Royal Society of London. Series A. Mathematical and Physical Sciences* **187**(1009), 229–260 (1946)

[173] Šolín, P., Červenỳ, J., Doležel, I.: Arbitrary-level hanging nodes and automatic adaptivity in the hp-FEM. *Mathematics and Computers in Simulation* **77**(1), 117–132 (2008)

[174] Song, H., Rahman, S.S.: An extended J-integral for evaluating fluid-driven cracks in hydraulic fracturing. *Journal of Rock Mechanics and Geotechnical Engineering* **10**(5), 832–843 (2018)

[175] Stazi, F.L., Budyn, E., Chessa, J., Belytschko, T.: An extended finite element method with higher-order elements for curved cracks. *Computational Mechanics* **31**(1-2), 38–48 (2003)

[176] Stern, M., Becker, E.B., Dunham, R.S.: A contour integral computation of mixed-mode stress intensity factors. *International Journal of Fracture* **12**(3), 359–368 (1976)

[177] Stolarska, M., Chopp, D., Moës, N., Belytschko, T.: Modelling crack growth by level sets in the extended finite element method. *International Journal of Numerical Methods in Engineering* **51**(8), 943–960 (2001)

[178] Stolarska, M., Chopp, D.L.: Modeling thermal fatigue cracking in integrated circuits by level sets and the extended finite element method. *International Journal of Engineering Science* **41**(20), 2381–2410 (2003)

[179] Sukumar, N., Chopp, D.L., Moës, N., Belytschko, T.: Modeling holes and inclusions by level sets in the extended finite-element method. *Computer Methods in Applied Mechanics and Engineering* **190**(46-47), 6183–6200 (2001)

[180] Sukumar, N., Chopp, D.L., Moran, B.: Extended finite element method and fast marching method for three-dimensional fatigue crack propagation. *Engineering Fracture Mechanics* **70**(1), 29–48 (2003)

[181] Sukumar, N., Moës, N., Moran, B., Belytschko, T.: Extended finite element method for three-dimensional crack modelling. *International Journal of Numerical Methods in Engineering* **48**(11), 1549–1570 (2000)

[182] Sukumar, N., Moran, B., Black, T., Belytschko, T.: An element-free galerkin method for three-dimensional fracture mechanics. *Computational Mechanics* **20**(1-2), 170–175 (1997)

[183] Surazhsky, V., Surazhsky, T., Kirsanov, D., Gortler, S.J., Hoppe, H.: Fast exact and approximate geodesics on meshes. In: *ACM Transactions on Graphics (TOG)*, vol. 24, pp. 553–560 (2005)

[184] Tarancón, J., Vercher, A., Giner, E., Fuenmayor, F.: Enhanced blending elements for XFEM applied to linear elastic fracture mechanics. *International Journal for Numerical Methods in Engineering* **77**(1), 126–148 (2009)

[185] Thevenaz, P., Blu, T., Unser, M.: Interpolation revisited. *IEEE Transactions on Medical Imaging* **19**(7), 739–758 (2000)

[186] Thompson, J.F., Soni, B.K., Weatherill, N.P.: Handbook of grid generation. CRC press (1998)

[187] T.L. Anderson: Fracture mechanics: fundamentals and applications. CRC press (2005)

[188] Vandamme, L., Curran, J.H.: A three-dimensional hydraulic fracturing simulator. *International Journal for Numerical Methods in Engineering* **28**(4), 909–927 (1989)

[189] Walker, S.W.: The Shapes of Things: A Practical Guide to Differential Geometry and the Shape Derivative. Advances in Design and Control. SIAM (2015)

[190] Walters, M., Paulino, G., Dodds, R.: Interaction integral procedures for 3-D curved cracks including surface tractions. *Engineering Fracture Mechanics* **72**(11), 1635–1663 (2005)

[191] Wang, Z., Yu, T., Bui, T.Q., Tanaka, S., Zhang, C., Hirose, S., Curiel-Sosa, J.L.: 3-D local mesh refinement XFEM with variable-node hexahedron elements for extraction of stress intensity factors of straight and curved planar cracks. *Computer Methods in Applied Mechanics and Engineering* **313**, 375–405 (2017)

[192] Westergaard, H.M.: Bearing pressures and cracks. *Journal of Applied Mechanics* **6**(2), 49–53 (1939)

[193] Williams, M.: On the stress distribution at the base of a stationary crack. *Journal of Applied Mechanics* **24**(1), 109–114 (1957)

[194] Williams, M.L., Ellinger, G.A.: Investigation of structural failures of welded ships. *Welding Journal* **32**, 498–528 (1953)

[195] Yau, J.F., Wang, S.S., Corten, H.T.: A mixed-mode crack analysis of isotropic solids using conservation laws of elasticity. *Journal of Applied Mechanics* **47**(2), 335–341 (1980)

[196] Yu, T., Bui, T.Q.: Numerical simulation of 2-D weak and strong discontinuities by a novel approach based on XFEM with local mesh refinement. *Computers & Structures* **196**, 112–133 (2018)

[197] Zhang, X., Bui, T.Q.: A fictitious crack XFEM with two new solution algorithms for cohesive crack growth modeling in concrete structures. *Engineering Computations* **32**(2), 473–497 (2015)

[198] Zhuang, X., Augarde, C., Mathisen, K.: Fracture modeling using meshless methods and level sets in 3D: framework and modeling. *International Journal for Numerical Methods in Engineering* **92**(11), 969–998 (2012)